DEVELOPMENT OF A PHOTOACOUSTIC IMAGING SYSTEM

Design and Development of a Novel Photoacoustic Imaging System for Detection of Intracranial hemorrhages

By Mandakini Jain,

A Thesis Submitted to the School of Graduate Studies in the Partial Fulfillment of the Requirements for the Degree Master of Applied Science

McMaster University © Copyright by Mandakini Jain December 28, 2018

McMaster University

Master of Applied Science (2018)

Hamilton, Ontario (McMaster School of Biomedical Engineering)

TITLE: Design and Development of a Novel Photoacoustic Imaging System for Detection of Intracranial hemorrhages

AUTHOR: Mandakini Jain (McMaster University)

SUPERVISOR: Dr. Troy Farncombe

NUMBER OF PAGES: xx, 129

Abstract

Photoacoustic (PA) imaging has the potential to overcome disadvantages of optical and ultrasonic imaging techniques by combining the two imaging modalities. This allows for exploitation of endogenous contrasts (variants of hemoglobin) to generate energy with light, and provides enhanced resolution by probing for resulting acoustic signals. The resulting platform has widespread applications ranging from structural (vasculature-based) to functional (oxygenation-based) point-of-care clinical imaging. This thesis has been aimed towards the development of a PA system for detection of intracranial hemorrhages. Simulations have been performed using a photon tracking Monte Carlo program and ultrasound wave propagation modeling software, k-wave to simulate light absorption and resultant acoustic signals in tissue. Furthermore, development of a PA imaging setup utilizes a 6-ns pulsed laser operating at 532-nm with a pulse repetition frequency of 28-Hz as the light source. Ultrasonic transducers with centre frequencies ranging from 1- to 5-MHz are used to receive acoustic signals produced from the object illuminated. The system is designed in a handheld, probe-like configuration to enable point-of-care detection and/or imaging. Acoustic signals are amplified and collected through a data acquisition system and processed through software to form an image. Simulations have shown sufficient penetration through superficial tissue, and absorption of light by blood at relevant wavelengths (near-infrared range). Black plastic resin phantoms have been used to characterize point-source PA signals, and complex geometries of phantoms have successfully been imaged and reconstructed with the PA system. Phantom geometries have also been imaged through gelatin and bone. The PA system has been successfully shown to image PA absorbers in different

surrounding media, providing a promising first-step towards further development of the PA system for the detection of intracranial hemorrhages. This research has shown that photoacoustic detection of intracranial hemorrhages may be possible for adult human patients with brain injuries, and that the PA system design presented should be further developed to meet this goal.

Acknowledgements

I would like to sincerely thank my supervisor, Dr. Troy Farncombe, for his immeasurable support and patience. I have learned to appreciate the value of research and scientific creativity under your guidance.

I would also like to extend my gratitude towards my supervisory committee for providing their expertise.

Finally, I would like to thank my family and friends for providing their encouragement through the years. To my doctors, thank you for keeping me healthy. I cannot imagine navigating the last two years without your support.

Contents

Abstract **iii**

Acknowledgements **v**

Acronyms **xix**

1 Preface **1**

2 Introduction **3**

2.1 Clinical Imaging 3

2.2 Multimodality Imaging 5

2.3 EM-induced Acoustic Imaging 7

2.3.1 Thermoacoustic Imaging 11

2.3.2 Photoacoustic Imaging 14

2.4 Conclusion 20

2.4.1 Novel Application 21

3 Fundamentals of photoacoustic imaging **23**

3.1 Optical wave Constraints 24

3.2 Initial Pressure Rise 26

3.3 Pressure Wave Propagation and Detection 28

3.4 Absorption and Tissue Absorbers 32
3.5 Laser Safety 38

4 Simulations **40**

4.1 3D Monte Carlo Simulations 41
4.1.1 Simulating a point absorber 42
4.1.2 Simulating intracranial hemorrhage models 43
4.2 k-wave Simulations 48
4.2.1 Ring Detector design 49
4.2.2 Simulating a point source 51
4.2.3 Simulating Intracranial hemorrhage models 51
4.3 Conclusion 56

5 Hardware and Software Development **57**

5.1 Laser Source 58
5.1.1 Fiber Optic Coupling and Cables 59
5.1.2 Photodetector 61
5.2 Piezoelectric Transducers 63
5.2.1 Disc Immersion Transducers 67
5.2.2 Annular Piezoelectric elements 68
5.2.3 Transducer Casing 70
5.3 Ultrasonic Pre-amplifiers 71
5.4 Data Acquisition Card 72
5.5 Linear Translation Stages 72
5.6 Data Processing 74

6 Experimental Results **83**

6.1 Gel-based Phantoms 84

6.2 Point Source 85

6.2.1 Absorber 86

6.2.2 Point Source Response 86

6.2.3 Amplitude Detection Sensitivities 89

6.3 Line Source 96

6.3.1 Absorber 96

6.3.2 Errors 96

6.4 Image reconstruction of a geometrically complex absorber 98

6.5 Effects of optical scattering on photoacoustic signal 102

6.6 Lipid phantom imaging 105

6.7 Effects of acoustic scattering on photoacoustic signal 109

6.8 Penetration through bone 111

7 Discussion **114**

7.1 Factors influencing signal strength 114

7.2 Noise inducing components 115

7.3 Limitations of this thesis 116

7.4 Conclusion 117

Bibliography **119**

List of Figures

2.1 Absorption coefficients of water and some biological tissues over the *Electromagnetic* (EM) spectrum (Ku et al. 2005a) 10

2.2 Relative dielectric constant and effective conductivity as a function of frequency for human malignant (solid line) and normal (dashed line) breast tissue (Lazebnik et al. 2007) (A), and microwave and *Radiofrequency* (RF) penetration depths in various tissues (Xu and Wang 2006a) (B) 13

3.1 Photoacoustic pressure wave generated by a spherical source (Li and Wang 2009) 31

3.2 Absorption spectra of (a) water, lipids, oxy- (HbO_2) and deoxy-hemoglobin (Hb) in the visible and near-infrared range, (b) water and lipids in the near-infrared range, and (c) water in the ultraviolet, visible and near-infrared range in terms of wavelength-dependent absorption coefficient μ_a in cm^{-1} (Tuchin 2015) 36

3.3 Absorption spectra of mineralized (black) and de-mineralized (grey) cortical bone of horse leg using the integrated sphere technique in the visible and near-infrared range in terms of wavelength-dependent absorption coefficient μ_a in mm^{-1} (Ugryumova et al. 2004) 37

3.4 Spectral ranges of absorption for other tissue chromophores (Tuchin 2015) 37
3.5 Maximum permissible exposure values for skin in the visible and near-infrared spectra (Li and Wang 2009) 39

4.1 Point absorber model with a 200 μm-diameter blood sphere centered in water as the medium; green rays show the path of the 532 nm laser beam (A), energy deposition in the model shown in terms of $log_{10}(A[cm^{-3}])$ when simulated for 30 min (B), and for 120 min (C) 45
4.2 Point absorber model with a 200 μm-diameter blood sphere centered in a low-absorbing medium; green rays show the path of the 532 nm laser beam (A), and energy deposition in the model shown in terms of $log_{10}(A[cm^{-3}])$ when simulated for 20 min (B) 46
4.3 Intracranial hemorrhage parallel-plate model with an elliptical-shaped 1 cm by 0.5 cm by 0.5 cm hematoma centered within cerebro-spinal fluid (simulated with water); green rays show the path of the laser beam (A), energy deposition in the model shown in terms of $log_{10}(A[cm^{-3}])$ when simulated with 532 nm laser source (B), and with 830 nm laser source (C) 47
4.4 Visualization of the ring sensor mask made up of 116 piezoelectric elements using a 3D plot of a binary matrix, where filled voxels are displayed at the positions of the 1 s. Ring sensor has inner diameter of 8.5 mm an outer diameter of 15 mm. 50

4.5 Time-domain PA waveforms overlaid from 116 element sensors making up the ring sensor shown in Figure 4.4 simulated in k-wave. Input to k-wave simulation was taken from the deposition map shown in (B) 4.1 simulated with a $532\,nm$ light source illuminating PA point source in water. 52

4.6 Time-domain PA waveforms overlaid from 32 element sensors making up the ring sensor shown in Figure simulated in k-wave. (A) shows results from simulations with input to k-wave simulation taken from the deposition map shown in (B) of Figure 4.3, where the light source is $532\,nm$. (B) shows shows results from simulations with input to k-wave simulation taken from the deposition map shown in (C) of Figure 4.3, where the light source is $830\,nm$. Red arrow points to rise in PA signal at $200\,ns$ attributed to the change in wavelength. 54

4.7 Healthy brain parallel-plate model; green rays show the path of a $830\,nm$ laser beam (A), energy deposition in the model shown in terms of $log_{10}(A[cm^{-3}])$ (B). Time-domain PA waveforms overlaid from 32 element sensors making up the ring sensor shown in Figure 4.4 simulated in k-wave with input taken from (B) of this figure. . . 55

5.1 Experimental setup showing laser, optical filters, fiber optic cable, annular transducer with housing and XY translational stage; not imaged: pre-amplifier and data acquisition card. 58

5.2 Traditional use of a fiber collimator (left to right) where diverging rays from a light source coming out of a fiber are passed through a converging lens to collimate the beam; NA=numerical aperture, f=focal length, a=mode field diameter, BD=beam diameter, DA=divergence angle. Collimator in the PAI system developed is used in reverse (right to left), where collimated rays from the laser are focused onto the fiber optic cable which can be used within a hand-held probe (Best and Sezerman 1999). 60

5.3 Attenuation in fiber optic cable due to macrobend loss (A), beam profile measurement showing attenuation of light as it is guided into cladding rather than the core of the optical fiber (B), and cross-section of light intensity across the donut beam profile, with the internal void fitted with the parabola $y = 10^{-5}(x - 509)^2 + 00.6$ (C) (Thorlabs Inc. 2018). 62

5.4 Typical structure of a piezoelectric transducer (Ihara 2008). 64

5.5 Annular pattern of a phased array acoustic transducer element commercially available from Olympus (Olympus Corporation 2017). . . 66

5.6 Simulations performed by Biqin et al. 2017 showing ultrasonic frequency detection sensitivities with four different detection geometries: point shape (a), $1\,mm$ disc shape (b), $1\,mm$ bar shape (c), and $60\,\mu m$ ring shape (d). Middle panels show the spatial distributions of ultrasonic amplitude detection sensitivities, and bottom panels show spatial distributions of ultrasonic frequency detection sensitivities along dotted locations in the middle panels. 67

5.7 Depiction of orthogonal mode (A), and receive mode (B) of the immersion transducers with the fiber optic cable (light source), with the object being imaged shown submerged in a water tank. (C) showing an immersion transducer from Olympus Inc. with a $1MHz$ center frequency. 69

5.8 Depiction of the side view (top) and front view (bottom) of the annular or ring transducer with the fiber optic cable (light source) threaded concentric to it, with the object being imaged shown submerged in a water tank (A), and the piezoelectric annular or ring element with center frequency of $3\,MHz$ from Martin & Steiner Inc. (B) 70

5.9 Front view (A) and side view (B) of a PZT element in 3D printed casing built in-house. 71

5.10 Top view of the raster pattern used to acquire images; annular ultrasonic transducer concentric with light source shown on the top-left of the depiction, and object being imaged shown in gray. Each box in the background grid map represents the area over which the transducer pauses and collects 10 signals, and the area which corresponds to 1 pixel in the final photoacoustic image 73

5.11 Top-view depiction of experimental setup showing transducer (top-left), raster pattern (red dotted lines) and absorber in a water bath. Gelatin and petri dish surrounding the point absorber not shown. Each box in the background grid map represents the area over which the transducer pauses and collects 10 signals. Yellow shaded box represents the area whose data will be analyzed in this example. . . 75

5.12 10 photoacoustic signals collected over the yellow shaded area shown in Figure 5.11 77
5.13 PA Signal 1 from Figure 5.12 78
5.14 STEP 1: 10 photoacoustic signals collected over the yellow shaded area shown in Figure 5.11, and brought down to zero baseline . . . 79
5.15 STEP 1: Closer view of zero baseline and raw photoacoustic Signal 1 from Figure 5.14 80
5.16 STEP 2: Zero baseline photoacoustic signals from Figure 5.14 averaged to produce one waveform 81
5.17 STEP 3: Absolute value of dataset from the averaged waveform from Figure 5.16 81
5.18 STEP 4: Time-gated subsection of averaged waveform from 5.17 that forms the value in Figure 5.19 (black pixel shown) 82
5.19 Data of one pixel showing the summed time-gated subsection from Figure 5.18 within the final 2D image produced as a result of summing time-gated subsections of processed signals from all areas depicted in Figure 5.11. 82

6.1 Height (A) and Diameter (B) of absorption-inducing point source embedded in gelatin (C); (D) depiction of experimental setup showing commercial (transmission mode operation) and in-house (receive mode operation) setups situated equidistantly at 0.75 cm away from the point source absorber contained in the petri dish. 87

6.2 Summed photoacoustic image time-gated to include signals from $0.675 - 0.9\,cm$ away from the transducers (A), averaged waveform of 10 signals obtained from a location containing the point absorber (B), and averaged waveform of 10 signals obtained from a location without the point absorber (C) captured through the commercial setup. 90
6.3 Summed photoacoustic image time-gated to include signals from $0.675 - 0.9\,cm$ away from the transducers (A), averaged waveform of 10 signals obtained from a location containing the point absorber (B), and averaged waveform of 10 signals obtained from a location without the point absorber (C) captured through the in-house setup. 91
6.4 Summed photoacoustic images captured through the in-house setup (A), and commercial setup (B) showing the location of their centroids with dotted black lines, time-gated to include signals from $0.675 - 0.9\,cm$ away from the transducers. 92
6.5 Depiction of experimental setup used to capture ultrasonic amplitude spatial detection sensitivities of both commercial and in-house setups; raster pattern shown in red dotted lines moving across (up and down) and away from the point absorber. 93
6.6 Spatial detection sensitivity pattern of the commercial setup containing the disc immersion transducer with $3.5\,MHz$ center frequency. 94

6.7 Spatial detection sensitivity pattern of the in-house setup containing the annular or ring immersion transducer with $3\,MHz$ center frequency (A), and acoustic signals (n=1) making up spatial sensitivity pattern and background signals (B). Note the background acoustic signal shows noise. 95
6.8 Length (A), Diameter (B) and absorption-inducing line source embedded in gelatin (C). 97
6.9 Summed photoacoustic image captured through the in-house setup of phantom containing the line source absorber. 98
6.10 Height (A), Width (B) and final geometrically-complex source embedded in gelatin (C) 99
6.11 PA image of complex source embedded in gelatin formed from in-house setup 100
6.12 Mean RF signals of top- and bottom-lines of the geometrically-complex absorber (A), simulated convolution result of a line absorber with a gaussian light source (B) and simulated convolution result of a line absorber with a donut-shaped light source (C) 101
6.13 Geometrically-complex phantom embedded in gelatin (width of each line is $1mm$) 103
6.14 PA image of scaffold in (A) 0% fat, (B) 0.01% fat, (C) 0.02% fat, (D) 0.05% fat, (E) 0.1% fat. Time-gating was not performed while processing this data. All images acquired with in-house setup. . . . 104
6.15 Design of staircase phantom (all dimensions in mm) (A) and staircase phantom embedded in emulsified gelatin-oil at varying depths from the transducer (B) 107

6.16 PA image of staircase immersed in water, with analysis regions shown (A), PA image of staircase immersed in lipid, with analysis regions shown (B), FWHM of absorbing lines in water as a function of probe-to-absorber distance (C) and FWHM of absorbing lines in lipid as a function of lipid depth and probe-to-absorber distance (D) 108
6.17 Height (A) and Width (B) of absorber immersed between clear layers of gelatin (C) and a talcum-gelatin mix (D), each layer 4 mm deep (E) 110
6.18 PA Image produced as a result of light–clear-gelatin–absorber–talcum-gelatin–receiver (A) and light–talc-gelatin–absorber–clear-gelatin–receiver (B) 111
6.19 Excavated bone revealing absorber (A) and side view with absorber (left) and bone (right) (B) 112
6.20 Ultrasound penetration through bone with 1 OD filter (A), 2 OD filter (B), 3 OD filter (C). Light penetration through bone (B) . . . 113

List of Tables

4.1 Optical properties of tissue types used in Monte Carlo simulations . 42

4.2 Simulation parameters for a point source absorber in water 43

4.3 Simulation parameters for a point source absorber in soft tissue . . 44

4.4 Simulation parameters for an intracranial hemorrhage model 44

4.5 Simulation parameters used in k-wave for a point-source absorber in water 51

4.6 Simulation parameters used in k-wave for an intracranial hemorrhage model 53

5.1 Immersion transducer (Olympus Corp.) specifications 68

5.2 Annular or ring transducer (Steiner & Martin Inc.) specifications . 71

Acronyms

ANSI American National Standards Institute

BOLD Blood Oxygen Level-Dependent

CT Computed Tomography

DCE Dynamic Contrast-Enhanced

DOI Diffuse Optical Imaging

DWI Diffusion-Weighted Imaging

EM Electromagnetic

fMRI functional Magnetic Resonance Imaging

ICH Intracranial Hemorrhage

LED light emitting diode

MFP mean free path

MPE Maximum Permissible Exposure

MRI Magnetic Resonance Imaging

Nd:YAG neodymium-doped yttrium aluminum garnet; Nd:$Y_3Al_5O_{12}$

PACT Photoacoustic computed tomography

PAI Photoacoustic Imaging

PET Positron Emission Tomography

RF Radiofrequency

SNR signal-to-noise ratio

SPECT Single Photon Emission Computed Tomography

TAI Thermoacoustic Imaging

TMFP transport mean free path

US Ultrasound Imaging

Chapter 1

Preface

This thesis begins with a general introduction of existing structural and functional imaging techniques, leading into establishing the need for building a novel *Photoacoustic Imaging* (PAI) system. Next, fundamentals of PAI are discussed, starting with the required characteristics of the input *Electromagnetic* (EM) energy, absorption and penetration of this energy in biological tissue, and finally, the generation and propagation of the acoustic wave.

The goal of this thesis is to describe the design, development and testing of a PAI system as a macroscopic imaging system. Therefore, the scope of the introductory Clinical Imaging section in Chapter 2 is limited to macroscopic imaging methods that are able to reliably image more than $1\,cm$ beyond the superficial layers of the body, and that are currently being used routinely in clinical settings. Microscopic imaging, spectroscopic imaging and tomographic (3D) image reconstruction are also considered beyond the scope of this thesis.

Chapter 3 presents the theoretical background of PAI, outlining the conversion

of light energy to thermal energy, resulting in the generation of acoustic waves that are detected outside of the body. Simulations are presented in Chapter 4. The results of the simulations suggest that the PA probe may be appropriate for the application of detection of intracranial hemorrhages in mind, and establish guidelines for the experimental design of the PA system.

Chapter 5 explains the hardware and software development of the PA system, outlining the components used for the experiments. Chapter 6 gives the results of experiments where $6ns$ pulses from a Nd:YAG laser are used to generate photoacoustic signals from a variety of phantoms.

Finally, Chapter 7 discusses limitations in the hardware used for the PA system and opportunities for improvements in the experimental techniques used in this project, along with a conclusion.

Chapter 2

Introduction

2.1 Clinical Imaging

From the first X-ray *Computed Tomography* (CT) to *Diffuse Optical Imaging* (DOI), advances in macroscopic imaging methods have transformed the delivery of medicine by offering a wealth of information about the human body. Today, a wide variety of imaging techniques can be found being utilized in clinical settings for their different capabilities. In any imaging modality, there are trade-offs, and the choice to utilize one imaging modality over another is primarily dictated by clinical application needs. Currently, structural imaging for gross anatomy can be obtained through CT, *Magnetic Resonance Imaging* (MRI) and *Ultrasound Imaging* (US). *Positron Emission Tomography* (PET) and *Single Photon Emission Computed Tomography* (SPECT) are often more commonly used to assess metabolic activities within tissues but utilize radioactive compounds (albeit in low doses) to provide signal. Less common approaches in current clinical settings include *functional Magnetic Resonance Imaging* (fMRI) and DOI.

Structural information can be quickly obtained with X-ray CT. For neurological imaging, CT offers high tissue penetration depth and good spatial resolution, but is limited by low sensitivity in lesion detection. While CT can offer information quickly in emergent situations such as an acute stroke or traumatic brain injury, it requires exposure to ionizing radiation in the form of X-rays (Caceres and Goldstein 2012). X-ray radiation poses a health hazard and is additive to a patient's lifetime risk of radiation-associated cancers (González 2011). Even though this risk is small compared to the benefits of a CT scan, the considerations can be significant for young patients, or in cases where sequential monitoring is warranted (Brenner et al. 2001; Griffey et al. 2009). MRI can overcome this disadvantage by utilizing a magnetic field and non-ionizing radiofrequency (RF) waves, while offering high penetration depth and good spatial resolution. Slow imaging speed and high equipment costs are considerations for MRIs. MRIs currently have low availability in critical medical situations, and are entirely unavailable in some facilities (Caceres and Goldstein 2013). Lastly, US can provide good spatial resolution without ionizing radiation, fast imaging speed, portability and is relatively inexpensive (Sistrom and McKay 2005). However, US has relatively low inherent contrast since it is based on detection of mechanical properties in tissues. It is also limited in its sensitivity and ability to image through bone, due to the high scattering and attenuation of bone, limiting neurological applications.

Functional information such as glucose metabolism can be readily obtained by Positron Emission Tomography (PET). PET has high sensitivity, but is limited by reduced spatial resolution, low temporal resolution and the need for administrating radioactive tracers into the body to assess tissue metabolism compared to MRI.

Whereas PET uses contrast agents containing positron-emitting radionuclides, SPECT uses radionuclides that decay via gamma-ray emissions and generally have longer decay half-lives. Nonetheless, both modalities are still limited by the need for radionuclides and have lower spatial and temporal resolution. MRI also offers functional imaging capabilities through *Dynamic Contrast-Enhanced* (DCE) MRI for perfusion imaging, *Blood Oxygen Level-Dependent* (BOLD) MRI for blood oxygenation and flow information, and *Diffusion-Weighted Imaging* (DWI) for diffusivity (Marinovich et al. 2012). Diffuse Optical Imaging (DOI) is another technique that is still under development and has yet to translate to clinical use (Hoshi and Yamada 2016). It utilizes light in the near infrared spectral region to measure the optical properties of physiological tissue. Fluorescence- and near-infrared-based optical imaging have been extensively explored for microscopic (`<1cm`) molecular imaging (Di Leo et al. 2017). DOI can provide high resolution and high functional contrast due to the differential absorption of near-infrared radiation in endogenous tissue markers, effectively providing functional information such as tissue oxygenation. The use of non-ionizing radiation and non-invasive functional imaging makes optical imaging an attractive modality for macroscopic imaging, however this application is limited by optical scattering in soft tissues that degrades spatial resolution significantly with depth (Hoshi and Yamada 2016).

2.2 Multimodality Imaging

Due to limitations in single modality imaging systems, there has been a large interest in combining them through through hardware or software fusion platforms

to address shortcomings of each technology. Nuclear medicine techniques for hybrid imaging include PET-CT, SPECT-CT and PET-MRI (Martí-Bonmatí et al. 2010). Together, these modalities provide good spatial resolution (through CT or MRI) and high sensitivity (through PET or SPECT). SPECT-CT and PET-CT have become ingrained in routine clinical practice for diagnostic and therapeutic oncology. While indispensable, they are still limited by the use of even more ionizing radiation than when used singly, especially in therapeutic settings.

Other multimodal systems are under development, and have the potential to lower ionizing radiation exposure. For instance, PET-MRI systems offer lower ionizing radiation, however they have limited availability and high equipment cost (Martí-Bonmatí et al. 2010). Further lowering exposure to ionizing radiation, MRI-US hardware and software co-registered platforms are currently being investigated for their added benefits in image-guided surgery (Tang et al. 2008). Novel software platforms are still being evaluated clinically for efficacy and advantage over using the modalities singly (Nelson 1999). Furthermore, this hybrid modality still has the limitations of MRI mentioned previously.

Today, a variety of imaging modalities come together to provide the required clinical information. However, there are gaps remaining in medical imaging. For urgent diagnostic neurological applications, such as detection of strokes or traumatic brain injury, CT remains the preferred imaging modality that can be accessed in a timely manner for structural information (Freeman and Aguilar 2012). Therefore, despite the risk of increased ionizing radiation exposure, CT is regarded as providing more benefits than risks, and are still used routinely in the emergency

department. This has led to increased speculation on overuse of CTs in the emergency department, and development of tactics to combat this over usage, such as the Canadian CT Head Rules (Stiell et al. 2005). Additionally, there are no clinical imaging modalities that can provide metabolic information without the use of invasive, injectable radioactive tracers. Beyond offering information already available through existing modalities, the need to investigate alternate modalities comes from the necessity to provide additional information about tissues with the goal of increasing detection sensitivity, increasing resolution and improving therapeutic applications. For instance, there are non-ionizing *Electromagnetic* (EM) radiation absorption properties of tissues related to their physiological and pathological states that are yet to be exploited clinically. Exploring new modalities with the use of non-ionizing EM radiation may provide radiological medicine with new structural and functional methods of imaging that could be useful in diagnosis and tracking disease progression.

2.3 EM-induced Acoustic Imaging

EM radiation-induced acoustic imaging offers non-invasive and cost-effective imaging using non-ionizing radiation, and has the potential to overcome many gaps currently present in medical imaging. First, photoaocustic imaging systems can image optical biomarkers such as blood. This optical absorption provided by photoacoustic imaging is an independent imaging contrast absent from other imaging modalities such as US, X-Ray CT, DOI and MRI. Second, imaging variants of hemoglobin (oxy-hemoglobin, deoxy-hemoglobin, methemoglobin) with multi-spectral light is

a possibility with EM-induced acoustic imaging. This has the potential to reveal information about lesion staging and hypoxia, which is also absent from current imaging modalities. Third, EM-induced acoustic imaging systems have the potential to be portable and small-sized. This presents an opportunity for these systems to be placed closer to bedside for monitoring patients, with paramedics in ambulances and at non-medical sites (for example, at football fields and older-adult care homes for brain injury detection).

The existing modalities within EM-induced acoustic imaging include *Thermoacoustic Imaging* (TAI), where acoustic waves are induced due to the absorption of microwave and *Radiofrequency* (RF) energy, and *Photoacoustic Imaging* (PAI), where acoustic waves are induced due to the absorption of visible and near-infrared components of the EM spectrum. The theoretical principal behind these imaging modalities is described as the photoacoustic or thermoacoustic effect. As an object absorbs energy (thermal or EM), the absorbed energy converts into heat, and the temperature of the object rises. The increased temperature results in thermal expansion, generating broadband acoustic waves originating from the point of absorption. Strong endogenous contrast in images is created because tissues absorb energy differently, depending on their dielectric properties in TAI, or on concentration of natural chromophores containing hemo-pigment, cytochrome pigment or melanin pigment in photoacoustic imaging (Li and Wang 2009; Sun and Chuang 2012). Absorption of energy in tissues ultimately results in acoustic waves which can be detected outside of the body. Even though virtually any type of EM wave can be used to generate this effect, no other portion of the EM spectrum seems practical for hybrid acoustic imaging. Terahertz rays that lie between microwave

and near-infrared waves do not penetrate biological tissue sufficiently due to water-dominated absorption (see Fig. 2.1). EM waves with frequencies higher than the visible region, such as Ultraviolet (ionizing radiation), have high photon energy and are harmful to tissues (Xu and Wang 2006a), although X-Ray induced acoustic tomography has been investigated for visualizing deep-seated micro-calcifications that are beyond the limitation of emerging non-ionizing imaging strategies (Xiang et al. 2016). While there are a wide variety of clinical applications that could benefit from TAI and PAI, these imaging modalities are especially attractive for brain imaging. Currently, US is the only non-ionizing imaging modality that is used for brain imaging in minimal applications such as the use of transcranial doppler for vasospasm detection (Tsivgoulis and Alexandrov 2016). Compared to US, in EM-induced acoustic imaging, the acoustic source is induced by EM absorption; hence, only one-way distortion of the acoustic wave due to the skull is expected. In US, both the transmission and reception of acoustic waves is affected by the skull.

In this manner, these modalities combine purely microwave, RF or optical imaging with commonly used US, resulting in an enhancement of US. US alone relies solely on acoustic impedance mismatch between different tissue types which provides weak contrast, reducing its diagnostic sensitivity for many applications. Furthermore, US is unable to image non-mechanical properties of tissues, such as electrical conductivity, oxygen saturation or hemoglobin concentration, which are useful in detecting pathological tissue states. Hence, the addition of generating endogenous contrast with EM waves to US offers significant advantages over a purely acoustic modality.

The two types of EM-induced acoustic imaging that have been heavily explored are TAI and PAI. These modalities expose tissue to different types of EM radiation in order to produce their respective EM absorption maps. Fundamentally, these modalities work on the same principles once thermal expansion has occurred and the acoustic wave has been generated. However, the two modalities diverge on the tissue properties that they exploit. While a TAI absorption image is related to dielectric properties of tissues, a PAI absorption image is created based upon absorption of specific wavelengths of light by endogenous chromophores in the body (such as the commonly used hemoglobin in the visible spectrum).

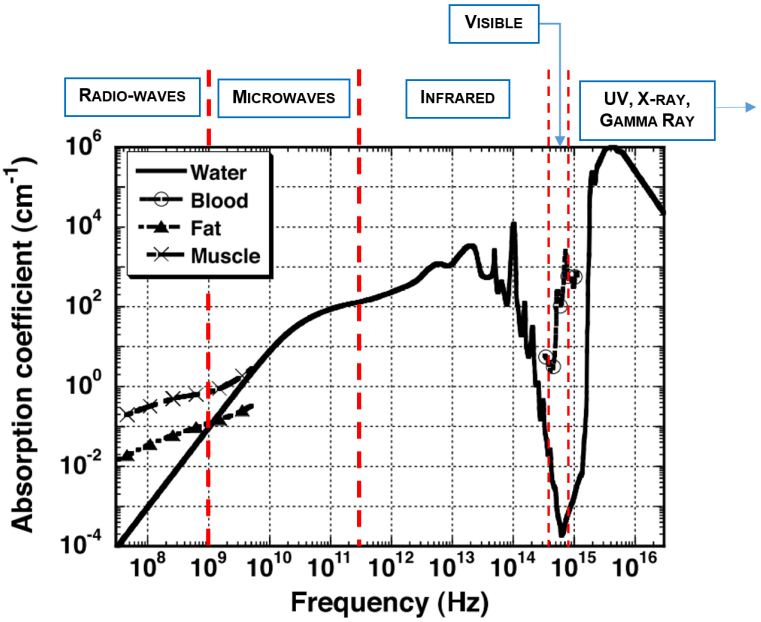

Figure 2.1: Absorption coefficients of water and some biological tissues over the EM spectrum (Ku et al. 2005a)

2.3.1 Thermoacoustic Imaging

TAI involves inducing thermoelastic expansion in tissues with short-pulsed microwave or RF sources (frequencies of `<1 GHz` to `300 GHz`, or wavelengths of `>300 mm` down to `1 mm`). When microwave radiation is absorbed in tissues, the heating and subsequent expansion causes the emission of acoustic signals. These signals are collected to map the distribution of microwave energy absorption in tissues. While TAI images the absorption of microwave energy in tissues, pure microwave imaging detects the reflection of the EM wave in tissue due to differences in dielectric permittivity and conductivity. Even though microwave imaging offers higher contrast than US, pure microwave imaging suffers from poor spatial resolution due to the long wavelength of microwave, which US has the capability to ameliorate (Xu and Wang 2005). This is because the diffraction of acoustic waves, which are the signals being generated in TAI are 2-3 orders of magnitude weaker than the microwave or RF signals generated in pure microwave or RF imaging (Wang 2008). As a result, TAI can provide higher spatial resolution than microwave imaging.

Microwave contrast in absorption maps is provided due to the dielectric properties of tissues, including permittivity and conductivity, which are related to their ionic content and mobility, membrane proteins and free water content. The application of an electric field within a medium causes displacement of charge. For heterogeneous materials such as biological tissues, polarizations in tissues are established and then decay away with time due to the electric field. The dielectric behavior of biological tissues is therefore characterized by a number of relaxation phenomena which give rise to dispersions within the RF and microwave

band. Causes of differing dielectric properties can be attributed to three dispersion mechanisms: λ dispersion in the microwave gigahertz ($10^9\,Hz$) region, β dispersion in the RF kilohertz ($100\,kHz$) region, and α dispersion in the RF low-frequency region. λ dispersion is due to dielectric relaxation of free water in tissues, β dispersion is due to polarization of protein and other organic macromolecules, and α dispersion is due to ionic diffusion processes at the cell membrane (Xu and Wang 2005). At microwave frequencies, water content dominates the dielectric properties of tissue. High water content tissues like muscle, skin and glandular tissue demonstrate higher absorption compared to adipose tissue. However, this also implies that specificity between high water content tissue is limited in microwave TAI (Nie et al. 2008; Tang et al. 2010).

Many research groups have made significant advances in clinically relevant TAI. As can be seen in Figure 2.2, in the $0.2 - 2\ GHz$ frequency range, the relative dielectric constant and conductivity of malignant tissues are about six times more strongly absorbing compared to normal tissue. Though the mechanism for higher absorption in malignant tissues is not well understood, malignant tissues have been proposed to carry cell-membrane glycoproteins, which are mostly bound with increased water and ions, leading to higher absorption of microwave in these tissues (Lazebnik et al. 2007). Kruger et al. 2000 have successfully demonstrated *in-vivo* TAI in breast cancer patients through their feasibility study, however they were limited by a penetration depth of $40 - 45\,mm$, and in their ability to image benign fibroadenomas, most likely due to low absorption at the $434\,MHz$ frequency used and low SNR (Xu and Wang 2006a). Nie et al. 2008 have developed a faster and less-expensive thermoacoustic CT breast imaging system with an improved spatial

resolution of $0.5\,mm$ showing a superior tumor-to-background contrast of $5.5:1$ over the routinely used X-Ray mammography in phantoms. Apart from breast imaging, TAI has also been explored for neurological imaging through the intact monkey skull and brain (Xu and Wang 2006b). $3\,GHz$ microwave pulses were used which were able to penetrate the skull with low distortion, and brain features $3cm$ deep in the head were imaged clearly with ultrasonic transducers that had a center frequency of $1\,MHz$.

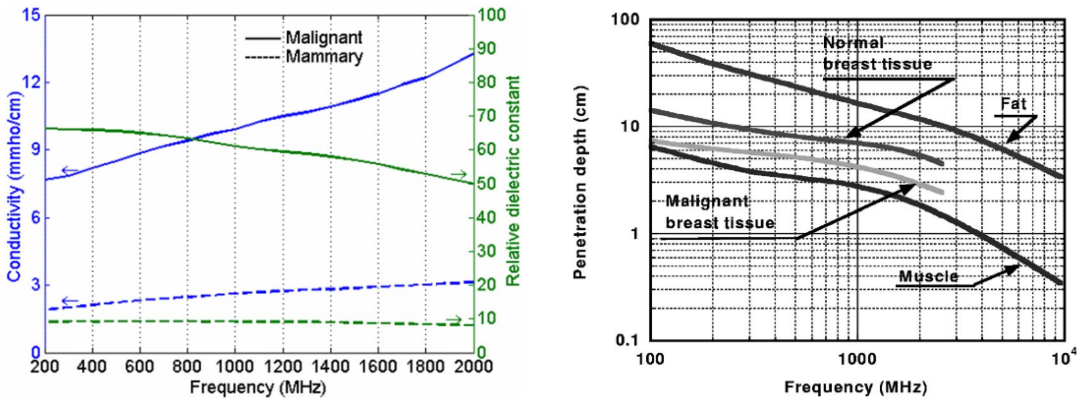

(A) (B)

FIGURE 2.2: Relative dielectric constant and effective conductivity as a function of frequency for human malignant (solid line) and normal (dashed line) breast tissue (Lazebnik et al. 2007) (A), and microwave and RF penetration depths in various tissues (Xu and Wang 2006a) (B)

In order to extend TAI to other applications, complete knowledge of dielectric properties is necessary. Dielectric properties have been reported for a number of biological tissues by Gabriel et al. 1996, however there are significant gaps remaining in the data over the entire relevant frequency range. Shown in Figure 2.2, microwave and RF radiation penetration data for some soft tissues has been assembled by Xu and Wang 2006a. Compared to PAI, TAI has the advantage

of imaging deeper into tissue because the microwave attenuation coefficient of soft tissue is lower than the optical counterpart (Li et al. 2008). However, there are significant challenges remaining in TAI systems, including the selection of a proper microwave or RF frequency with which to initiate the thermoacosutic effect. As can be seen in Figure 2.2 (A) and (B), total conductivity increases with frequency, which means that more energy is absorbed and converted to heat by tissues at higher frequencies leading to a higher *signal-to-noise ratio* (SNR). On the other hand, penetration depth decreases with higher frequencies (Wang 2009). Therefore, choosing the EM frequency for the TAI system can be a challenge. Additionally, long wavelengths of EM energy means that focusing onto smaller regions of interest to generate optimal resolution can be difficult due to diffraction (Xu and Wang 2006a)

2.3.2 Photoacoustic Imaging

When the microwave or RF source in TAI is replaced with a pulsed light source made up of near-infrared ($650-1000\,nm$) or visible ($450-650\,nm$) light, the technique is called photo-acoustic imaging (PAI), also termed opto-acoustic imaging (OAI). PAI is a hybrid modality that brings together optical imaging and US.

Optical Imaging

Pure optical imaging involves exposing tissues to visible and/or near-infrared light, and assessing the absorption and scattering that occurs due to interaction of photons with endogeneous chromophores by counting photons that have traversed

through the tissue and are detected by optical cameras outside of the body. The term "chromophore" refers to any molecule in biological tissue that absorbs light with a characteristic spectral pattern, like hemoglobin. While optical imaging presents a non-invasive and non-ionizing method of structural and functional imaging, it is limited to superficial imaging in tissue due to high scattering events of photons as they propagate deeper into the tissue. Scattering can be described as photon absorption and re-emission without the loss of energy, but potentially with a change in the original direction of the photon. While all EM waves scatter, ultraviolet ($< 450\,nm$), visible and near-infrared scatter more due to photon interaction with cellular structures resulting in blurring of image.

Penetration depth limit of photons can be expressed through two physical parameters. The *transport mean free path* (TMFP) describes the mean propagation distance that it takes for photons, on average, to lose relation to the propagation direction they had before entering tissue. TMFP is influenced by the second parameter, the *mean free path* (MFP) of a photon, which describes the average distance that a photon travels between two consecutive scattering events. While their values vary from tissue to tissue, 1 MFP is $0.1\,mm$ generally, and 1 TMFP is $1\,mm$ (Ntziachristos 2010; Yao and Wang 2014). MFP provides information about the abundance of forward or anisotropic scattering (Mie regime), and the TMFP assesses the degree of unidirectional or isotropic scattering (Rayleigh regime). These parameters are influenced by scattering coefficients (μ_s) of tissues and the anisotropy function (g) which determines backward ($-1 < g < 0$) or forward ($0 < g < 1$) scattering. As photons propagate deeper into tissue, they transition from the zero scattering ballistic regime (under 1 MFP) into the weakly

scattering quasi-ballistic regime (from 1 MFP to 1 TMFP) into the strongly scattering quasi-diffusive regime (from 1 TMFP to 10 TMFP). The diffusive regime is beyond 10 TMFP ($10\,mm$), where scattering is completely isotropic, with photons having no sense of their original direction (Wang 2008).

The upper limit on penetration depth for optical ballistic imaging is 1 TMFP (typically $< 0.5 - 1\,mm$), and imaging beyond this limit is traditionally left to other modalities such as X-ray CT or MRI (Ntziachristos 2010; Mehmet et al. 2009). Diffuse optical tomography is based on multiple-scattered photons and can image in the quasi-ballistic regime, however it has poor spatial resolution.

Basics of Photoacoustic Imaging

PAI presents a solution to image deeper into biological tissue with optical sources by taking advantage of the improved spatial resolution of US. This is because ultrasonic scattering coefficient in tissue is 2-3 orders of magnitude less than the optical counterpart (Wang 2008). PAI can image deeper than optical imaging techniques because the resultant acoustic signal amplitude depends linearly on the excitation-light intensity, and time-resolved acoustic detection can suppress the interference of unnecessary surface signals (Wang and Yao 2016). If the spatial resolution is relaxed to hundreds of micrometers attainable with low-frequency ultrasonic detection ($5\,MHz$), photoacoustic CT can be used to reach the diffusive regime, albeit only a few centimeters deep. Research groups have demonstrated penetration depths of up to $70\,mm$ with internal light illumination and external

ultrasound detection, reducing the problem of high photon scatter seen with external illumination probes (Mitcham et al. 2015). However, this technique is suited to limited invasive procedures such as PAI-guided biopsies or thermal therapy.

While the imaging depth of PAI remains a challenge for whole organ imaging due to optical wave penetration limitations, PAI still proves to be a useful technique for superficial (few centimeters) diagnostic imaging. PAI begins with a short-pulsed light beam (typically laser) made up of visible or near-infrared light irradiating biological tissue. If the wavelength of the light is tuned to an absorption line of the tissue component of interest, the optical energy is absorbed by the target chromophore and most of the energy is dissipated as heat. Absorption is the only way by which light can interact with tissue to induce photothermal effects, such as the photoacoustic effect. Heat is further converted to a pressure rise via thermoelastic expansion of tissue. The initial pressure rise propagates in the tissue as an acoustic wave. Piezoelectric transducers that are in acoustic contact with the sample are used as detectors to measure the amplitude of the resultant photoacoustic wave. Electric signals from piezoelectric detectors are then amplified, digitized and transferred to a computer where an images can be formed (Tuchin 2016; Wang 2008).

Compared to TAI, PAI can provide improved tissue contrast since it relies on absorption of endogenous chromophores such as hemoglobin, myoglobin or cytochrome c oxidation states for absorption maps instead of water content of tissues (Sun and Chuang 2012). Hence, PAI has the ability to provide unique functional information about tissues. Additionally, unlike microwave, there is no centimeter-scale periodic heterogeneity in infrared laser illumination. Therefore,

the low-frequency disturbance can be reduced significantly. Another advantage of using a near-infrared light source is that the SNR can be increased greatly by a significant increase of the illumination energy given the same illumination area. For example, in the brain imaging study of Xu and Wang 2006b, the energy of a single microwave pulse was about $10\,mJ$, and it is easy to find a commercial laser providing a single pulse energy of several hundred milliJoule.

Applications of Photoacoustic Imaging

PAI has been extensively explored and tested for numerous clinical applications. Breast cancer tissue can be detected by TAI as well as PAI, as PAI is sensitive to tumor-related vasculature (angiogenesis) and hemorrhagic infiltration (Valluru and Willmann 2016; Nie et al. 2008; Heijblom et al. 2016). Tumors generally have higher optical absorption since they have higher vascularity than surrounding tissues, which means that they have higher hemoglobin concentration leading to increased absorption of photons in the near-infrared range. One system that exploits this property *in-vivo* is the photoacoustic mammoscope developed by Piras et al. 2010. The laser ($1064\,nm$, $10\,mJ/cm^2$) and ultrasound detector array (diameter of $80\,mm$, 590 elements, $1\,MHz$ centre frequency) operate in transmission mode across the compressed breast. Clinical evaluation of the system showed high sensitivity but low specificity due to high-contrast or abnormally structured areas observed at different locations outside of the tumor volume (Heijblom et al. 2016).

Ex-vivo studies with biopsy samples have also been performed to successfully

detect breast microcalcifications, detect prostate and thyroid cancer (differentiating from benign cancers through significantly increased deoxyhemoglobin content), and detect malignant postmenopausal ovaries with 83% sensitivity and specificity (Kim et al. 2014; Dogra et al. 2013; Dogra et al. 2014; Aguirre et al. 2011). An *in-vitro* study on frozen cervical biopsy samples with a $532\,nm$ laser and $10\,MHz$ ultrasound transducer has shown 94% correlation between staging of cervical cancer and mean optical absorption (Peng et al. 2015). Favazza et al. 2011 have performed an *in-vivo* study to characterize skin lesions with their PAI system.

Non-invasive imaging of the brain with PAI has yet to transition to clinical testing, however pre-clinical studies have shown the utility of diffusive *Photoacoustic computed tomography* (PACT) for deep brain imaging. The deep penetration of PACT can be attributed to the combination of near-infrared optical excitation and low-frequency ultrasonic detection of photoacoustic waves. Wang et al. 2003 have developed a PAI system for structural and functional transcranial neuroimaging of rats with skin and skull (total thickness of $1.4\,mm$) intact. They used a green $532\,nm$ Q-switched Nd:YAG laser ($6.5\,ns$ pulse width, $< 10\,mJ/cm^2$ incident energy density) and an ultrasonic transducer with center frequency of $3.5\,MHz$ ($1mm$ focal diameter) to image interior brain structures $8mm$ beneath the scalp surface clearly. Other groups have image tumor-related vasculature through the skull in rats (Ku et al. 2005b).

When passing through biological tissue, near-infrared wavelengths are known to penetrate deeper than visible light, and absorption and scattering are much lower with longer wavelengths through the dense skull (Jacques 2013; Ugryumova et al. 2004). Furthermore, ultrasound signals propagating through a skull suffer less

distortion at lower frequencies of $0.5-1\,MHz$ (Fry 1977). Hence, Yang and Wang 2008 used a $1064\,nm$ Nd:YAG laser ($<15\,ns$ pulse width, $50\,mJ/cm^2$ incident energy density) and an ultrasonic transducer with center frequency of $1\,MHz$ (unfocused) in an orthogonal configuration. They were able to successfully image brain structures of the rhesus monkey through skull thicknesses of $2\,mm$ with their setup. Similar results have been shown by Nie et al. 2011 in monkeys as well. The adult human skull thickness varies from $2.6\,mm-7.3\,mm$ as one moves across different regions of the skull, while the neonatal skull is much thinner (De Boer et al. 2016). Some groups have successfully the PA effect through the whole adult and infant human brain with skull intact (Nie et al. 2012; Wang et al. 2008; Petrov et al. 2016). Resolution and imaging depth remain key issues for PAI brain imaging, however given the unique functional information and its capability to image with non-ionizing radiation quickly and inexpensively, there is motivation to explore applications in superficial brain imaging with PAI systems that can build upon the ones presented here by exploring different configurations of ultrasound arrays and laser wavelengths.

2.4 Conclusion

PAI has the potential to overcome gaps in current medical imaging by offering a non-invasive and non-ionizing method of structural and functional imaging. Furthermore, PAI may offer functional information that cannot be currently provided by existing modalities. Penetration depth remains a concern for development of PAI systems, however the use of alternative wavelengths and transducers specific

to clinical applications can bring improvements to current systems. Furthermore, trimodal acoustic systems combine PAI and TAI to generate absorption maps from both modalities to take advantage of the long penetration depth of TAI and the unique endogeneous information offered by PAI. Systems have been developed for the purpose of breast cancer imaging (Ke et al. 2012; Ku et al. 2005a).

2.4.1 Novel Application

The focus of this thesis is the development of a PAI system with the possible novel application of imaging *Intracranial Hemorrhage* (ICH) in mind. ICH is defined here as primary or secondary bleeding within the intracranial vault including in the superficial brain parenchyma and surrounding meningeal spaces, resulting from a vast array of diseases such as strokes (lobar, extradural, subarachnoid, subdural), traumatic brain injury, hypertension, etc. Currently, ICH carries the highest risk of severe morbidity and a reported mortality rate of up to 52% (Caceres and Goldstein 2012). Hematomas can enlarge in the acute phase, and an increase in the volume of ICH itself is a significant cause of clinical deterioration leading to neurosurgical intervention (Kazui et al. 1996; Salihovi et al. 2013). The gold standard for monitoring expansion of ICHs is X-Ray CT scans, however the majority of significant hematoma growth occurs between baseline and one-hour CT scans (Brott et al. 1997). Clinical practice recommend initiating surgical evacuation when hemorrhage size has reached $1\,cm$ at the thickest point (Marshall 2009). This necessitates early diagnosis and immediate action for expanding intracranial hematomas since size of hematoma at intervention, and hence time-to-surgery greatly determines patient outcomes. Increasing the frequency of CT

scans for inpatients poses multiple feasibility problems, including personnel time, radiation-associated risks and accessibility for select hospitals. A non-invasive, point-of-care device capable of detecting and continuous monitoring of superficial ICHs has the potential to address this gap in clinical care and improve efficiencies for management of patients presenting with ICH. PAI may be developed into such a device, since it offers functional imaging based on hemoglobin absorption, along with superficial structural imaging.

There are no present photoacoustic technologies that are dedicated towards the detection of ICH. The only commercialized medical device that claims the same application is a near-infrared spectroscopy based technology called the InfraScan (Leon-Carrion et al. 2010). The proposed photoacoustic system may have the potential for increased detection accuracy over its spectroscopy analog since PAI uses information retrieved from multiple scattered photons instead of just ballistic or quasi-ballistic photons that spectroscopy achieves. This allows for detection of photons that have penetrated deeper into the tissue, although US may still be a barrier to penetration depth.

Chapter 3

Fundamentals of photoacoustic imaging

Generation of the photoacoustic effect starts with an object absorbing EM energy in the optical region (visible to near-infrared). Heating with these EM sources needs to be time-variant in order to generate an acoustic wave. Two methods that have been conceived to generate time variant sources are EM pulses provided by lasers (Q-switched Nd:YAG, Ti:Sapphire, dye lasers) and those provided by intensity modulated continuous-wave EM waves provided by *light emitting diode* (LED) (Li and Wang 2009). Short EM pulses are advantageous because they provide a higher *signal-to-noise ratio* (SNR), and permit depth profiling as all signal reaching acoustic detectors after the short pulse has ended can be attributed entirely to the thermoelastic expansion in the region illuminated by the short pulse. Since the pulse energy of LEDs or laser diodes is significantly lower than the energy per pulse of most Nd:YAG laser, more pulses are required to obtain the same SNR since the resultant amplitude of the photoacoustic signal is proportional

to the laser pulse energy (Kolkman et al. 2009). While LEDs as energy sources provide inherently lower SNR and pulse energy, they are lower cost, more portable units, smaller sized, significantly cheaper and have lower cooling and maintenance requirements, thereby making them attractive for superficial imaging (Allen and Beard 2016).

3.1 Optical wave Constraints

In order to effectively generate the photoacoustic effect, an input EM wave must meet thermal confinement and stress confinement conditions. When the heating process with a laser is much faster than the medium expansion rate, the stress is temporarily confined during laser heat deposition, allowing for efficient pressure generation. This thermal confinement condition ensures that the EM pulse width, τ is so short that thermal diffusion during the excitation pulse time can be neglected. If we represent heat dissipation by thermal conduction or the thermal confinement threshold with τ_{th}, the thermal confinement condition enforces the following:

$$\tau < \tau_{th} \tag{3.1}$$

Furthermore, τ_{th} is dependent on d_c, the characteristic linear dimension of the tissue volume being heated (the penetration depth of the EM wave or the size of

the absorbing structure) determining the spatial resolution of the system, and D_T, the thermal diffusivity of the sample, which is $0.14\ \frac{mm^2}{s}$ for most soft tissues:

$$\tau_{th} = \frac{{d_c}^2}{4 \cdot D_t} \tag{3.2}$$

The stress confinement condition ensures that a high thermoelastic pressure (acoustic wave) will be built rapidly in the sample being heated and that the volume expansion of the absorber during the illumination period is negligible. The time for stress to traverse the heated region is dependent on previously defined d_c, and the speed of sound c according to:

$$\tau_s = \frac{d_c}{c} \tag{3.3}$$

Then, the stress confinement condition asserts that the pulse the *Electromagnetic* (EM) pulse width, τ:

$$\tau < \tau_s \tag{3.4}$$

To achieve a spatial resolution of $d_c = 15\ \mu m$, if water is the medium, $c = 1500\ \frac{m}{s}$ and the sample is soft tissue, $D_T = 0.14\ \frac{mm^2}{s}$, then $\tau_{th} = 400\ \mu s$ and the more stringent $\tau_s = 10\ ns$. Hence, the pulse width of an EM source for an effective acoustic signal to be generated in this case must be smaller than $10\ ns$ (Li and Wang 2009).

3.2 Initial Pressure Rise

When both thermal and stress confinement conditions are satisfied, the heated region undergoes fractional volume expansion that is dependent on the isothermal compressibility κ (expressed in Pa^{-1}), the change in pressure p (expressed in Pa), the thermal coefficient of volume expansion β (expressed in K^{-1}), and the change in temperature ΔT (expressed in K), according to:

$$\frac{dV}{V} = -\kappa p + \beta \Delta T \tag{3.5}$$

If both confinement conditions are enforced, the fractional volume expansion during the heating process is negligible. Then, the initial pressure rise p_0 can be written as:

$$\begin{aligned} 0 &= -\kappa p_0 + \beta \Delta T \\ p_0 &= \frac{\beta \Delta T}{\kappa} \end{aligned} \tag{3.6}$$

The local temperature rise ΔT can be expressed as:

$$\Delta T = \frac{\eta_{th} A(r)}{\rho C_p} \tag{3.7}$$

where η_{th} is the percentage of absorbed light converted into heat, $A(r)$ is the

specific optical energy deposition (expressed in J/m^3), ρ is the density of the region, and C_p is the specific heat of the illuminated region at constant volume. Then, combining the pressure and temperature change equation:

$$p_0 = \frac{\beta}{\kappa \rho C_p} \eta_{th} A(r) \tag{3.8}$$

By introducing Γ, the Grunesian parameter (dimensionless), pressure can be expressed in a more concise manner:

$$p_0 = \Gamma \eta_{th} A_e \tag{3.9}$$

$$\Gamma = \frac{\beta}{\kappa \rho C_p}, \text{(Zhou et al. 2016)}$$

Since acoustic speed ${v_s}^2 = \frac{1}{\rho \kappa}$,

$$\Gamma = \frac{\beta {v^2}_s}{C_p} \tag{3.10}$$

$$p_0 = \frac{\beta {v^2}_s}{C_p} A(r) \tag{3.11}$$

For soft tissue at room temperature, $\beta \approx 4 \times 10^{-4} K^{-1}$, $C_p \approx 4 \times 10^3 \frac{J}{kg} K$, and the acoustic speed $v_s = 1.5 \times 10^3\ m/s$. This makes $\Gamma \approx 0.23$ (Li and Wang 2009).

Lastly, note that A_e is proportional to the local optical fluence F (expressed in J/cm^2). Hence, the initial pressure rise can be finally expressed as:

$$p_0 = \Gamma \eta_{th} \mu_a F \tag{3.12}$$

Hence, the initial pressure rise is proportional to the absorption coefficient μ_a and fluence F (Zhou et al. 2016). Γ and η_{th} are often approximated as constants, however they have been shown to be dependent on tissue type (Yao et al. 2014). If a blood vessel (absorption coefficient $\mu_a = 4.3\,cm^{-1}$) in soft tissue ($\Gamma = 0.23$) is illuminated by a pulsed laser with a wavelength of $800\,nm$ and at a fluence $F = 20\,\frac{mJ}{cm^2}$, the initial pressure rise $p_0 = 2.0 \times 10^4\,Pa$, assuming efficient conversion of absorbed light to heat (Li and Wang 2009).

3.3 Pressure Wave Propagation and Detection

Once an initial pressure rise has been generated, it propagates into the medium according to the following wave equation:

$$(\nabla^2 - \frac{1}{{v_s}^2} \cdot \frac{\partial^2}{\partial t^2}) p(r,t) = -\frac{\beta}{C_p} \frac{\partial H(r,t)}{\partial t} \tag{3.13}$$

where ∇^2 is the Laplacian operator calculating the divergence of the gradient of the pressure function in three dimensions, $H(r,t)$ is the heating function defining the thermal energy converted at spatial position r and time t by the EM radiation

per unit volume per unit time, C_p is the isobaric specific heat in $\frac{J}{K \cdot kg}$, β is the isobaric volume expansion coefficient in K^{-1}, and v_s is the acoustic speed (Li and Wang 2009).

The heating function can be represented by:

$$H(r,t) = \mu_a \cdot \phi(r,t) \tag{3.14}$$

where μ_a is the absorption coefficient and ϕ is the optical radiation fluence rate.

The pressure wave equation can be solved by using a Green function approach. The Green function in an infinite homogeneous and non-viscous medium satisfies:

$$(\nabla^2 - \frac{1}{{v_s}^2} \cdot \frac{\partial^2}{\partial t^2}) G(r,t;r',t') = -\delta(r-r')\delta(t-t') \tag{3.15}$$

The Green function can be solved as:

$$G(r,t;r',t') = \frac{\delta(\frac{t-t'-|r-r'|}{v_s})}{4\pi|r-r'|} \tag{3.16}$$

where r represents the spatial location at which pressure is being detected, and r' represents the spatial location at which the initial pressure rise occurred. Using this, pressure detected $p(r,t)$ can be solved for in the photoacoustic wave equation:

$$p(r,t) = \int dt' \int dr' G(r,t;r',t') \frac{\beta}{C_p} \frac{\partial H(r,t)}{\partial t}$$
$$p(r,t) = \frac{\beta}{4\pi C_p} \int dr' \frac{1}{|r-r'|} \frac{\partial H(r', t - \frac{|r-r'|}{v_s})}{\partial t}$$
$$p(r,t) = \frac{\beta}{4\pi C_p} \frac{\partial}{\partial t} \int dr' \frac{1}{|r-r'|} H(r', t - \frac{|r-r'|}{v_s}) \tag{3.17}$$

Under stress and thermal confinement conditions, the heating function can be treated as a delta function $H(r,t) \approx A(r)\delta(t')$ and $|r-r'| = v_s t$, yielding:

$$p(r,t) = \frac{\beta}{4\pi C_p} \frac{\partial}{\partial t} [\frac{1}{v_s t} \int dr' A(r') \delta(t - \frac{|r-r'|}{v_s})] \tag{3.18}$$

In section 3.2, it was established that:

$$p_0 = \frac{\beta {v^2}_s}{C_p} A(r) \tag{3.19}$$

Hence, the detected pressure in terms of the initial pressure rise p_0 can be written as:

$$p(r,t) = \frac{1}{4\pi {v^2}_s} \frac{\partial}{\partial t} [\frac{1}{v_s t} \int dr' p_0(r') \delta(t - \frac{|r-r'|}{v_s})] \tag{3.20}$$

Using a spherical source centered at r_s with radius a uniformly illuminated by a laser source as an example, the spherical absorber will produce an initial pressure

of:

$$p_0(r) = A_0 U(a - |r - r_s|) \tag{3.21}$$

where A_0 is the amplitude of the initial pressure and $U(x)$ is the step function with $U(x) = 1$ when $x \geq 0$, and $U(x) = 0$ when $x < 0$. The acoustic pressure at spatial location r_0 and time t emitted from this spherical source is:

$$p(r_0, t) = A_0 U(a - |R - v_s t|) \frac{R - v_s t}{2R} \tag{3.22}$$

where $R = |r_0 - r_s|$. Figure 3.1 shows the characteristic N-shaped pressure wave that would be detected at a distance of $20\,mm$ from a uniform spherical source with a radius of $2.0\,mm$, assuming an acoustic speed $v_s = 1.5\,\frac{mm}{s}$, and a unit initial pressure.

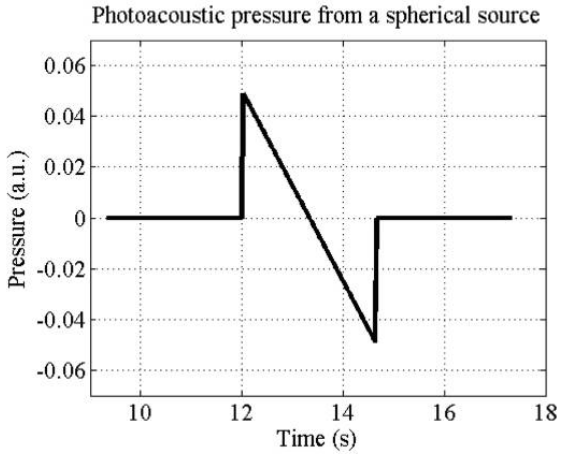

FIGURE 3.1: Photoacoustic pressure wave generated by a spherical source (Li and Wang 2009)

The photoacoustic pressure wave generated as a result of the photoacoustic effect always has a bipolar shape, with both a positive and negative amplitude. Its amplitude is inversely proportional to the distance from the absorber that created the photoacoustic wave, and directly proportional to the size of the absorber. The temporal width of the photoacoustic pressure wave is proportional to the absorber size. Smaller objects will lead to higher frequency components (shorter temporal width) in the detected pressure wave (Diebold et al. 1991; Li and Wang 2009).

Finally, the propagating photoacoustic pressure wave can be captured with an acoustic detector. This pressure wave will travel at the speed of sound $v_s \approx 1500\,m/s$ through a medium such as water, and the pressure wave producing source will be located at a distance $d = v_s t$ away from the face of the transducer, where t is the time that the wave arrives at the transducer after the laser impulse responsible for creating the photoacoustic effect. In practice, acoustic detectors can be hydrophones or piezoelectric transducers that generate electricity when subjected to pressure change, as is the case when the propagating photoacoustic pressure wave reaches and imparts energy onto the transducer. In the N-shaped wave shown in Figure 3.1, if the absorbing spherical source is immersed in a medium in which $v_s = 1.5\,mm/s$, the source producing the wave will be located $18\,mm$ away from the face of the transducer.

3.4 Absorption and Tissue Absorbers

Once an appropriate visible ($380\,nm - 750\,nm$) or near-infrared ($750\,nm - 2500\,nm$) wave source has been selected and EM wave constraints are met, photons in the

laser beam can be optimally absorbed by tissue to create the photoacoustic effect. In order to understand light transport within tissue, two equations of transmitted fluence $\phi(d)$ (expressed in expressed in W/cm^2) can be described:

$$\phi(d) = \phi_0 e^{-\mu_a d}, \text{in the ballistic regime} \tag{3.23}$$

where ϕ_0 is the incident illumination fluence and d is the depth (expressed in cm), and

$$\phi(d) \approx \phi_0 e^{-\mu_{eff} d}, \text{in the diffusive regime} \tag{3.24}$$

where $\mu_{eff} = \sqrt{3\mu_a(\mu_a + \mu_s{}')}$. Hence, light attenuation in the diffusive regime will depend on both the reduced scattering coefficient $\mu_s{}'$ and the absorption coefficient μ_a (both expressed in cm^{-1}). While multiple scattering and absorption processes are responsible for decay of light, absorption is solely responsible for the creation of the photoacoustic effect. The wavelength dependence of $\mu_s{}'$ is significantly smoother compared to μ_a over the visible and near-infrared regions, therefore absorption plays a larger role in attenuating light through tissue at increased depths (Li and Wang 2009). The intensity of signals obtained from PAI will depend on the amount of energy absorbed and transformed into heat and on the thermoelastic properties of the tissue and its surroundings. Absorption of visible and near-infrared light in tissue is due to electronic excitation of aromatic or conjugated unsaturated chromophores. There are a variety of chromophores in the body that absorb light. For example, proteins found in the epidermis contain the

aromatic amino acids tryptophan and tyrosine which have a characteristic absorption band near $270\,nm - 280\,nm$, and epidermal melanin plays a role in limiting penetration depth of light to image beyond superficial layers due to its absorption band from $300\,nm - 1000\,nm$. The number of photons absorbed, dN, between depth x (expressed in cm) and $x + dx$ along the path of a light beam is described by:

$$\frac{dN}{dx} = -\mu_a N = -\rho_M \sigma_{abs} N \tag{3.25}$$

where N is the number of photons penetrating, σ_{abs} is the absorption cross section (expressed in cm^2) and ρ_M is the number of absorbing chromophore molecules per unit volume (expressed in cm^{-3}).

Hence, the number of photons absorbed is directly related to the absorption coefficient μ_a, which is wavelength-dependent. Absorption spectra are often expressed in terms of wavelength dependence of absorption coefficient. Ultraviolet, visible and near-infrared spectra for commonly referred tissue absorbers or chromphores in PAI studies such as water, lipids, oxy- and deoxy-hemoglobin are shown in Figure 3.2. As is the case for all soft tissues, skin absorption in the near-infrared range is mainly determined by absorption of water (Tuchin 2015). Oxy-hemoglobin contained in oxygenated arterial blood supply has its strongest absorption at $415\,nm$ and two secondary absorption bands at $542nm$ and $577\,nm$, Deoxy-hemoglobin contained in deoxygenated venous blood supply has a primary absorption band at $430\,nm$ and secondary absorption at $555\,nm$. The skull is almost entirely composed of cortical bone, whose absorption spectrum has been

reported by Ugryumova et al. 2004 using the integration spheres technique (see Fig. 3.3). Cortical bone absorption is decreased in the near-infrared region compared to the visible region. Absorption spectra of many other endogenous chromophores have been reported in literature (see Fig. 3.4). Heme proteins serve many roles, like oxygen storage and transport (myoglobin in skeletal muscle, and hemoglobin in blood supply), electron transport (cytochrome b and c) and oxygen activation and utilization (cytochrome c oxidase). Cytochrome c oxidase catalyzes the final step in electron transport chain in which oxygen is reduced to water. The absorption of EM energy occurs when this enzyme is reduced allowing the tracking of oxygen utilization directly at the site of ATP synthesis, the mitochondria (Tuchin 2015). These heme proteins have weaker absorption at higher near-infrared wavelengths than at lower visible and ionizing wavelengths. Nonetheless, their spectra have been exploited for functional optical imaging in visible and near-infrared ranges (Wray et al. 1988; Lee et al. 2006; Kahraman et al. 2006).

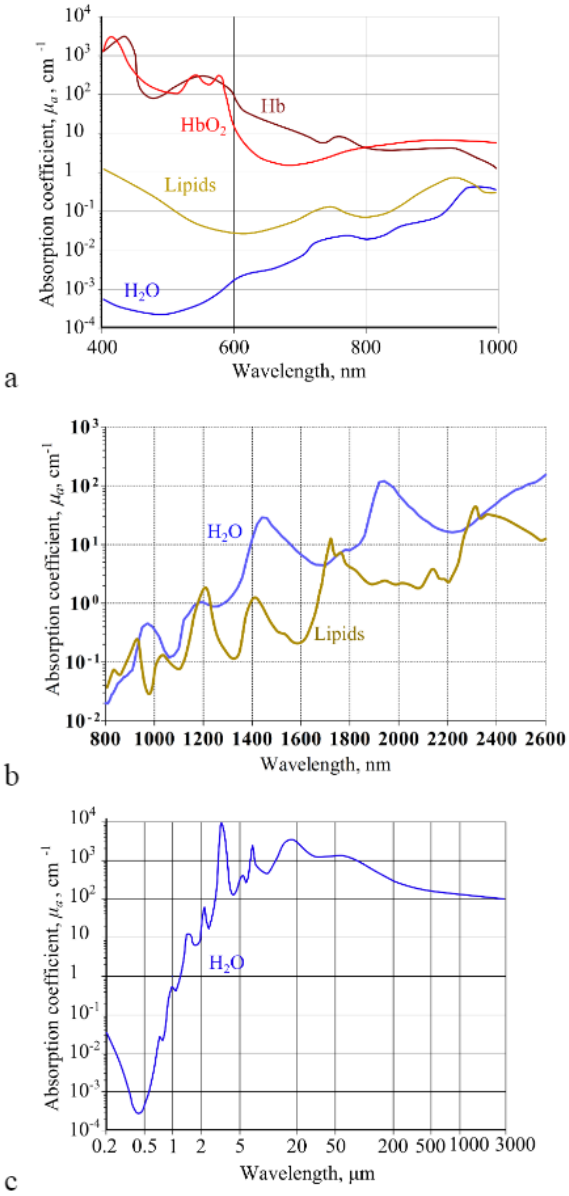

FIGURE 3.2: Absorption spectra of (a) water, lipids, oxy- (HbO_2) and deoxy-hemoglobin (Hb) in the visible and near-infrared range, (b) water and lipids in the near-infrared range, and (c) water in the ultraviolet, visible and near-infrared range in terms of wavelength-dependent absorption coefficient μ_a in cm^{-1} (Tuchin 2015)

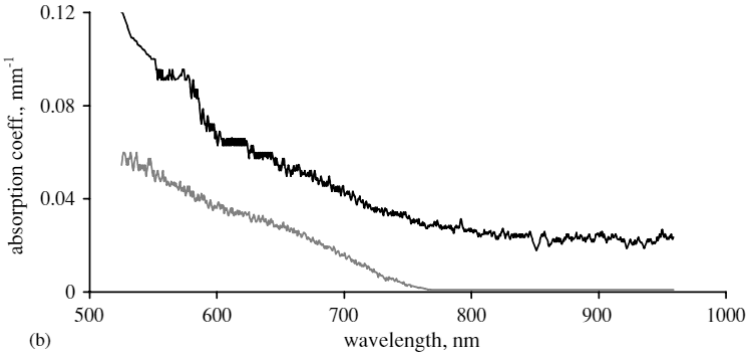

Figure 3.3: Absorption spectra of mineralized (black) and demineralized (grey) cortical bone of horse leg using the integrated sphere technique in the visible and near-infrared range in terms of wavelength-dependent absorption coefficient μ_a in mm^{-1} (Ugryumova et al. 2004)

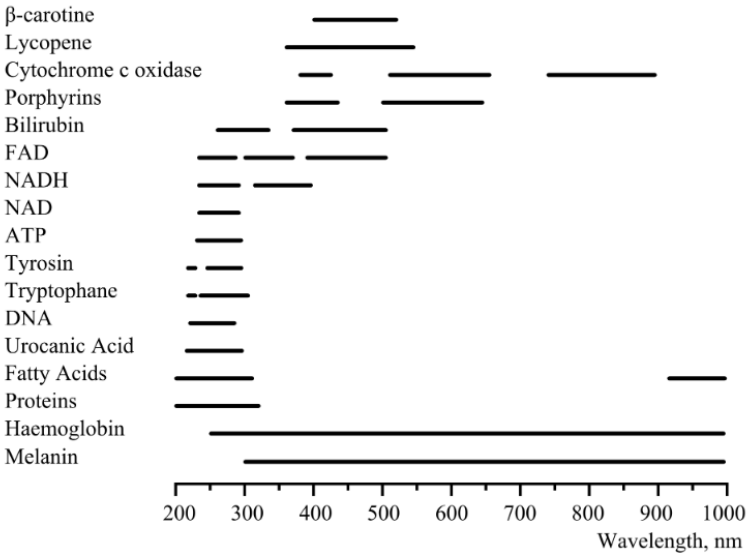

Figure 3.4: Spectral ranges of absorption for other tissue chromophores (Tuchin 2015)

3.5 Laser Safety

For biomedical applications, it is vital to consider laser safety. *American National Standards Institute* (ANSI) has laser safety standards that determine considerations for eye and skin exposure. ANSI standards determine *Maximum Permissible Exposure* (MPE) dependent on wavelength, pulse duration, exposure duration and exposure aperture (see Fig. 3.5 for skin exposure). Single-pulse exposure and average irradiance of the pulse train cannot exceed maximum permissible exposure for applications on PAI for the skin. For instance, consider a pulsed laser source that generates repeated pulses of $532\,nm$ wavelength and $6\,ns$ pulse width. If this source is incident on the same location of the skin, with a $\pi \cdot 1.0\,cm^2$ illumination area for $10\,ms$, ANSI requires that the MPE for each single pulse be less than $20\,\frac{mJ}{cm^2}$, or $62.8\,mJ$ and the averaged power be less than $200\,\frac{mW}{cm^2}$, or $628.3\,mW$. Note the relationship between average power (P_{avg}), pulse energy (E), and pulse repetition rate (f) is $P_{avg} = Ef$. Then, the maximum pulse energy is allowed to be $22.4\,mJ$ if the pulse repetition rate is $28\,Hz$ in this example. For raster scanning applications, the skin is illuminated for less than $10\,s$. The safety limit in these cases for lasers in the $400-700\,nm$ spectrum lasers (derived according to MPE(2) in Fig. 3.5) can be obtained from the following derivation:

$$E \times F^{1/4} \leq 2.75 \times 10^2 \pi d^{5/4} (\frac{\Delta}{N})^{4/3} \tag{3.26}$$

where E is the pulse energy in mJ, F is the repetition rate in Hz, d is the diameter of the illumination region in cm, Δ denotes the scanning step size in

cm, and N is the number of pulses at each step (Laser Institute of America 2007; Wang 2009; Li and Wang 2009).

Wavelength λ (nm)	MPE[1] (mJ/cm^2)	MPE[2] (mJ/cm^2)	MPE[3] (mW/cm^2)
400–700	20	$1100t^{0.25}$	200
700–1050	$20\times10^{2(\lambda-700)/1000}$	$1100\times10^{2(\lambda-700)/1000}t^{0.25}$	$200\times10^{2(\lambda-700)/1000}$
1050–1400	100	$5500t^{0.25}$	1000

Time t is in seconds

[1] $10^{-9}\text{s} \le t < 10^{-7}\text{s}$;
[2] $10^{-7}\text{ s} \le t < 10\text{ s}$;
[3] $t > 10\text{ s}$.

FIGURE 3.5: Maximum permissible exposure values for skin in the visible and near-infrared spectra (Li and Wang 2009)

.

PA applications use a pulsed laser (commonly on the order of nanoseconds) to generate and capture the photoacoustic effect in tissue. Consider a $532\,nm$ laser with a $6\,ns$ pulse width being used to generate a PA signal. According to Figure 3.5, the maximum permissible energy for this application is $20\,mJ/cm^2$ when collecting a single PA signal with a $6\,ns$ laser.

Chapter 4

Simulations

Prior to developing a PAI system, it is essential to simulate the photoacoustic effect in tissue in order to understand the parameters that affect the photoacoustic image, including the optical and acoustic properties of tissue, positioning and characteristics of the excitation laser source, and design and characteristics of the ultrasound sensors. These parameters can be modeled by conceptualizing the photoacoustic effect as a combination of two components: optical and acoustic. Modeling the optical component implies simulating how the energy of a laser pulse is deposited in an optically heterogeneous tissue model. A 3D Monte Carlo program called mcxyz.c is capable of modeling the optical component of PAI (Jacques et al. 2013). This program outputs an energy deposition map of the tissue, which can be used as the input for an acoustic simulation. Since initial pressure is directly proportional to deposited energy, the acoustic program should be capable of simulating propagation of pressure waves based on an initial pressure map through a heterogenous acoustic and optical tissue volume. K-wave is a program that can perform such simulations (Treeby and Cox 2010). By generating

simulated time-domain photoacoustic pressure signals at a variety of positions, a final photoacoustic image can be formed.

4.1 3D Monte Carlo Simulations

The 3D Monte Carlo program mcxyz.c creates a 3D Cartesian grid of voxels which represents the entire volume of tissue to be simulated. Each voxel is assigned a tissue type with its own set of absorption properties (μ_a $[cm^{-1}]$), scattering properties (μ_s $[cm^{-1}]$) and anisotropy of scattering (g, dimensionless) at the particular wavelength of light being simulated (see Table 4.1 for coefficient values used in simulations). Tissue structure $T(y, x, z)$ and simulation parameters (voxel size, number of voxels, wavelength of light, time of simulation, etc.) are used as an input parameters to the C-code mcxyz.c program that executes the simulation and saves a file holding the spatial distribution of the relative deposited energy $A(y, x, z)$ $[\frac{J}{cm^3}$ per J delivered] or $[\frac{1}{cm^3}]$.

Compared to Monte Carlo simulations that can only realistically track several million photons, practical implementation of Nd:YAG lasers leads to the production of many more photons per minute. The energy E (expressed in J) of a photon is directly proportional to its frequency f (expressed in Hz) according to:

$$E_{pulse} = Nhf \tag{4.1}$$

where n is the number of photons produced per pulse and h is Planck's constant ($6.63 \times 10^{-34}\, Js$). For a $532\, nm$ laser that outputs $125\, mJ$ per pulse, 3×10^{17}

TABLE 4.1: Optical properties including absorption coefficient (μ_a), scattering coefficient (μ_s) and anisotropy of scattering (g) of tissue types used in Monte Carlo simulations at $532\,nm$ wavelength. All values obtained from (Jacques et al. 2013), except *obtained from (Jacques 2013).

Tissue	μ_a $[cm^{-1}]$	μ_s $[cm^{-}1]$	g
Air	1×10^{-4}	1	1
Water	3.6×10^{-4}	100	1
Epidermis	16.6	375.9	0.9
Dermis (with 0.2% blood)	0.5	356.5	0.9
Blood	230.5	94.0	0.9
Soft Tissue (Fat)*	2.3	172.8	0.9
Skull	0.1	282.0	0.9
White and Grey Matter	2.3	181.6	0.9

photons are produced per pulse. If each pulse lasts $30\,ms$, 1×10^{19} photons are produced per minute.

4.1.1 Simulating a point absorber

In these simulations, the size of the point absorber was based on the size of an absorber that could also be used experimentally, which was determined to be $200\,\mu m$ (longest dimension). A simple simulation was conducted with a $532\,nm$ laser source, where the point source was chosen to be a sphere of blood with a diameter of $200\,\mu m$ surrounded by water as the medium. Table 4.2 depicts parameters selected for this simulation. Figure 4.1 (A) depicts a point absorber tissue model along with the energy deposition resulting from simulating 8430 photons (B), and 34195 photons (C), as reported by mcxyz. Both simulations show $A \approx 10^{2.7} = 501\,\frac{J}{cm^3}$ per J delivered, or $5 \times 10^{-4}\,J$ per voxel per J delivered at the absorber layer closest to the light source. The total energy deposited in the

entire sphere can be calculated in MATLAB performing this calculation for each voxel constituting the sphere, leading to a total energy deposition of $0.15\,J$ per J delivered in the absorbing sphere (as analyzed from the $2\,hours$ simulation shown in (C) of Figure 4.1). Note that since the point absorber simulated was chosen to be experimentally realistic, the energy deposition is not seen to be homogeneous over the entire vessel cross-section.

Table 4.2: Simulation parameters for a point source absorber in water

Parameters	Values
Wavelength (nm)	532
Laser radius	$0.3\,cm$, diverging to $0.7\,cm$ at $4\,cm$
Run Time	30 min, 2 hrs
Photons per Simulated Pulse	281
Volume Simulated	$(1.5\,cm)^3$
Voxel Size	$(0.01\,cm)^3$

Consider a more practical scenario, such as a low-absorbing medium (like soft tissue) instead of water (approximately zero absorbing) containing a spherical, high-absorbing point source (blood). Simulations show $A \approx 10^{0.22} = 1.66\,\frac{J}{cm^3}$ per J delivered, or $1.66 \times 10^{-6}\,J$ per voxel per J delivered at the absorber layer closest to the light source. The total energy deposited in the entire sphere is $6.0 \times 10^{-4}\,J$ per J delivered.

4.1.2 Simulating intracranial hemorrhage models

After characterizing the point source response of simulations, an intracranial hemorrhage parallel-plate brain model was simulated in mcxyz. (A) of Figure 4.3

Table 4.3: Simulation parameters for a point source absorber in soft tissue

Parameters	Values
Wavelength (nm)	532
Laser radius	$0.3\,cm$, diverging to $0.7\,cm$ at $4\,cm$
Run Time	20 min
Photons per Simulated Pulse	3.0×10^5
Volume Simulated	$(1.5\,cm)^3$
Voxel Size	$(0.01\,cm)^3$

shows the cross-section of the head model with dermal (pink), bone (green) and hemorrhagic (red) layers, followed by gray and white matter. The hemorrhage is simulated as the commonly observed elliptical shape of size 1 cm by 0.5 cm by 0.5 cm. At 532 nm, penetration through dermal layers and bone is minimal, as can be seen in the simulation results in (B) of Figure 4.3, where only 4% of the light is absorbed in the hemorrhagic layer. (C) of Figure 4.3 shows the simulated results of 830 nm (near infrared, NIR) light absorption in the various tissue layers, and shows 40% absorption of the initial light in the top-most layer of the hemorrhage. These simulations show promising results for the use of NIR wavelengths as optical sources for optimal penetration of light through the skull for the detection of intracranial hemorrhages.

Table 4.4: Simulation parameters for an intracranial hemorrhage model

Parameters	Values
Wavelength (nm)	532 and 830
Laser radius	$0.3\,cm$, diverging to $0.7\,cm$ at $4\,cm$
Run Time	10 min
Photons per Simulated Pulse	3.0×10^5
Volume Simulated	$(1.5\,cm)^3$
Voxel Size	$(0.02\,cm)^3$

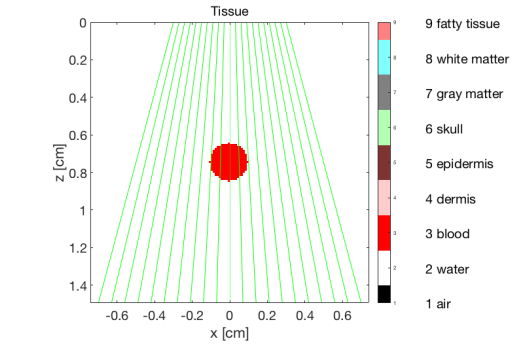

(A)

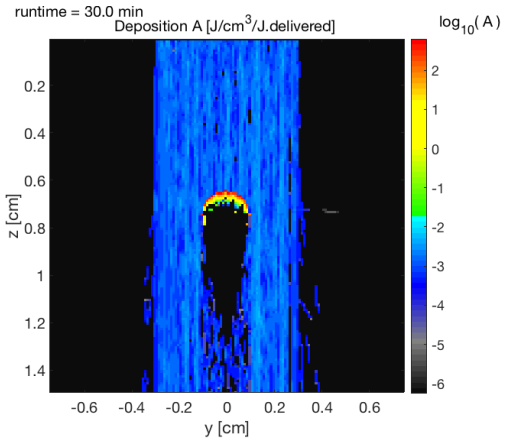

(B)

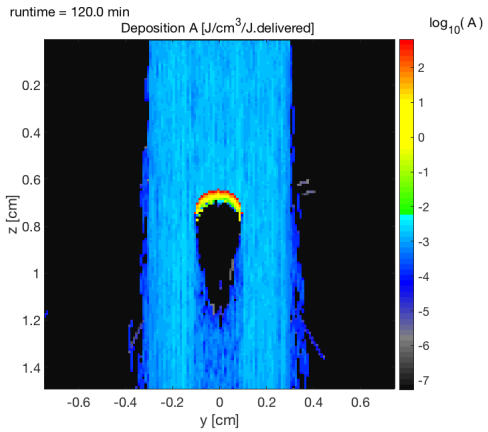

(C)

FIGURE 4.1: Point absorber model with a 200 μm-diameter blood sphere centered in water as the medium; green rays show the path of the 532 nm laser beam (A), energy deposition in the model shown in terms of $log_{10}(A[cm^{-3}])$ when simulated for 30 min (B), and for 120 min (C)

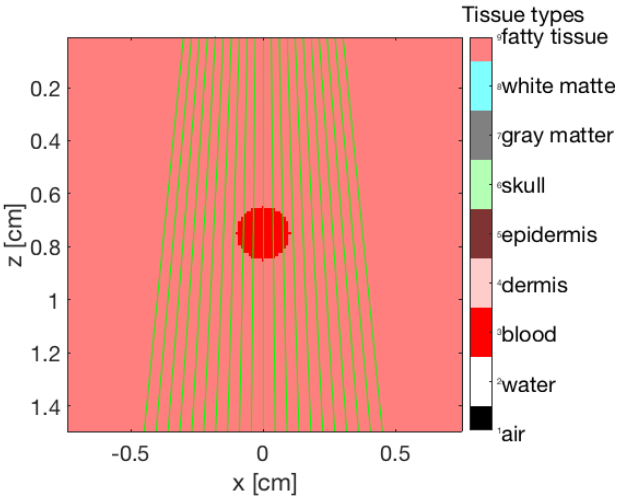

(A)

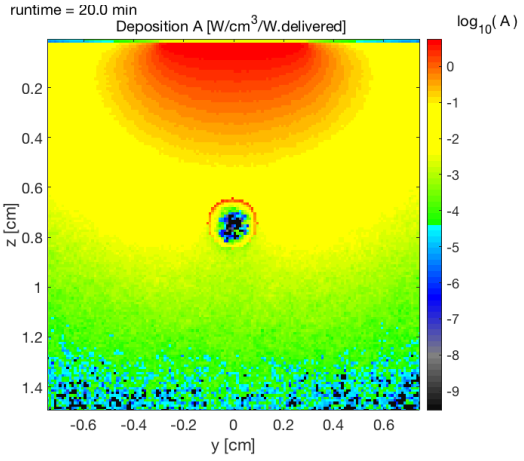

(B)

FIGURE 4.2: Point absorber model with a 200 μm-diameter blood sphere centered in a low-absorbing medium; green rays show the path of the 532 nm laser beam (A), and energy deposition in the model shown in terms of $log_{10}(A[cm^{-3}])$ when simulated for 20 min (B)

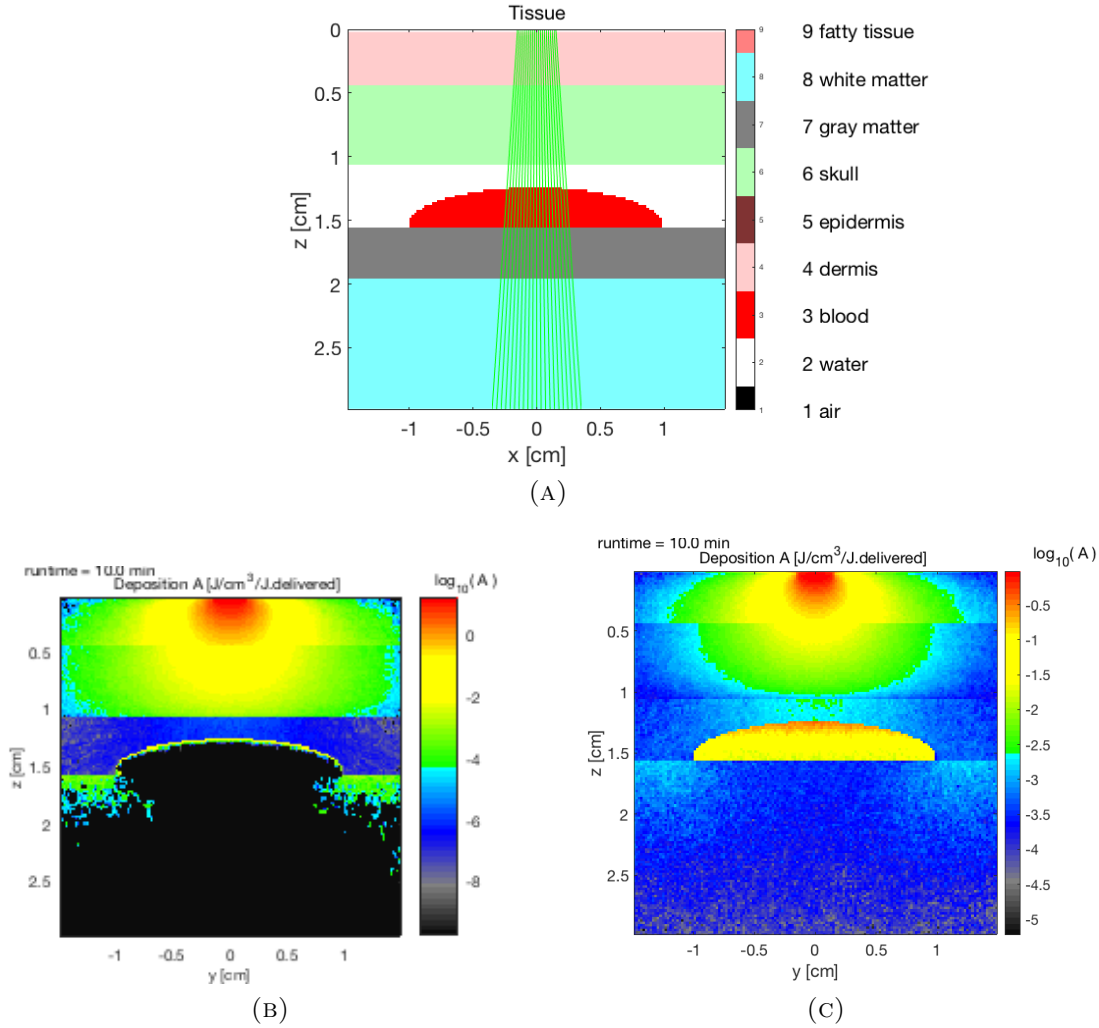

(A)

(B)

(C)

FIGURE 4.3: Intracranial hemorrhage parallel-plate model with an elliptical-shaped $1\,cm$ by $0.5\,cm$ by $0.5\,cm$ hematoma centered within cerebro-spinal fluid (simulated with water); green rays show the path of the laser beam (A), energy deposition in the model shown in terms of $log_{10}(A[cm^{-3}])$ when simulated with $532\,nm$ laser source (B), and with $830\,nm$ laser source (C)

4.2 k-wave Simulations

k-Wave is an open source MATLAB toolbox designed for the time-domain simulation of propagating acoustic waves in 1D, 2D, or 3D. Using an initial pressure distribution p_0 as the source, it provides time domain acoustic and ultrasound simulations in complex and tissue-realistic media. Since the energy deposited into tissue is directly proportional to the initial pressure rise p_0, the energy deposition maps created from mcxyz can be used in k-wave to simulate the photoacoustic signals that are expected from the intracranial hemorrhage model simulated.

The initial pressure p_0 (expressed in Pa) per J delivered can be written in terms of the velocity potential ϕ arriving at time t at a pressure-sensitive detector in the following manner:

$$P = -\rho \frac{\partial \phi}{\partial t} \tag{4.2}$$

where

$\rho \approx 1000 \frac{kg}{m^3}$ is the density of soft tissue. Furthermore, the velocity potential $\phi(t)$ (expressed in $\frac{m^2}{s}$ per J delivered to the tissue) is related to the energy absorbed A. After the appropriate energy has been deposited onto each voxel, a spherical shell of deposited energy A_{shell} (expressed in $\frac{1}{m^3}$) with radius $r = c_s t$ centered on a piezoelectric detector will have launched a stress wave that arrives at the detector at time t. The velocity potential is related to the spatial distribution of energy

deposition A according to:

$$-\phi(t) = \frac{\beta}{4\pi\rho C_p}\frac{1}{\partial t}\int_{r-dr/2}^{r+dr/2}\frac{A_{shell}}{r}4\pi r^2 dr \tag{4.3}$$

where

$r = c_s t$, the distance from shell to detector at time t (expressed in m)

t = time of stress wave arrival at detector (expressed in s)

$c_s \approx 1500\,\frac{m}{s}$ is the speed of sound in tissue

∂t = time step of integration; since $\partial t = \frac{\partial z}{c_s}$, time step can be calculated with bin size and speed of sound in tissue

$C_p \approx 4180\,\frac{J}{kg\cdot\deg C}$

(Jacques 2014)

4.2.1 Ring Detector design

We simulated a ring-shaped detector made up of smaller ultrasonic elements (see Fig. 4.4). The ring detector was simulated to have an inner diameter of $8.5\,mm$ and outer diameter of $15\,mm$ similar to ring-shaped detectors manufactured by Steiner & Martin (see Table 5.2). The ring shape was chosen so that the combined mcxyz and k-wave simulations could simulate the light source central to the ring detector constituting a PA probe.

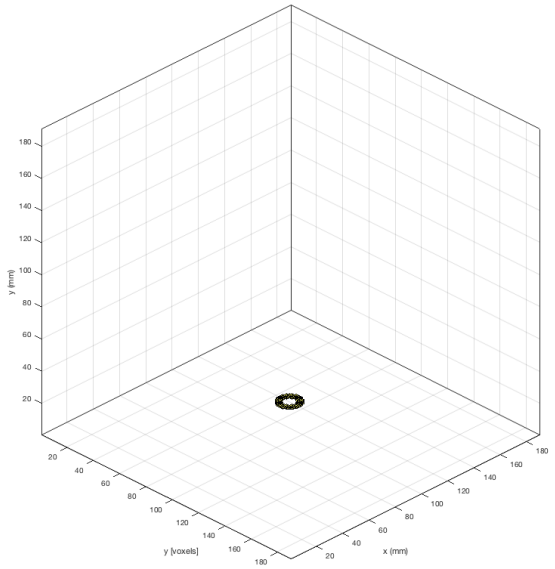

(A)

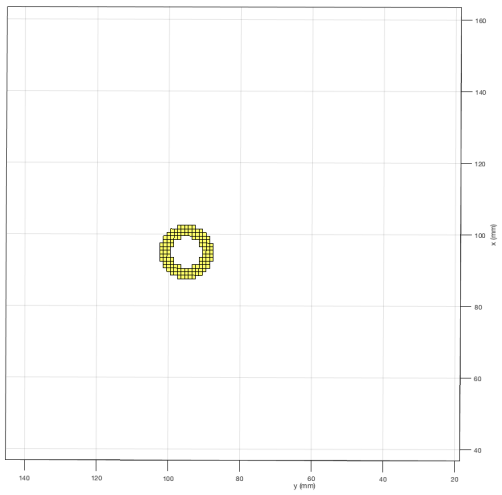

(B)

Figure 4.4: Visualization of the ring sensor mask made up of 116 piezoelectric elements using a 3D plot of a binary matrix, where filled voxels are displayed at the positions of the 1 s. Ring sensor has inner diameter of 8.5 mm an outer diameter of 15 mm.

4.2.2 Simulating a point source

To develop a positive baseline for a photoacoustic signal, the deposition map generated in (B) of 4.1 of a point absorber in water was used as the initial pressure distribution for a k-wave simulation. The parameters of the k-wave simulation are listed in Table 4.5. Each sensor making up the ring-shaped sensor outputted a time-dependent PA waveform. The PA waveforms are overlaid and shown in Figure 4.5. The characteristic N-shaped wave discussed in Section 3.3 and Figure 3.1 is not perfectly represented in Figure 4.5. This is because the energy deposition is inhomogeneous on the chosen point absorber.

Table 4.5: Simulation parameters used in k-wave for a point-source absorber in water

Parameters	Values
Medium speed of sound	$1500\,m/s$
Medium density	$1000\,kg/m^3$
Run Time	38 min
Detector Shape	Ring, inner diameter = $8.5\,mm$, outer diameter = $15\,mm$
Number of elements in sensor	116
Volume Simulated	$(190\,mm)^3$
Voxel Size	$(1\,mm)^3$

4.2.3 Simulating Intracranial hemorrhage models

Using absorption maps generated in Figure 4.3 as inputs for k-wave, and using a ring-transducer made up of 32 elements surrounding the light source in the deposition maps, time-dependent PA waveforms are generated. The results are shown in (A) of Figure 4.6 for the deposition map created with a $532\,nm$ light source and (B) of Figure 4.6 for the deposition map created with a $830\,nm$ light

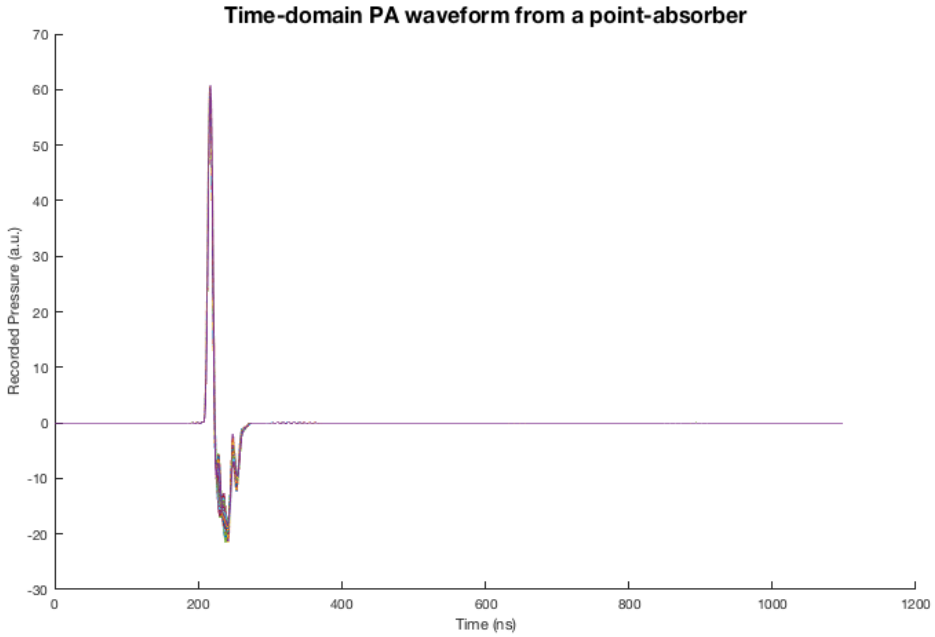

FIGURE 4.5: Time-domain PA waveforms overlaid from 116 element sensors making up the ring sensor shown in Figure 4.4 simulated in k-wave. Input to k-wave simulation was taken from the deposition map shown in (B) 4.1 simulated with a $532\,nm$ light source illuminating PA point source in water.

source. The rise in pressure at $200\,nm$ in (B) of Figure 4.6 (red arrow) can be attributed to intracranial hemorrhage being illuminated by the $830\,nm$ light source. Based on absorption and scattering coefficients of tissues involved in this brain model at $532\,nm$, the results shown in (A) of Figure 4.6 are expected as light is not expected to sufficiently penetrate bone and generate an acoustic signal due to the hemorrhage at $532\,nm$.

To compare, the parallel-plate brain model was simulated at $830\,nm$ without the hematoma in place (see Fig. 4.7). An acoustic pressure rise cannot be seen at $200\,nm$ as is seen in (B) of Figure 4.6, leading us to believe that there is a difference that may be exploited at near-infrared wavelengths between healthy

and hemorrhaged brains.

Table 4.6: Simulation parameters used in k-wave for an intracranial hemorrhage model

Parameters	Values
Medium speed of sound	$1500\,m/s$
Medium density	$1000\,kg/m^3$
Run Time	38 min
Detector Shape	Ring, inner diameter = $8.5\,mm$, outer diameter = $15\,mm$
Number of elements in sensor	32
Volume Simulated	$(190\,mm)^3$
Voxel Size	$(2\,mm)^3$

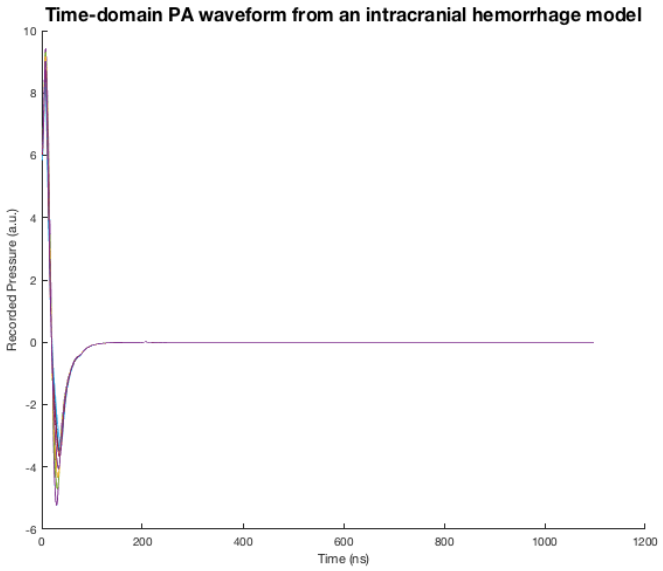

(A)

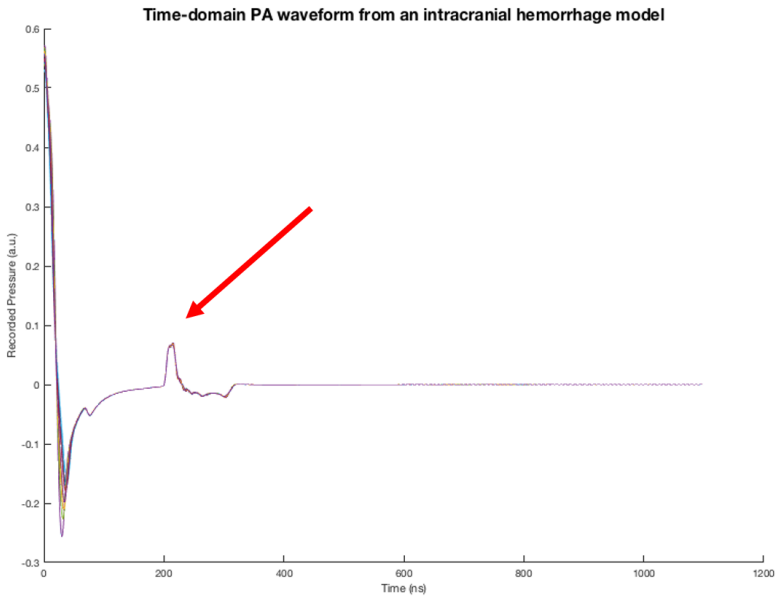

(B)

FIGURE 4.6: Time-domain PA waveforms overlaid from 32 element sensors making up the ring sensor shown in Figure simulated in k-wave. (A) shows results from simulations with input to k-wave simulation taken from the deposition map shown in (B) of Figure 4.3, where the light source is $532\,nm$. (B) shows shows results from simulations with input to k-wave simulation taken from the deposition map shown in (C) of Figure 4.3, where the light source is $830\,nm$. Red arrow points to rise in PA signal at $200\,ns$ attributed to the change in wavelength.

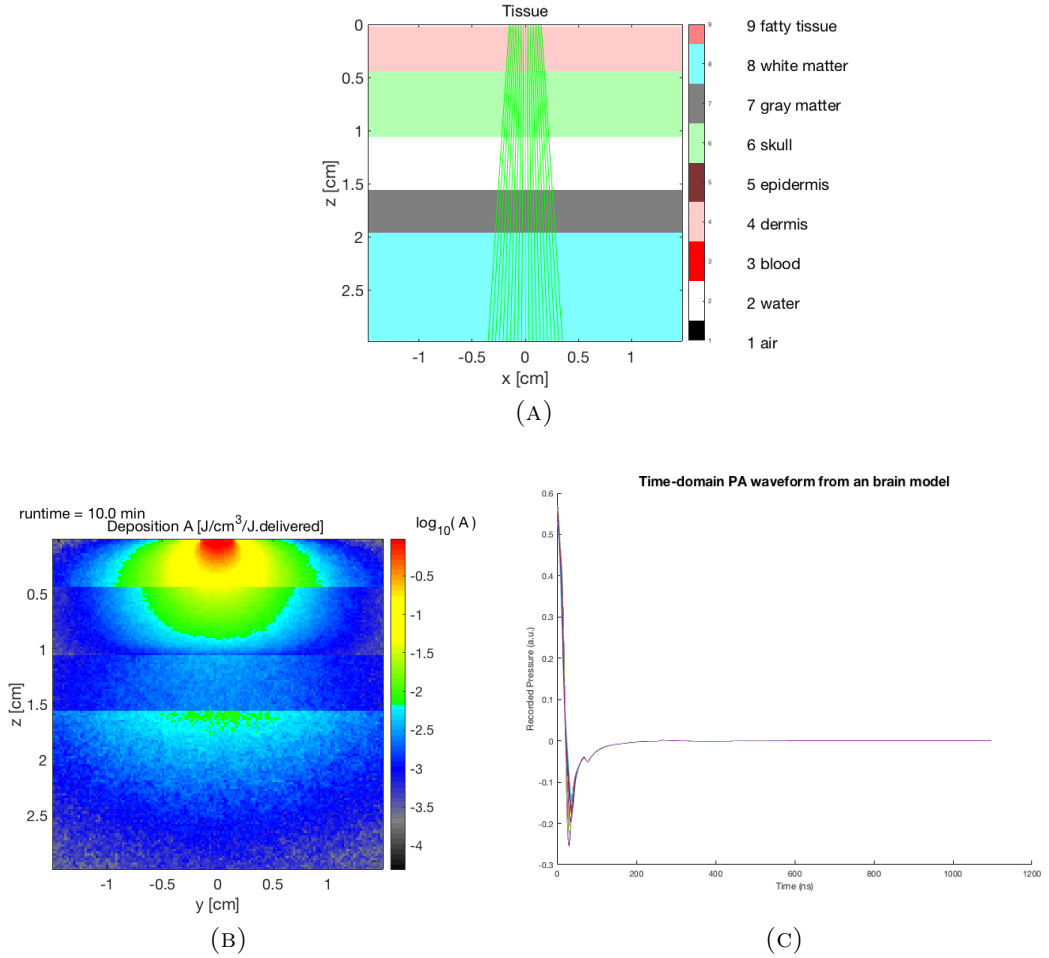

(A)

(B)

(C)

FIGURE 4.7: Healthy brain parallel-plate model; green rays show the path of a 830 nm laser beam (A), energy deposition in the model shown in terms of $log_{10}(A[cm^{-3}])$ (B). Time-domain PA waveforms overlaid from 32 element sensors making up the ring sensor shown in Figure 4.4 simulated in k-wave with input taken from (B) of this figure.

4.3 Conclusion

The results of these simulations confirmed that there are differences in PA signals betweens simple parallel-plate models of healthy and intracranial hemorrhaged brain models. These differences can be best exploited in the near-infrared wavelength range (simulated for one wavelength case at $830\,nm$ here), and are not noticeable at $532\,nm$. A limitation of these simulations, specifically k-wave is that k-wave does not take into account frequency-dependent attenuation of acoustic signals, which may impact the results seen here. The PA probe designed through these simulations led us to proceed into hardware development that would meet these design requirements for this application. While we did not possess a laser capable of generating near-infrared light sources, we proceeded to carry out the development and initial testing as a start towards verifying the use of PA for the application of detection of intracranial hemorrhages.

Chapter 5

Hardware and Software Development

After establishing that optical sources can penetrate features of interest and acoustic signals can be recovered from simulated tissue models, a photoacoustic system was developed with various hardware and software components. The goal of the development was to make a hand-held photoacoustic probe, much like an ultrasound probe, that may be integrated clinically with ease. The complete system is shown in Figure 5.1.

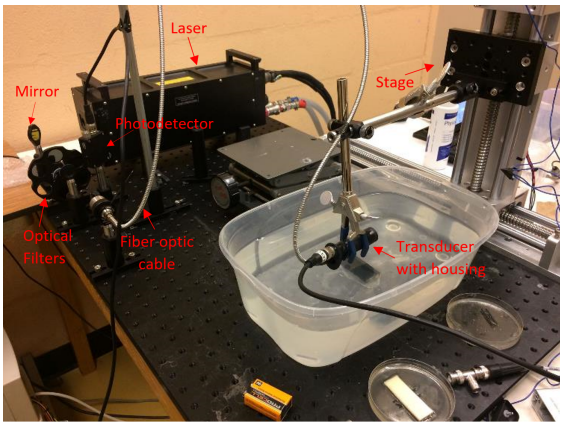

FIGURE 5.1: Experimental setup showing laser, optical filters, fiber optic cable, annular transducer with housing and XY translational stage; not imaged: pre-amplifier and data acquisition card.

5.1 Laser Source

The laser source chosen was a Quantel/BigSky *neodymium-doped yttrium aluminum garnet; Nd:*$Y_3Al_5O_{12}$ (Nd:YAG) laser producing 532 nm wavelength output. The active element of this solid-state laser is a glass host (YAG) doped with a relatively small percentage (1%) of ions (Nd^{3+}) from the rare earth group of the periodic table. Excited states of the atoms for stimulated emission are produced by transferring energy from a flashlamp to pump the gain medium. The laser is operated in Q-switching mode. Quality factor, Q, is defined as the ratio of energy stored in the cavity to the energy loss per cycle, that is, the higher the quality factor the lower the energy loss. In Q-switching, energy is stored by optical pumping while Q is lowered to prevent laser emission. When a high cavity Q is restored, the stored energy is suddenly released in the form of a very short pulse of light (6 ns). The peak power during this pulse exceeds that obtainable from an ordinary long pulse by several orders of magnitude (Koechner and Bass Springer 2003).

The laser energy per pulse is $125\,mJ$, the pulse duration is $6\,ns$ and the circular beam's diameter is $\approx 4.6\,mm$ at the aperture as reported in the datasheet provided by the supplier. This leads to an energy density per pulse of:

$$D_{pk} = \frac{E_{pulse}}{\pi r^2} = 0.8 \ \frac{J}{cm^2} \text{ per pulse}$$

and peak power of:

$$P_{pk} = \frac{E_{pulse}}{t_{pulse}} = 20.8\,MW \text{ per pulse}$$

where t_{pulse} is the pulse duration. The laser is being driven at $28\,Hz$. This leads to an average power of:

$$P_{av} = E_{pulse} R_{rate} = 3.5\,W \text{ on average}$$

where R_{rate} is the repetition rate in pulses per second, or Hz.

5.1.1 Fiber Optic Coupling and Cables

In order to guide the laser beam into a probe-like setup, a combination of a collimator and multi-mode fiber optic cable was used. The collimator was used to couple the laser beam to the fiber optic by focusing light into the fiber optic cable. The collimated beam coming out of the laser is focused through the lens present in the collimator so that the rays converge onto the fiber optic cable (see Fig. 5.2). The fiber optic cable was inserted into a probe housing to make a hand-held probe, as will be discussed in later sections. Glass (silica) fiber optic patch cables were obtained from Thorlabs. These cables use a step-index fiber structure and are $2\,m$ long. They have an inner core ($600\,\mu m$) made from a material with a refractive index that is higher than the surrounding cladding layer, while within the fiber, a

critical angle of incidence exists such that light will reflect off the core or cladding interface rather than refract into the surrounding medium, using the principles of Total Internal Reflection.

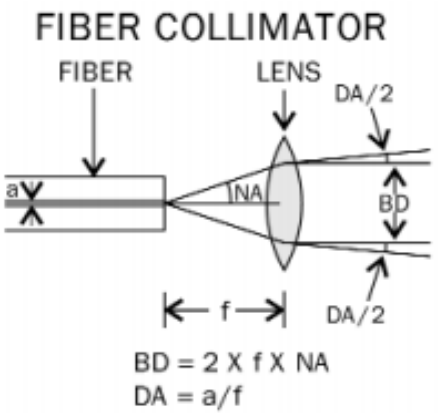

Figure 5.2: Traditional use of a fiber collimator (left to right) where diverging rays from a light source coming out of a fiber are passed through a converging lens to collimate the beam; NA=numerical aperture, f=focal length, a=mode field diameter, BD=beam diameter, DA=divergence angle. Collimator in the PAI system developed is used in reverse (right to left), where collimated rays from the laser are focused onto the fiber optic cable which can be used within a hand-held probe (Best and Sezerman 1999).

Fiber optic cables present many sources of energy loss or attenuation within the fiber. While the discussed sources of attenuation in optical fibers are not comprehensive, they seem to be the most likely causes of non-uniform beam profile for the photoacoustic system developed. Some scattering losses are expected with the use of $532\,nm$ wavelength laser, as scattering losses become significant at shorter wavelengths of the Ultraviolet region and the lower end of the visible spectrum. Optical fibers also experience losses due to changes in the external and internal geometry (bending) of the fiber. Macrobends, such as rolling the fiber in a tight coil, render light near the outer radius of the bend unable to maintain the same

spatial mode profile without exceeding the speed of light (see (A) in Fig. 5.3). Bend radii larger than the suggested $\sim 23\,mm - 30mm$ cause energy to be lost to the surrounding through the cladding.

Lastly, launch conditions originating from improper fiber optic coupling can severely impact performance. Underfilled launch conditions result when the laser beam diameter and numerical aperture at the fiber optic coupling are smaller than the core diameter and numerical aperture of the fiber. Underfilled launches result in light spatially concentrated at the center of the fiber. Overfilled launch conditions result from the opposite circumstances, where the beam diameter and numerical aperture are bigger than those of the fiber optic. This makes overfilled launches even more sensitive to macrobend losses. When light is increasingly guided into the cladding rather than the core of the fiber, a characteristic donut beam profile results at the output of the fiber optic cable (see (B) in Fig. 5.3). The donut profile results from a high number of skew rays that propagate in a helical path along the fiber in cladding that is tangent to the inner caustic of the path compared to meridional rays that pass through the central axis (core) of the fiber after each reflection. The donut beam profile translates to a light intensity cross-section seen in (C) in Figure 5.3 (Thorlabs Inc. 2018).

5.1.2 Photodetector

A photodetector from Thorlabs Inc. (PDA30G) was oriented towards the laser beam to detect the onset of each pulse from the laser. The electrical resistance of the photoconductive material made of lead sulfide is reduced when illuminated with

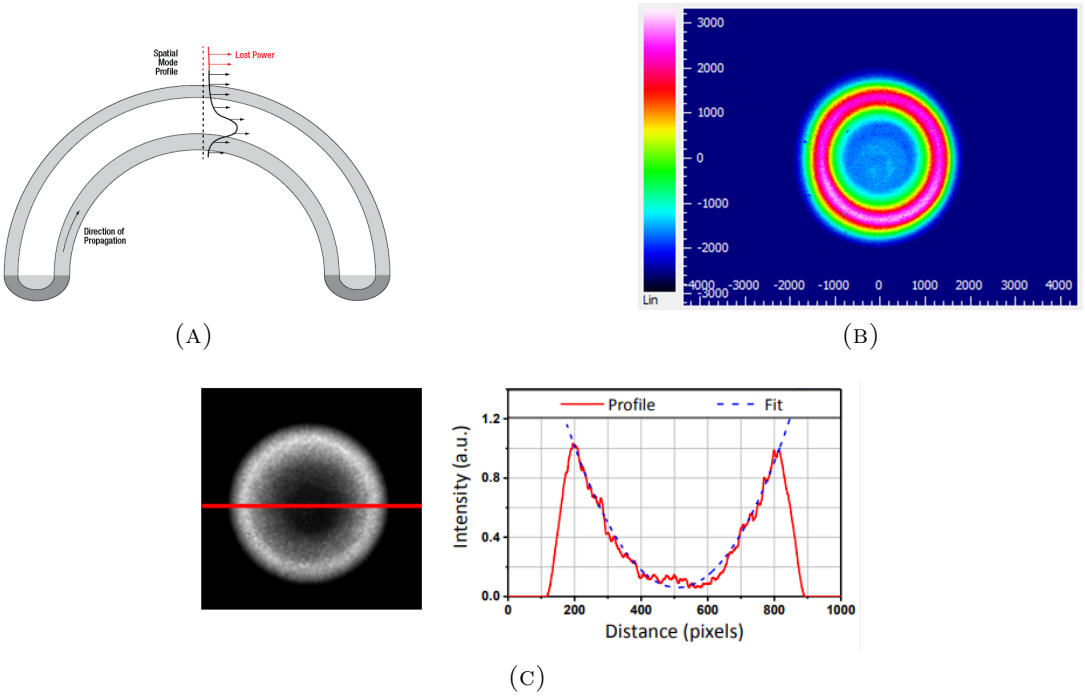

FIGURE 5.3: Attenuation in fiber optic cable due to macrobend loss (A), beam profile measurement showing attenuation of light as it is guided into cladding rather than the core of the optical fiber (B), and cross-section of light intensity across the donut beam profile, with the internal void fitted with the parabola $y = 10^{-5}(x-509)^2 + 00.6$ (C) (Thorlabs Inc. 2018).

light, leading to a change in measured voltage. The photodetector is connected to the data acquisition system and acts as a trigger that allows the subsequent data acquisition card to start collecting acoustic signals only after a pulse has been emitted out of the laser.

5.2 Piezoelectric Transducers

Once light has traversed the fiber optic cable to reach the object being imaged, the photoacoustic effect results in broadband acoustic pressure waves. Two types of ultrasonic waves can propagate energy through a medium: shear (transverse) vibrations, or rarefactions resulting from distortion caused by a force parallel to the object, and longitudinal vibrations, or compressions resulting from forces normal to the object. An ultrasound wave can attenuate as it propagates through a medium, affecting its amplitude and waveform for a variety of reasons including beam spreading, energy absorption, dispersion, transmission at interfaces, and so on. Further weakening of ultrasound energy results from scattering, which is the reflection of sound in directions other than its original direction of propagation, and absorption, which is the conversion of sound energy to other forms of energy. Their combined attenuating effect can be demonstrated through the amplitude change of a decaying plane wave:

$$A = A_0 e^{-\alpha z} \tag{5.1}$$

where A is the reduced amplitude after the wave has traveled a distance z from its initial location where the unattenuated amplitude was A_0. The attenuation coefficient α is experimentally determined, and depends on the sound frequency (NDT Resource Center 2014).

These ultrasound waves can be captured through single-element or phased array piezoelectric transducers that are oriented in the direction of the laser's focus

on the object. A transducer is defined as a device that converts one form of energy into another. A piezoelectric transducer converts mechanical energy, that is, pressure waves to electrical energy (receive mode), or vice versa (transmit mode). A commercial piezoelectric transducer consists of a piezoelectric element, electrical connections, backing materials, front layers and a casing (see Fig. 5.1). The front layers function to protect the active element, or the piezoelectric element against external stresses and environment influences, and to act as an impedance matching layer matched to the medium that pressure waves are being generated in, so that the transfer of ultrasonic energy is optimized. The backing material functions to alter the resonance frequency of the piezoelectric element and dampens unwanted ultrasonic waves reflected back from the back wall of the element (Ihara 2008).

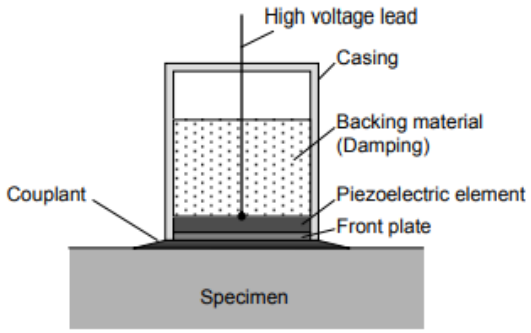

FIGURE 5.4: Typical structure of a piezoelectric transducer (Ihara 2008).

The piezoelectric element is made up of a variety of ceramics such as barium titanate ($BaTiO_3$), lead metaniobate ($PbNb_2O_3$) and lead zirconate titanate (PZT). The active element is polarized material with some parts of the molecules positively charged while the others negatively charged, with two electrodes attached to its opposite faces. The piezoelectric effect occurs when a mechanical force causes the

element to change dimensions, producing an electric field. Compression (pushing forces) and tension (pulling forces) produce a positive and negative current across the element respectively. The element's size and shape are designed for a specific application. The thickness of the element is determined by the desired frequency for transmit mode, since the element vibrates with a wavelength that is twice its thickness (NDT Resource Center 2014). Conventional ultrasonic transducers commonly consist of either a single active element that both generates and receives high frequency sound waves, or two paired elements, one for transmitting and one for receiving. Phased array probes, on the other hand, typically consist of a transducer assembly with 16 to as many as 256 small individual elements. These may be arranged in a strip (linear array), a ring (annular array), a circular matrix (circular array), or a more complex shape. A single element transducer merges the effects of all beam components that strike that area, whereas a phased array transducer can spatially sort the returning wavefront according to the arrival time and amplitude at each element (Olympus Corporation 2017). The ideal shape for a piezoelectric element for a photoacoustic hand-held probe is an annular ring design that can accommodate the fiber optic light source in the center of the ring, such as the one shown in Figure 5.5.

Gao et al. 2013 have shown the importance of picking an appropriate center frequency of the ultrasonic transducer in photoacoustic applications as it relates to image resolution. Higher frequency was shown to be related to the absorber's boundary information, and lower frequency to be associated with the absorber's central information. Hence, the smaller the absorber size, the higher the frequency component. For instance, a centimeter, millimeter and a few hundred micrometer

FIGURE 5.5: Annular pattern of a phased array acoustic transducer element commercially available from Olympus (Olympus Corporation 2017).

absorber generates ultrasonic waves in the $\sim\ 20-300\,kHz$, $\sim\ 70\,kHz-2.5\,MHz$ and $\sim\ 400\,kHz-20\,MHz$ range respectively. This implies that when the center frequency of the ultrasonic transducer is high, the imaging resolution will be higher, and that choosing specifications of an ultrasound transducer depends on the resolution required for the application. Furthermore, choosing an appropriate detector shape is also important. Biqin et al. 2017 have simulated different detector geometries to evaluate their amplitude sensitivity distribution due to an ultrasonic monopole source and as a function of different frequencies emitted by the source (see Fig. 5.6). They have shown that the disk shape has advantages in near-field ultrasound detection because the geometric simplicity minimizes the phase retardation seen with disk elements. Ring shape was also seen to provide better sensitivity at higher frequency, making it more suitable for broadband detection.

Keeping previous photoacoustic literature and the eventual application in mind, commercial and in-house disc and annular- or ring-shaped piezoelectric transducers

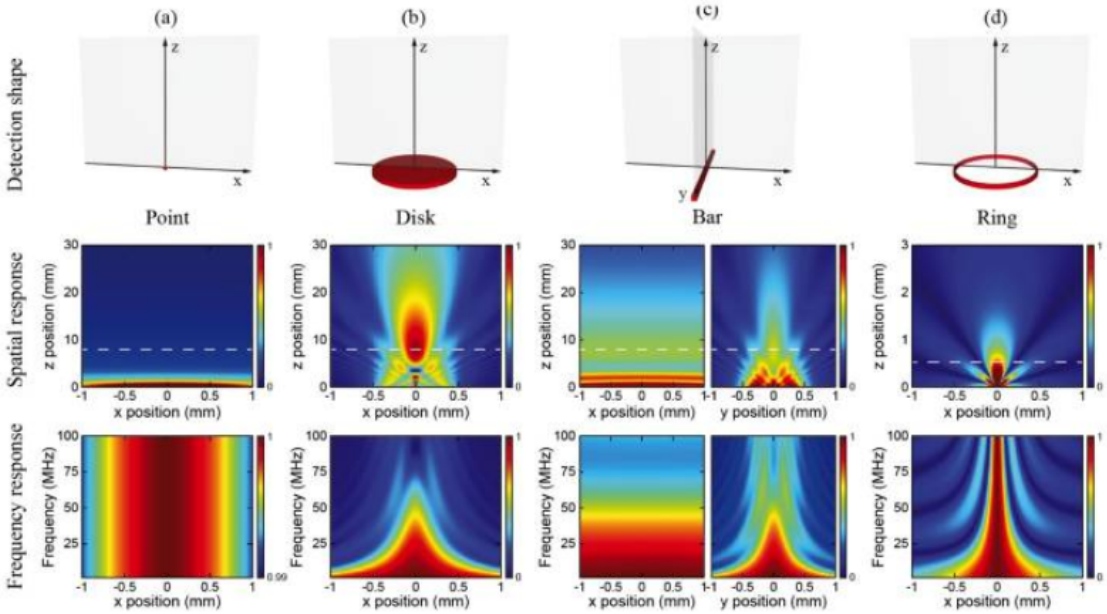

FIGURE 5.6: Simulations performed by Biqin et al. 2017 showing ultrasonic frequency detection sensitivities with four different detection geometries: point shape (a), 1 mm disc shape (b), 1 mm bar shape (c), and 60 μm ring shape (d). Middle panels show the spatial distributions of ultrasonic amplitude detection sensitivities, and bottom panels show spatial distributions of ultrasonic frequency detection sensitivities along dotted locations in the middle panels.

with center frequencies ranging from 1 MHz to 3.5 Hz were chosen for experimentation (Nie et al. 2012; Wang et al. 2008; Petrov et al. 2016).

5.2.1 Disc Immersion Transducers

To initiate experimentation with the photoacoustic effect, two disc-shaped immersion transducers from Olympus Corp. were used (see Table 5.1 and (C) in Fig. 5.7). Immersion transducers are single element longitudinal wave transducers, whose wear face is impedance matched to water for uniform coupling, allowing

optimal capture of the photoacoustic pressure wave by placing the sample containing an absorber in a water bath. This eliminates the need for any coupling gels necessary to impedance match the transducer to the surface of the sample, which would interfere with light propagation as well. Since the transducers were disc shaped, they were operated in orthogonal mode, or in receive mode with a wedge fitted in between the straight fiber optic cable and angled transducer (see Fig. 5.7) so that the transducer and light source are pointed towards the region of the photoacoustic wave initiation.

Table 5.1: Immersion transducer (Olympus Corp.) specifications used for experimentation

Product Code	V314-SU-F1.90IN-PTF	V383-SU-F1.65IN-PTF
Center Frequency (MHz)	1	3.5
Element Diameters (cm)	1.91	0.95
Focal Length (cm)	4.83	4.19

5.2.2 Annular Piezoelectric elements

In addition to using commercial disc transducers, we incorporated annular pieozelectric elements with a center frequency of $3\,MHz$ from Steiner & Martins Inc. in experimentation (see (B) in Fig. 5.8 and Table 5.2). The elements are made of lead zirconate titanate (PZT), and electrodes were soldered onto the positive and ground faces of the elements, and a housing was built around the elements. There were many advantages of using these elements and developing a probe in-house. While Olympus transducers come with a backing attached, and an RF-shielded casing, the PZT elements are significantly less expensive than immersion transducers or any custom made annular transducers from Olympus and the annular design

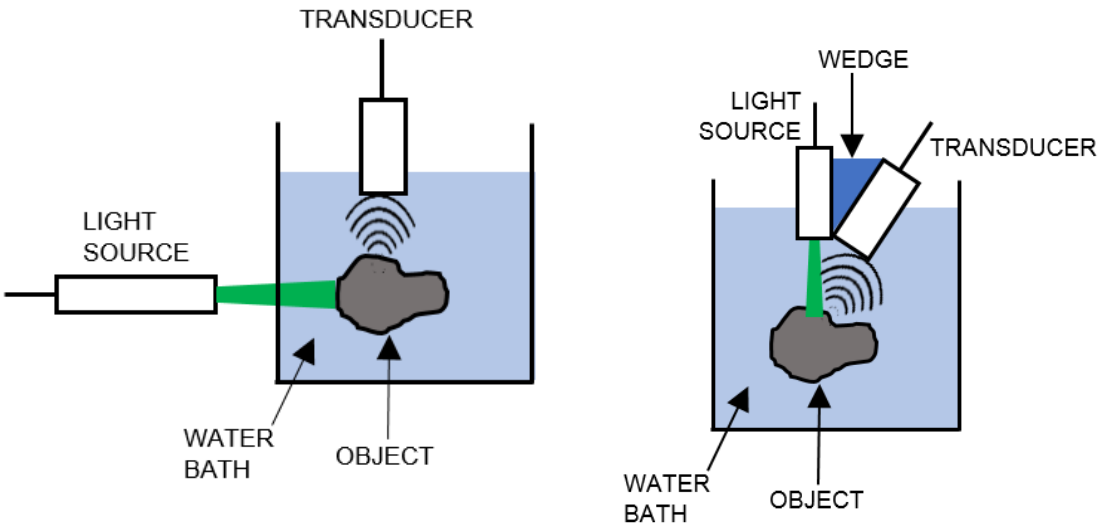

(A) (B)

(C)

FIGURE 5.7: Depiction of orthogonal mode (A), and receive mode (B) of the immersion transducers with the fiber optic cable (light source), with the object being imaged shown submerged in a water tank. (C) showing an immersion transducer from Olympus Inc. with a $1MHz$ center frequency.

allows the threading of a fiber optic cable containing the light source through the middle of the element, thereby allowing for a compact hand-held design to operate the PAI system in receive mode (see (A) Fig. 5.8). Additionally, ultrasonic transducers have directionality, and need to be situated in a manner that optimally directs them towards the acoustic signal. This design reduces the possibility that the transducer may not be oriented correctly for optimal capture of acoustic waves from the illuminated region.

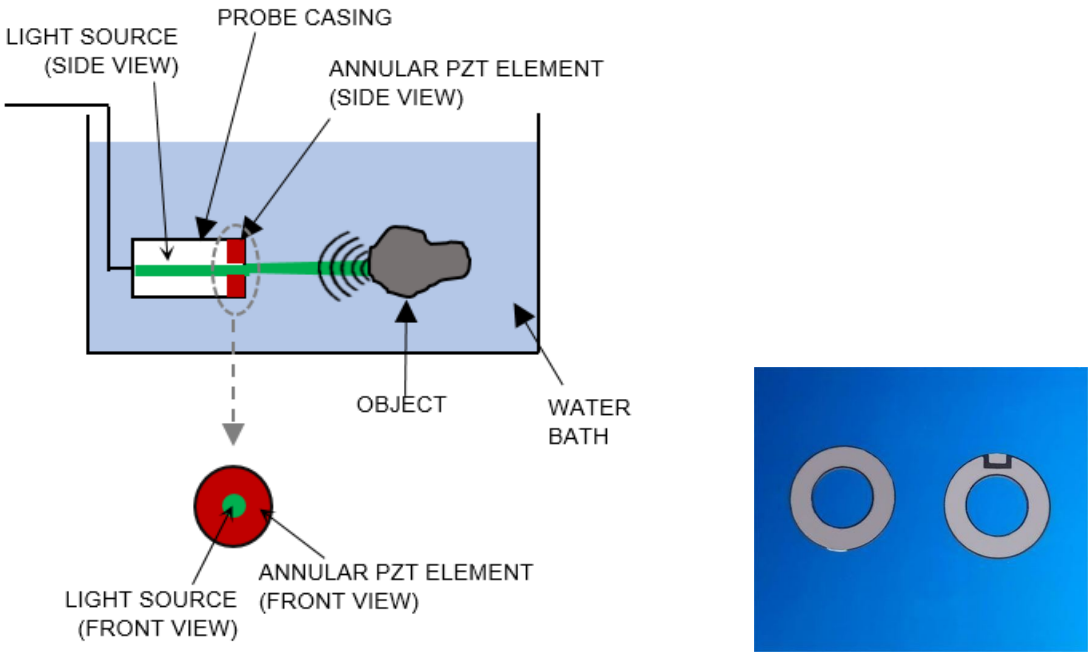

(A) (B)

FIGURE 5.8: Depiction of the side view (top) and front view (bottom) of the annular or ring transducer with the fiber optic cable (light source) threaded concentric to it, with the object being imaged shown submerged in a water tank (A), and the piezoelectric annular or ring element with center frequency of 3 MHz from Martin & Steiner Inc. (B)

5.2.3 Transducer Casing

A casing was designed and 3D printed that could accommodate the fiber optic cable and the PZT element along with all the electrical wiring needed to receive the acoustic signals (see Fig. 5.9). The PZT element was epoxied onto the front of the casing which acts as a backing for the element, and the electrode wires were led through the front into the casing, and attached to a BNC cable that connects the element to an instrumentation pre-amplifier. The fiber optic cable containing the 532 nm laser light is threaded through the back of the probe and into the front

Table 5.2: Annular or ring transducer (Steiner & Martin Inc.) specifications used for experimentation.

Product Code	SMR1585T07111R
Center Frequency (MHz)	3
Outer Diameter (cm)	1.5
Inner Diameter (cm)	0.85
Thickness (cm)	0.07
Resonant Mode	Thickness mode Vibration

of the casing.

(A) (B)

Figure 5.9: Front view (A) and side view (B) of a PZT element in 3D printed casing built in-house.

5.3 Ultrasonic Pre-amplifiers

Photoacoustic signals are low amplitude, hence a pre-amplifier is usually required to measure signals. Pre-amplifiers also contain RF bandpass filtering that helps limit very high frequency noise. An ultrasonic pre-amplifier from Olympus Corp. was used (Model 5682) that provides amplification of signals ranging from $0.5 -$

$25\,MHz$, with a gain of $30\,dB$ at $10\,MHz$, with an output limited to $2.5\,V$ peak-to-peak. A second, low noise pre-amplifier was also used based on the Exar Com-Linear CLC1002 Ultra Low-Noise amplifier, whose gain was higher.

5.4 Data Acquisition Card

The pre-amplifier output is connected to a data acquisition card from National Instruments Corp. (NI 5102) that has two 8-bit resolution analog input channels, and a sampling rate of 20 *MegaSamples* per *second*. The card also contains an external trigger, where output from the photodiode enables the card to initiate collecting acoustic signals. Acoustic signals are collected for $100\,\mu s$ after the trigger. Assuming a speed of sound of $1500\,m/s$, as is the case in soft tissue and water, this allows collection of photoacoustic signals that are originating from objects up to $0.15\,m$ away, which encompasses the entire water tank that the object is placed in, and a $50\,ns$ interval between the 2000 sampled points. Output from the card can be viewed through the NI SCOPE program on the computer, or it can be stored in MATLAB to be processed at a later time.

5.5 Linear Translation Stages

In order to perform PA imaging, the object being imaged must be illuminated at different spatial locations. This is done through the use of a PC-controlled X-Y translation stage. Two motorized linear translation stages were used to hold the

photoacoustic probe and move it in discrete 0.25 mm steps in the rasterized pattern shown in Figure 5.10. The stages allowed controlled, precise and repeatable motion of the probe for the experiments. Stepper motors that convert rotary motion into linear motion after being given an electrical impulse were used to drive the two stages. After each step, the stage was paused long enough for $n = 10$ photoacoustic signals to be collected and saved into MATLAB. $n = 10$ was picked after giving consideration to the time taken per acquisition and the number of averages that would sufficiently reduce noise.

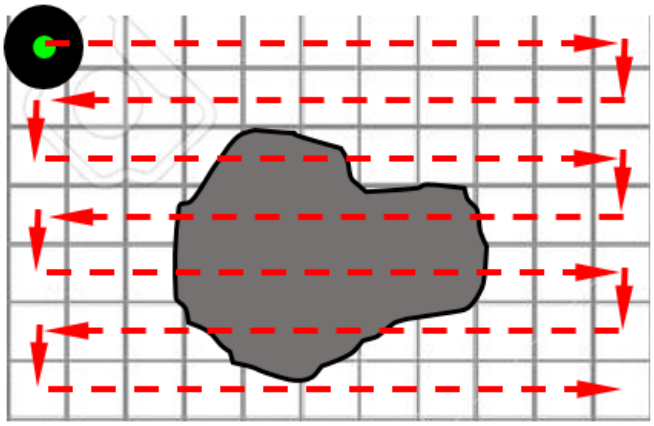

FIGURE 5.10: Top view of the raster pattern used to acquire images; annular ultrasonic transducer concentric with light source shown on the top-left of the depiction, and object being imaged shown in gray. Each box in the background grid map represents the area over which the transducer pauses and collects 10 signals, and the area which corresponds to 1 pixel in the final photoacoustic image

5.6 Data Processing

At each (x,y) sample location, the 10 signals constituting one pixel were processed with the following steps:

1. the mean of each photoacoustic waveform was subtracted from all the data points making up the waveform to bring each signal to zero baseline (see Fig. 5.14 and Fig. 5.15),

2. the 10 waveforms collected after each step (at each pixel) were averaged together to reduce noise in the dataset (see Fig. 5.16),

3. the averaged waveform was absolute valued, such that all negative lobes of the signal were reflected onto the positive axis,

4. the resulting waveform was summed over a user-selectable finite time window (time-gated), and the value was stored in an element of the 2D array in the corresponding pixel address representing the $0.25\,mm \times 0.25\,mm$ area over which the transducer paused and collected the 10 signals

To clarify, consider imaging a black resin point source embedded in gelatin that is molded into a petri dish and suspended in a water bath, with a photoacoustic imaging system from the top (see Fig. 5.11). Black resin was experimentally determined to be an optimal absorber and is expected to create a photoacoustic signal that can be detected by the developed system.

Next, consider the transducer pausing to collect 10 photoacoustic signals over the shaded yellow area in Figure 5.11. The 10 signals are expected to look similar

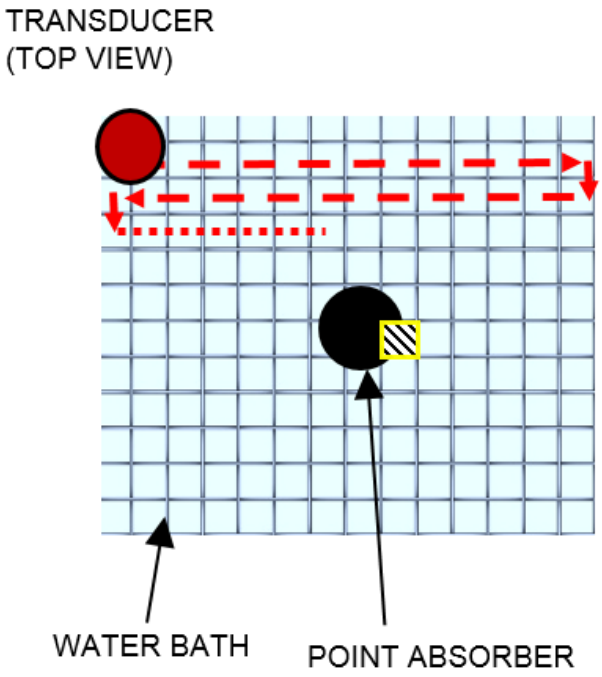

FIGURE 5.11: Top-view depiction of experimental setup showing transducer (top-left), raster pattern (red dotted lines) and absorber in a water bath. Gelatin and petri dish surrounding the point absorber not shown. Each box in the background grid map represents the area over which the transducer pauses and collects 10 signals. Yellow shaded box represents the area whose data will be analyzed in this example.

to the ones shown in Figure 5.12. The high-amplitude photoacoustic signal due to the point absorber can be seen between $\sim 4-6\,\mu s$ in all 10 signals in Figure 5.12, and more closely in Figure 5.13. As outlined in Step 1 of the data processing method, all 10 signals are first baseline corrected as shown in Figure 5.14, and more closely in Figure 5.15. Next, as mentioned in Step 2, the 10 zero baseline waveforms are averaged together to produce the waveform in Figure 5.16, and in Step 3, the absolute value of the averaged waveform produces the waveform shown in Figure 5.17. Next, as in Step 4 and Figure 5.18, a subsection consisting of data from $\sim 4-6\,\mu s$ of this waveform is taken and summed to produce a value of

$2.188\,V$. This value, as seen in Figure 5.19 is fed into a 2D array element or pixel corresponding to the shaded yellow area in Figure 5.11.

These 2D arrays are then shown in future chapters as colored images, where the red color represents higher PA values, and blue represents lower values (see Fig. 5.19). While displaying some images, time-gating is used where only a finite time interval from the time-dependent photoacoustic signal is used rather than the entire $100\,\mu s$-long signal, in order to reject acoustic data from unwanted depths in the phantom. Additionally, in planar imaging, time-gating can be used to discern depth information of the photoacoustic wave producing objects. If the depth of these objects is known in designed phantoms, time-gating can be used to strategically remove photoacoustic signals originating from objects not being analyzed in the experiment. The time interval constituting the images will be clearly displayed, and the hypothesized reasons behind the appearance of unwanted signals in the dataset will be discussed in Chapter 6.

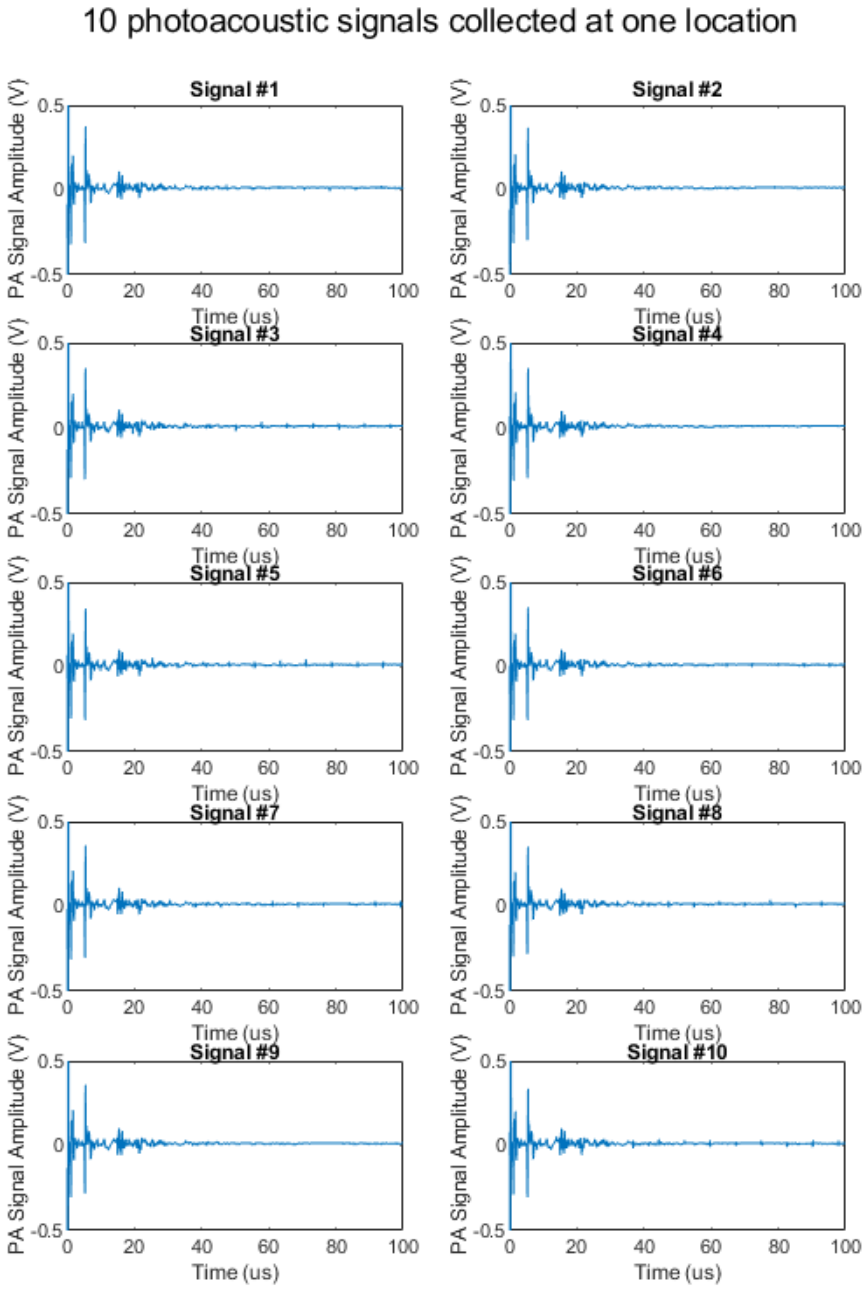

Figure 5.12: 10 photoacoustic signals collected over the yellow shaded area shown in Figure 5.11

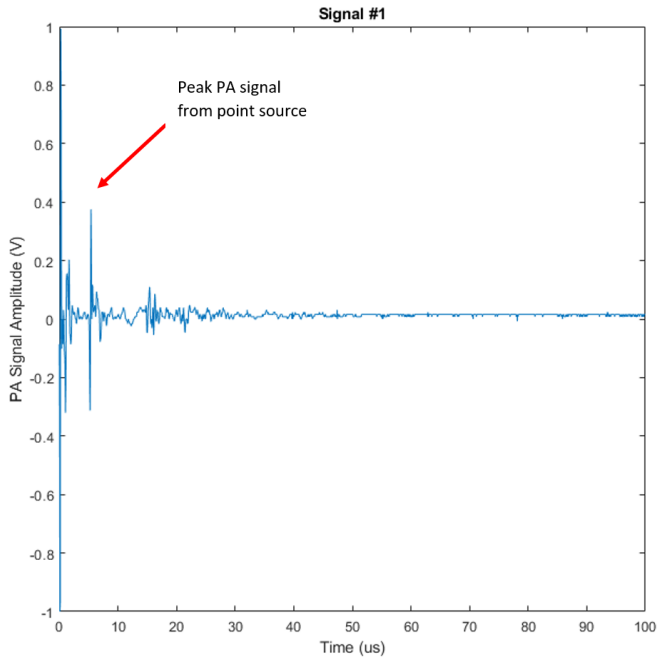

FIGURE 5.13: PA Signal 1 from Figure 5.12

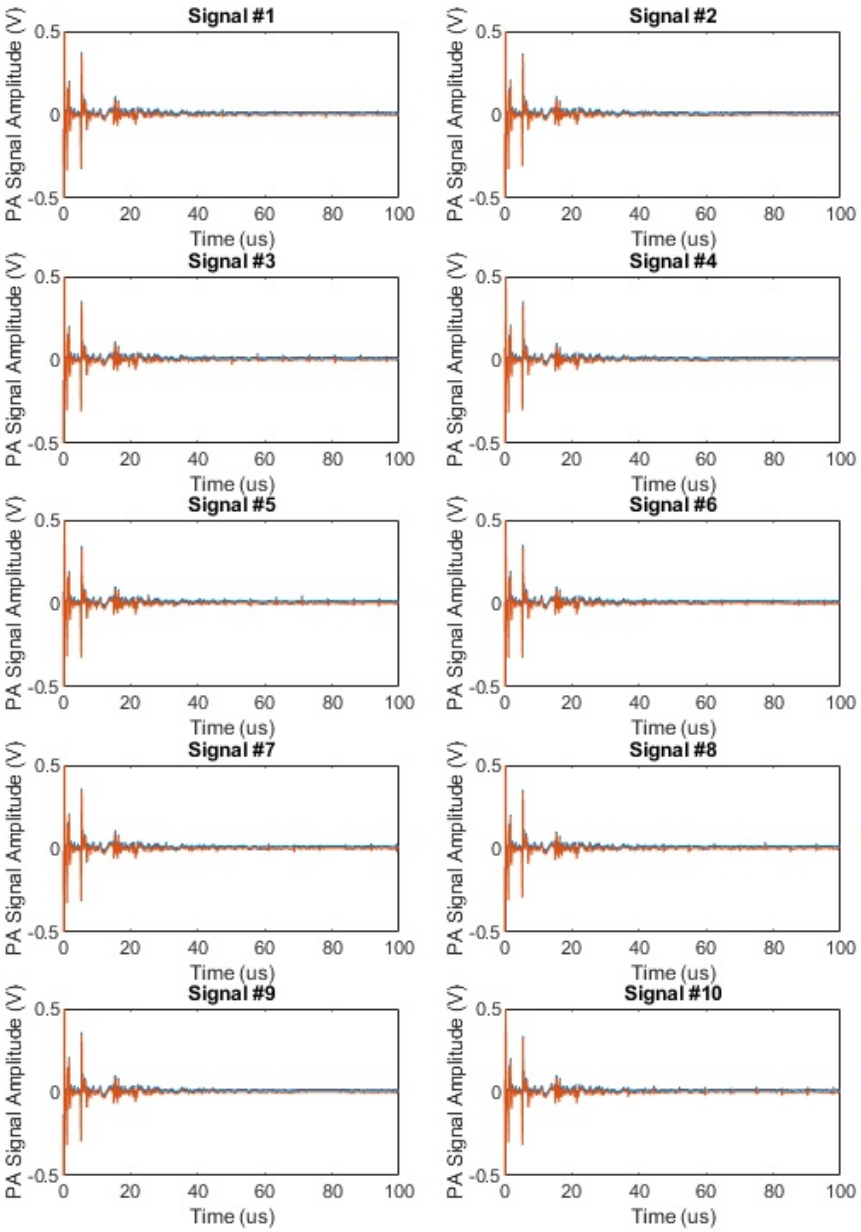

FIGURE 5.14: STEP 1: 10 photoacoustic signals collected over the yellow shaded area shown in Figure 5.11, and brought down to zero baseline

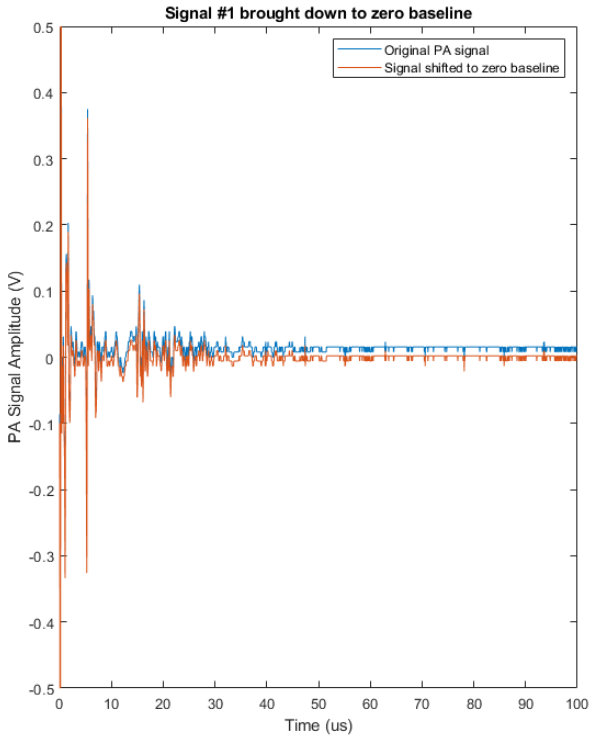

Figure 5.15: STEP 1: Closer view of zero baseline and raw photoacoustic Signal 1 from Figure 5.14

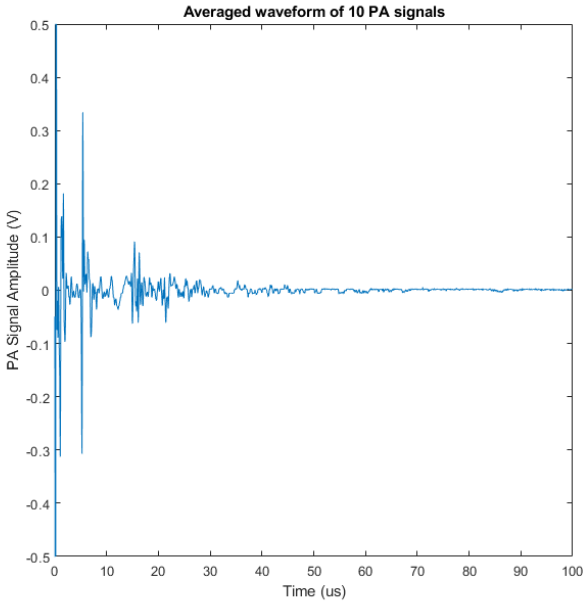

FIGURE 5.16: STEP 2: Zero baseline photoacoustic signals from Figure 5.14 averaged to produce one waveform

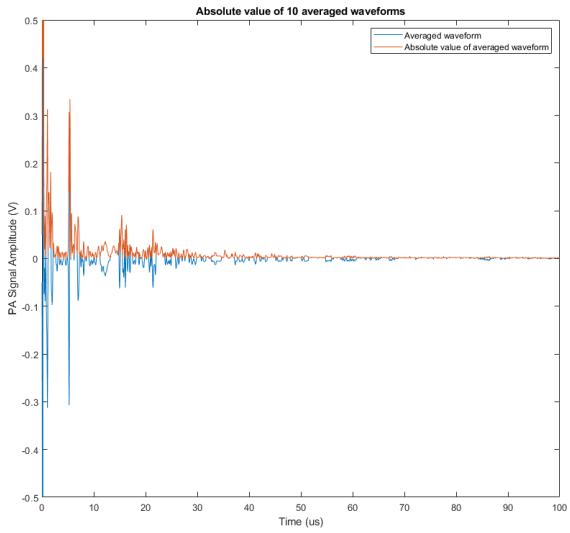

FIGURE 5.17: STEP 3: Absolute value of dataset from the averaged waveform from Figure 5.16

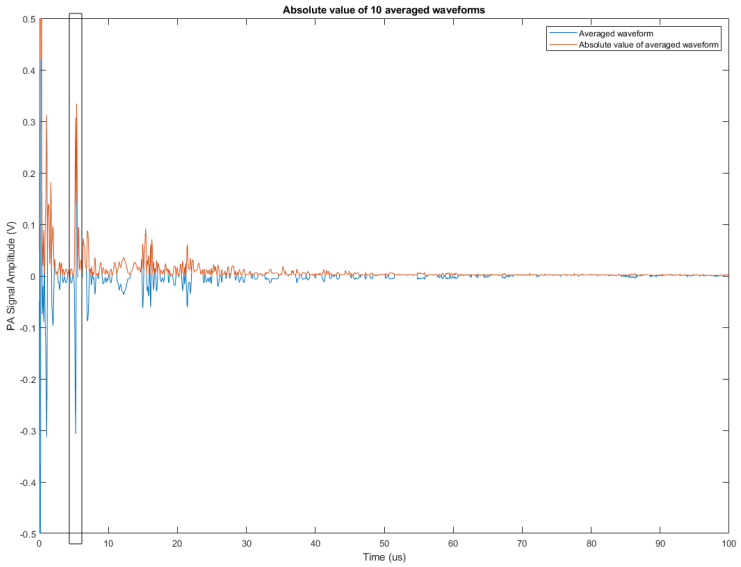

FIGURE 5.18: STEP 4: Time-gated subsection of averaged waveform from 5.17 that forms the value in Figure 5.19 (black pixel shown)

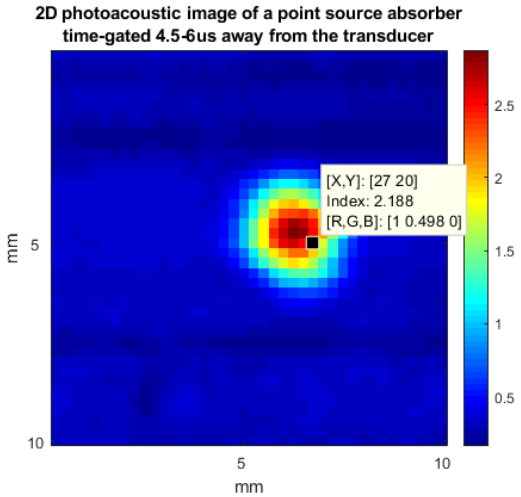

FIGURE 5.19: Data of one pixel showing the summed time-gated subsection from Figure 5.18 within the final 2D image produced as a result of summing time-gated subsections of processed signals from all areas depicted in Figure 5.11.

Chapter 6

Experimental Results

After hardware and software implementation, the PA system was tested using various photoacoustic source geometries. In medical imaging, phantoms are imaging specimens that have known geometric and material composition and are used in the development and characterization of an imaging system or imaging techniques. Furthermore, a tissue-mimicking phantom emulates important properties of biological tissue to provide a clinically relevant imaging environment. In the case of PA imaging, optical absorption and scattering are the two most important parameters in phantoms, since the magnitude of a photoacoustic signal is related to both the local fluence and optical absorption at the signal-generating source. Phantoms with gel-based backgrounds are often used for PA imaging as they allow for suspension of absorption- or scatter-inducing objects, and they can be immersed in a water bath without degrading quickly, which is required for optimal coupling of photoacoustic signals. While gel-based phantoms do not have a long shelf-life, they can be formulated quickly and with ease. To increase absorption, colored dyes are commonly used, and to increase scattering, Intralipid solution or polystyrene

beads are frequently (Cook et al. 2011a).

6.1 Gel-based Phantoms

Phantoms were prepared by combining 225-bloom gelatin derived from porcine skin (Knox Unflavored Gelatine) with water, according to instructions provided by the manufacturer. The water was brought up to boiling point, then combined slowly with gelatin powder while mixing continuously to mitigate aggregation. After a homogeneous mixture was produced, the mixture was poured into a mold or a container containing a photoacoustic wave producing source. Most phantoms were poured into petri dishes. The phantoms were cooled at 4 degrees Celsius for $20\,min$ up to $1\,hr$, depending on their sizes. The final phantoms produced were translucent, with a yellowish hue. A 3D printed stand for the petri dishes was built and epoxied onto the bottom of a water bath container, so that the petri dishes could be suspended in the water bath reducing any chance of mobility while imaging.

Absorption-inducing agents used in experimentation include concentrated India Ink incorporated into gelatin, and black photoreactive cured or 3D printed resin. India Ink has been shown to be a good absorber of $532\,nm$ light (Cook et al. 2011b). Alternatively, the black resin is traditionally used for 3D printing objects with Formlabs 3D Printers. It is described as a mixture of methacrylic acid esters, photoinitiators, proprietary pigment and additive package in its safety data sheet, hence the exact formulation is unknown. Through experimentation, it was found that the 3D printed resin absorbs $532\,nm$ light very well and produces

a significant PA signal. It is much easier to handle and work with, as there is no need to incorporate it into gelatin, or contain it in capillary tubes which add more complexity to the photoacoustic signal. Additionally, virtually any source geometry can be printed to test the system's response.

6.2 Point Source

In order to test the imaging capabilities of the experimental PA probe, an absorption-inducing point source experiment was used. First, the immersion disc transducer with center frequency of 3.5 MHz (Olympus Corp. Model V383-SU-F1.65IN-PTF) connected to the Olympus pre-amplifier were used to ensure that a point source could be localized reliably, and that the expected characteristic N-shaped photoacoustic waveform can be detected with our apparatus (see Fig. 3.1). Second, the response to a point source of two different setups of the PA system were compared with this experiment. One setup was the 3.5 MHz immersion disc transducer connected to the Olympus pre-amplifier, which will be referred to as the "commercial setup". Another setup was an annular or ring transducer with center frequency of 3 MHz (Steiner & Martins Inc. with in-house casing) connected to the CLK-10002 pre-amplifier, which will be referred to as the "in-house setup". Third, this experiment was used to compare spatial distribution of ultrasonic amplitude detection sensitivities of the two setups.

6.2.1 Absorber

The first set of experiments were performed to ensure that a photoacoustic wave producing source could be localized by the imaging system accurately, and to understand the impulse response of the imaging system to a point source. To approximate a point source, a small cylinder of black resin material was embedded in gelatin and set in a petri dish. The cylinder was `1 mm` in height, and `1 mm` in diameter (see (A), (B) and (C) in Fig. 6.1). The petri dish was submerged in a water bath. The diameter of the circular light source reaching the phantom from the fiber optic was $\sim 1\,cm$, making it $\sim 10X$ larger than the absorber.

6.2.2 Point Source Response

To meet the first two objectives, the commercial and in-house setups were positioned across from each other in a water bath, with the phantom containing the absorber situated in between them (see (D) in Fig. 6.1). Here, receive-mode refers to the configuration where the transducer and light source are on the same side of the absorber. Transmit-mode refers to the configuration where the transducer and light source are on opposite sides of the absorber. In this experiment, the fiber optic cable containing the light source was positioned within the in-house setup, such that the in-house setup was operating in receive mode, and the commercial setup in transmission mode. Both transducers were situated $0.75\,cm$ away from the absorber. Both setups were moved across the petri dish, meaning the in-house setup containing the light source was also moved, such that the light was always central to both transducers as they both move to create two 2D planar images.

(A) (B) (C)

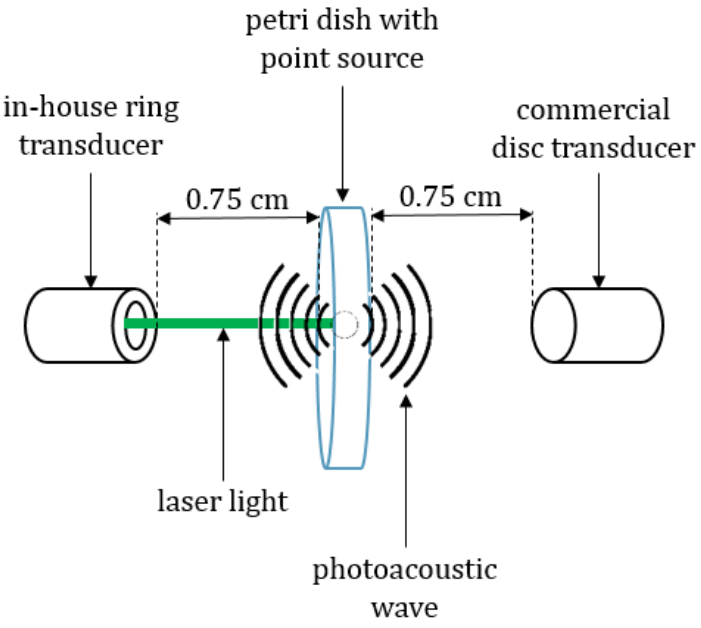

(D)

FIGURE 6.1: Height (A) and Diameter (B) of absorption-inducing point source embedded in gelatin (C); (D) depiction of experimental setup showing commercial (transmission mode operation) and in-house (receive mode operation) setups situated equidistantly at 0.75 *cm* away from the point source absorber contained in the petri dish.

The photoacoustic signal obtained from the commercial setup as a result of the point source experiencing thermoelastic expansion is shown in (B), while the background signal is shown in (C) of Figure 6.2. The former signal (B) shows the characteristic N-shaped acoustic waveform that results from a point or spherical absorber due to the photoacoustic effect, while the latter signal (C) demonstrates the signals originating from a location that does not contain the absorber. This implies that (C) of Figure 6.2 is showing the relatively low-amplitude signals originating due to thermoelastic expansion being caused in the petri dish glass, the gelatin formulation and any impurities within it, any extra materials in the water bath (the in-house transducer and associated wiring in this case), and any impurities within the water bath as the light source illuminates all these objects within its field. Since minimal light is absorbed, or reaches these objects, the photoacoustic signals captures are also low-amplitude, but real. All photoacoustic waveforms displayed were obtained by following the method outlined in Section 5.6 up to Step 3., meaning the signals are averaged waveforms ($n = 10$) acquired from the pixel locations shown in the figures. Taking a closer look at (B), it should be noted that the N-shaped wave is seen with opposite polarity. This is due to the Olympus immersion transducers that reverse or invert the phase or polarity of the echo from the boundary between the materials when the order of relative acoustic impedances is reversed (low to high versus high to low).

To compare the commercial and in-house setups, the final photoacoustic images from both setups can be analyzed. (A) in Figure 6.2 and (A) in Figure 6.3 show the images produced by the commercial setup and the in-house setup respectively. Both images have been time-gated similarly to show summed signals

from $0.675 - 0.9\,cm$ away from the transducers. The images were time-gated to remove any potential photoacoustic signals generated from objects immediately close to the transducers, such as the casings of the transducers. Photoacoustic signals greater than $0.9\,cm$ from the transducer were removed to eliminate acoustic signals originating from the transducer and associated wiring situated opposite to the transducer's signals being examined. Flipping the commercial transducer image, the weighted centroid is calculated for the commercial setup. As can be seen in (A) and (B) of Figure 6.4, the calculated weighted centroids appear to be the same for both images, located at: [4 4.75] cm. This calculation ensures that the setups were aligned appropriately across from each other, and focused similarly towards the point absorber so that they can be compared reliably.

The petri dish was also flipped and similar results were obtained from both setups. This was done to ensure that the contribution of uneven gelatin layers and the petri dish glass are minimal to the overall photoacoustic signal for both transducers.

6.2.3 Amplitude Detection Sensitivities

All ultrasonic waves diverge and have beam spread, including the photoacoustic wave produced by objects in this experiment. Depending on the shape and size of the ultrasonic detector, the spatial amplitude divergence of an ultrasonic signal will be captured with different spatial sensitivities, as discussed previously in Section 5.2. To understand the spatial sensitivity of the detectors used in these

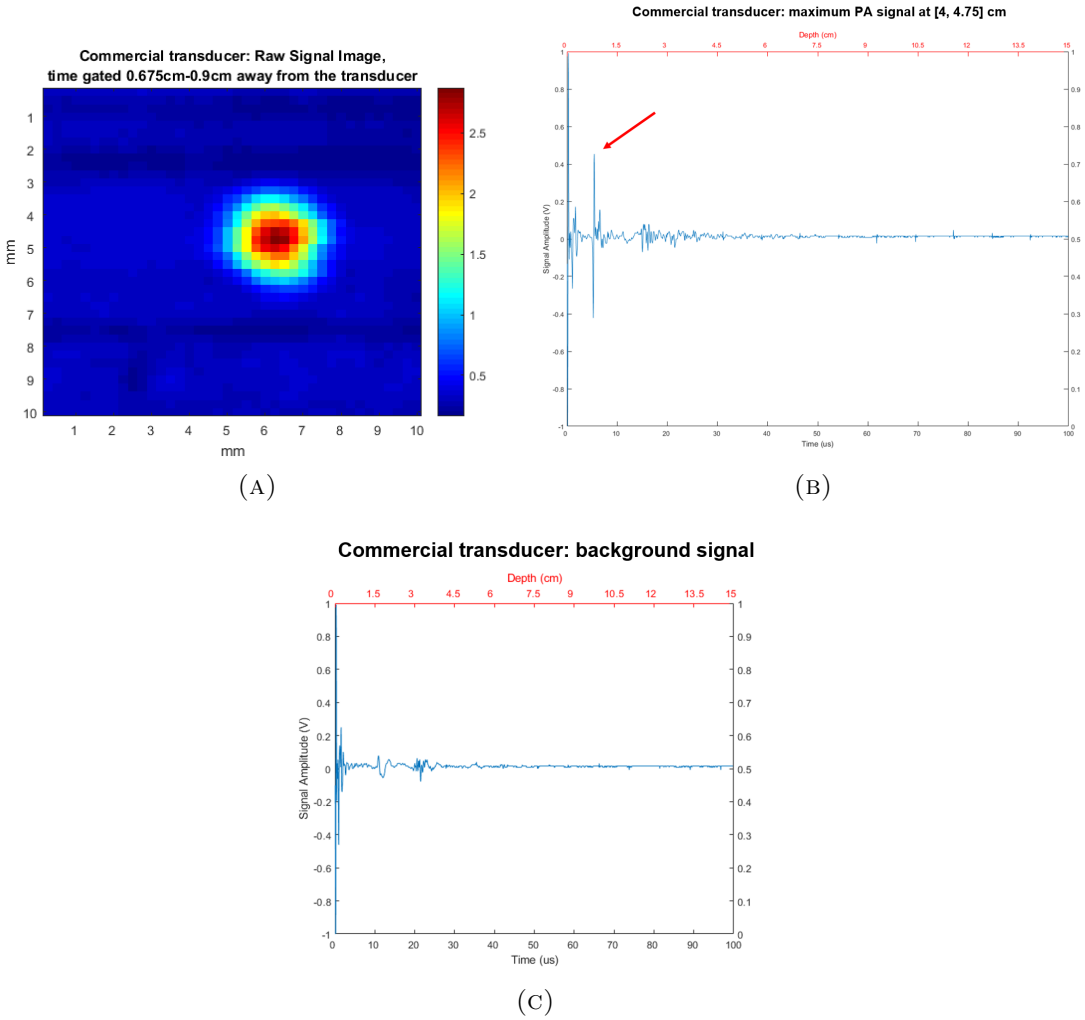

FIGURE 6.2: Summed photoacoustic image time-gated to include signals from $0.675-0.9\,cm$ away from the transducers (A), averaged waveform of 10 signals obtained from a location containing the point absorber (B), and averaged waveform of 10 signals obtained from a location without the point absorber (C) captured through the commercial setup.

experiments, the setup depicted in Figure 6.5 was used with the point source absorber. Unlike the previous experimental setup, the light source was in a constant position in this experiment, always illuminating the point absorber such that a photoacoustic wave due to the absorber was produced throughout the experiment.

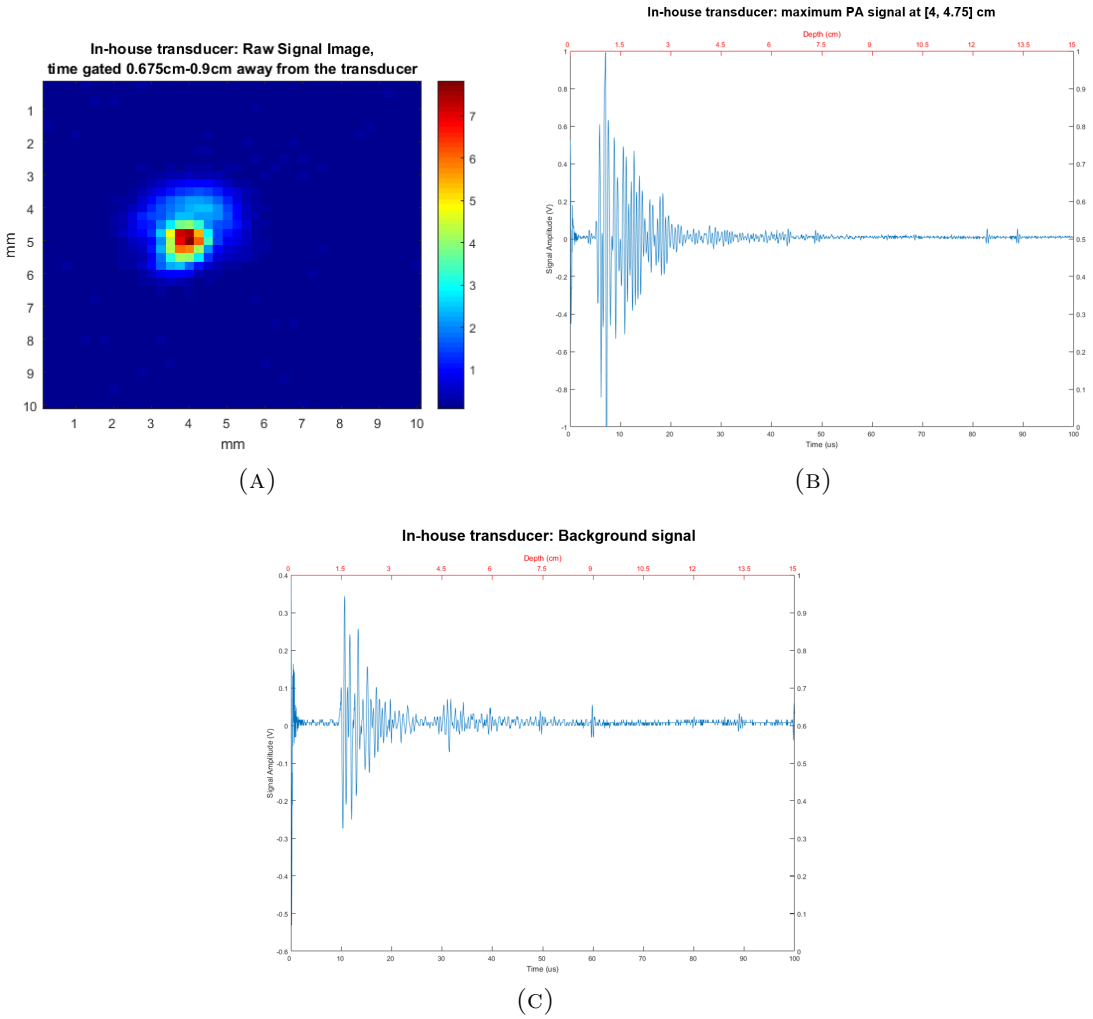

FIGURE 6.3: Summed photoacoustic image time-gated to include signals from $0.675-0.9\,cm$ away from the transducers (A), averaged waveform of 10 signals obtained from a location containing the point absorber (B), and averaged waveform of 10 signals obtained from a location without the point absorber (C) captured through the in-house setup.

The transducers were translated spatially away from the acoustic source through the raster pattern depicted in Figure 6.5. The commercial setup produced the amplitude sensitivity pattern shown in Figure 6.6, while the in-house setup produced the pattern shown in (A) of Figure 6.7. As seen in Figure 5.6 discussed

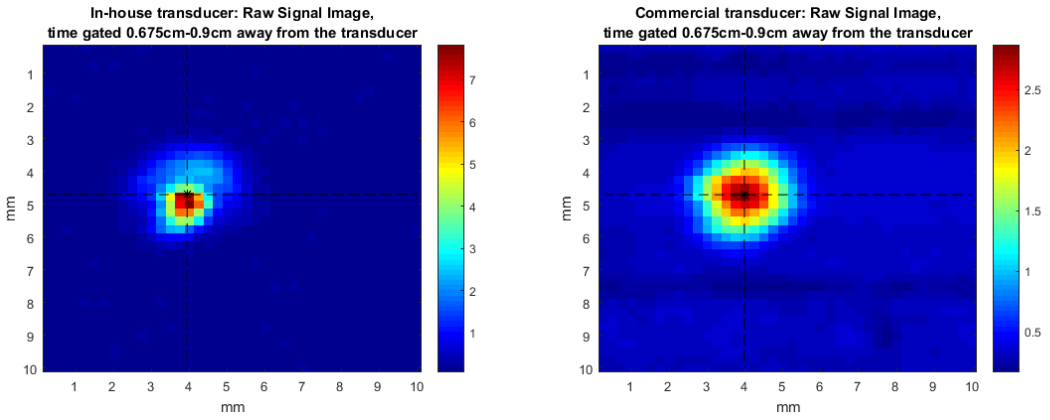

(A) (B)

FIGURE 6.4: Summed photoacoustic images captured through the in-house setup (A), and commercial setup (B) showing the location of their centroids with dotted black lines, time-gated to include signals from $0.675 - 0.9\,cm$ away from the transducers.

in Section 5.2 through the research of Biqin et al. 2017, the ring transducer has advantages (greater sensitivity to acoustic signals) in near-field spatial detection of ultrasound, while the disc transducer has advantages in far spatial fields. The images acquired do not entirely resemble the simulated ones in Figure 5.6 since the initial photoacoustic signals that would have been closest spatially to the absorber were not acquired. This is because the point absorber was embedded underneath some layers of gelatin, and because close contact with the phantom as the transducer is translated linearly would have moved and degraded the phantom surface, which may have presented further problems with localization and accuracy of the photoacoustic signals detected.

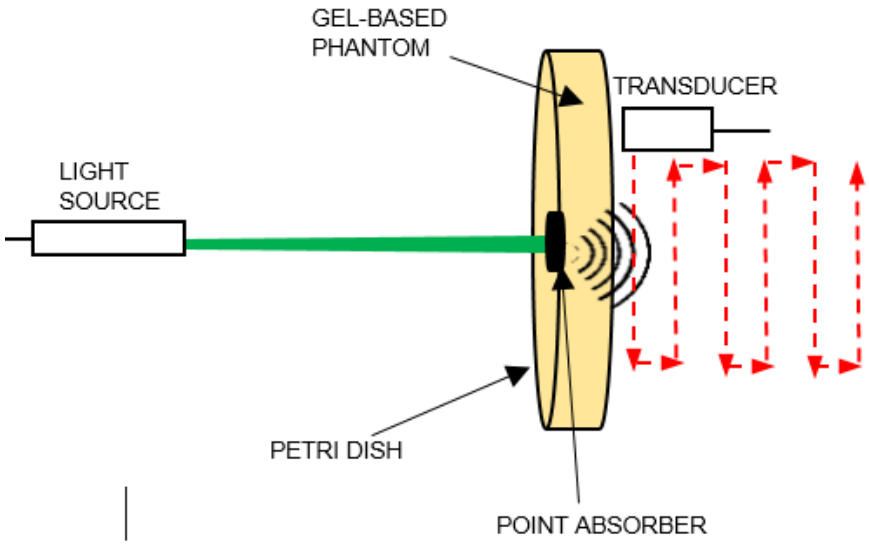

Figure 6.5: Depiction of experimental setup used to capture ultrasonic amplitude spatial detection sensitivities of both commercial and in-house setups; raster pattern shown in red dotted lines moving across (up and down) and away from the point absorber.

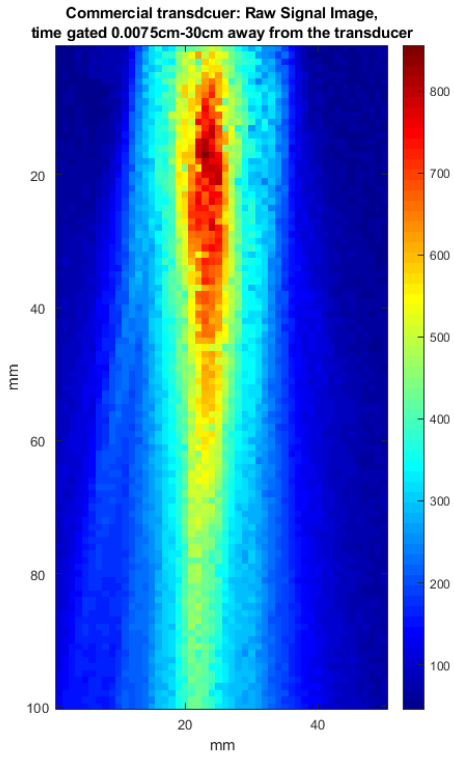

FIGURE 6.6: Spatial detection sensitivity pattern of the commercial setup containing the disc immersion transducer with $3.5\,MHz$ center frequency.

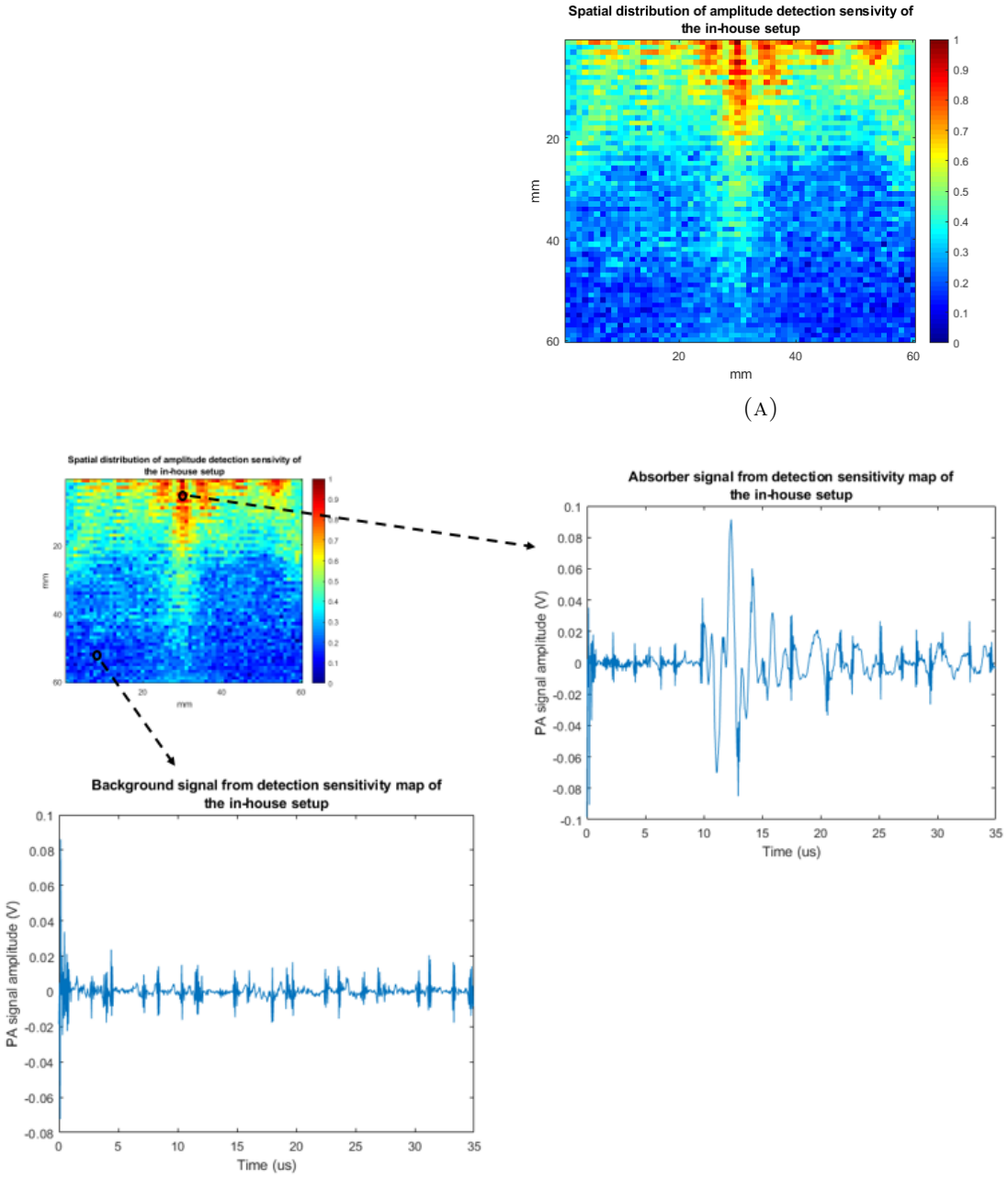

(A)

(B)

FIGURE 6.7: Spatial detection sensitivity pattern of the in-house setup containing the annular or ring immersion transducer with $3\,MHz$ center frequency (A), and acoustic signals (n=1) making up spatial sensitivity pattern and background signals (B). Note the background acoustic signal shows noise.

6.3 Line Source

Following confirmation that both acquisition systems could detect an expectant PA signal from a point source, an absorption-inducing line source was used to demonstrate that a line-source that is experimentally possible could be imaged. Some errors that have often interfered with optimal image formation or transport of photoacoustic signals in these experiments have been identified.

6.3.1 Absorber

The line absorber was a $13\,mm$ long and $1\,mm$ wide line 3D printed with black resin material. Similar to the point source, the line source was also embedded in gelatin in a petri dish (see Fig. 6.8). The diameter of the circular light source reaching the phantom from the fiber optic was $\sim 1\,cm$, making it $\sim 10X$ larger in diameter than the absorber.

6.3.2 Errors

Figure 6.9 shows the summed photoacoustic image captured through the in-house setup. The first unintended effect demonstrated in the image is an apparent "doubling" of the line absorber. As discussed previously in Section 5.1.1, this effect can be attributed to laser light being incorrectly guided into the cladding instead of the core of the fiber optic cable, resulting in a donut beam profile exiting the fiber

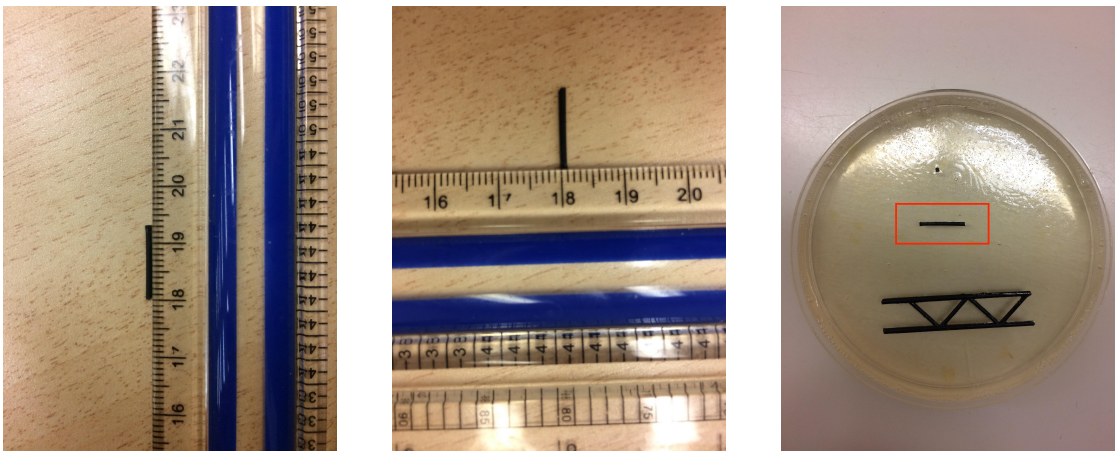

(A) (B) (C)

FIGURE 6.8: Length (A), Diameter (B) and absorption-inducing line source embedded in gelatin (C).

optic and reaching the absorber. In future discussions, we show the simulation results of a donut beam profile and homogeneous absorber in MATLAB, confirming this scenario (see (C) in Figure 6.12). The results show a reduction in the center of the convolved signal, which is seen in this experiment, and interpreted as the "doubling" effect. In the image produced, the width of line-source is observed to be 2.5 mm, compared to the actual width of 1 mm.

Another error seen is the non-homogeneity of the signal, seen as a break in the expected homogeneous line-source in Figure 6.9. One explanation may be that the break is seen due to impurities such as denatured protein and fat aggregates in gelatin blocking the penetration of light that reaches the line-absorber. The aggregates are formed when gelatinous solutions are heated and can be minimized by not overheating the solution.

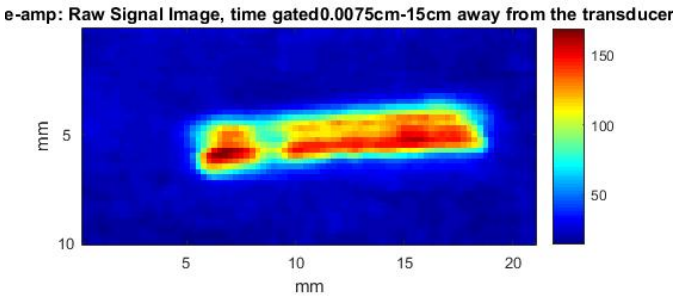

FIGURE 6.9: Summed photoacoustic image captured through the in-house setup of phantom containing the line source absorber.

6.4 Image reconstruction of a geometrically complex absorber

Next, we wanted to characterize the response of the photoacoustic system to a geometrically complex absorber. The phantom was a `4.3 cm` by `1 cm` scaffold made with black resin, and embedded in gelatin (see Fig. 6.10). All widths of line absorbers forming the scaffold were `1 mm`.

Figure 6.11 shows the PA image formed by summation of RF signals obtained at each pixel of the complex source phantom from the in-house transducer and pre-amplifier setup. This data set was used to measure other performance characteristics of the in-house setup. First, mean and summed signals from the cross-section of the top and bottom absorbing lines were plotted to assess the distribution of the signal strength (see Fig. 6.12 (A)). The analysis indicated a FWHM of `2.25 mm` for both lines. Simulating the convolution of a rectangular pulse of width

`1 mm` and a Gaussian light source with $\sigma = 0.89\,mm$ to $\sigma = 0.97\,mm$ produced $FWHM = 2.2\,mm$ of the convolution result, allowing us to predict the width of our light source as it reaches the absorber (see Fig. 6.12 (B)). Also seen in Figure 6.12 (A) for the top line is a reduction in signal at the top of the curve. This can be explained by inefficient alignment of the laser beam to the fiber-optic, creating a well-established donut-shaped laser beam at the output of the fiber optic. This is also simulated in Figure 6.12 (C), and convolved with the rectangular absorber to produce the results seen experimentally.

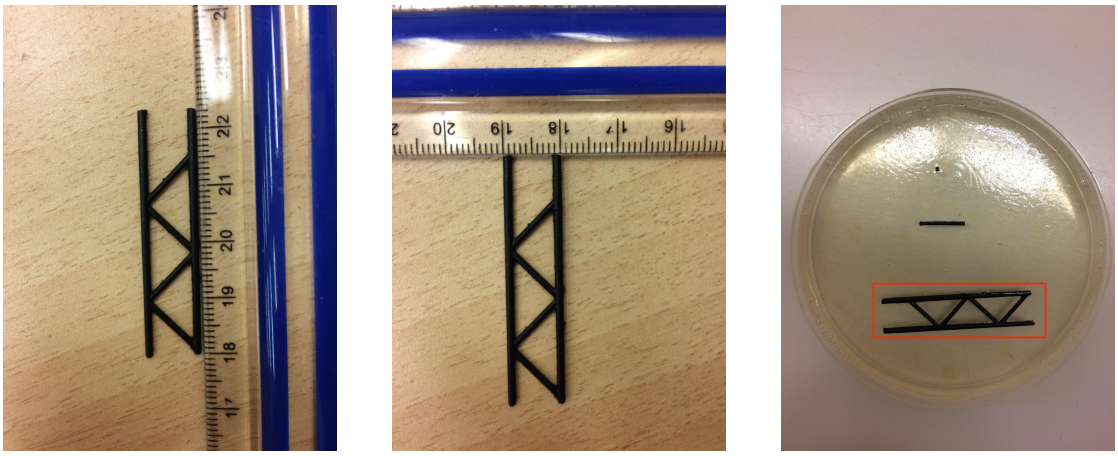

(A) (B) (C)

FIGURE 6.10: Height (A), Width (B) and final geometrically-complex source embedded in gelatin (C)

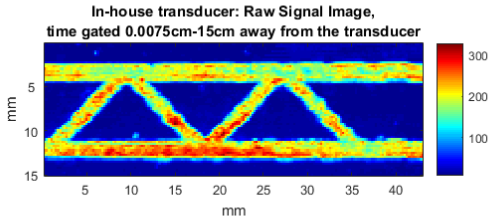

Figure 6.11: PA image of complex source embedded in gelatin formed from in-house setup

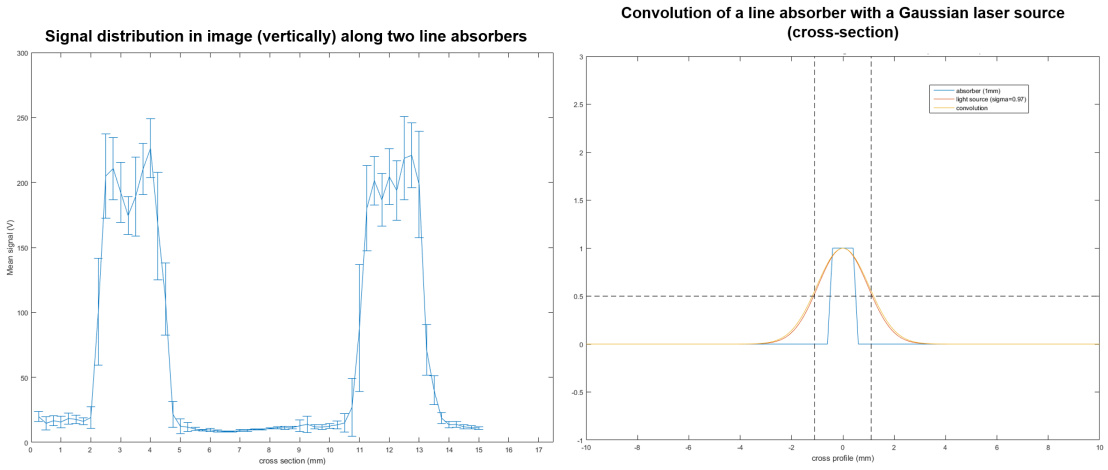

(A) (B)

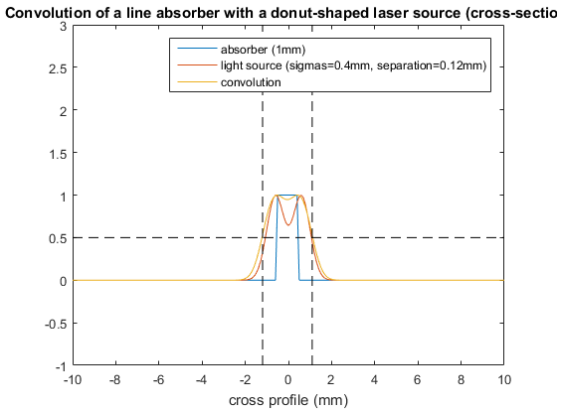

(C)

Figure 6.12: Mean RF signals of top- and bottom-lines of the geometrically-complex absorber (A), simulated convolution result of a line absorber with a gaussian light source (B) and simulated convolution result of a line absorber with a donut-shaped light source (C)

6.5 Effects of optical scattering on photoacoustic signal

Up to now, experiments were performed using water as a transmission medium. Water is a low optical scattering medium that allows us to measure the effect of the PA absorber and US wave. In order to understand how optical scattering can influence the experimental photoacoustic signal, varying quantities of milk was added to a geometrically complex phantom (see Fig. 6.13). The phantom and transducer positions were kept constant as milk concentration was increased in the surrounding water bath. 2% milk was used, meaning 2% of the milk volume used was milk-fat or cream. This 2% milk was further diluted with water.

Figure 6.14 (A) to (E) show resulting PA images as 2% milk's concentration is increased from 0% to 5%, or as fat concentration is increased from 0% to 0.1% of the total volume. PA images show the sequential degradation of the geometrically-complex structure. The experiment was initiated by submerging the petri-dish containing the absorber in a $3\,L$ water bath with no milk. Figure 6.14 (A) shows the results of this initial experiment, acting as a baseline for visual comparison. As milk was added slowly to the water bath, real-time degradation of PA signal was observed. Upon acquiring data and forming the images, three effects were observed. First, strength of PA signal decreased as fat concentration increased. Second, by 0.05% fat concentration in the surrounding medium, high-intensity PA signals started appearing outside of the expected regions containing the PA absorber (see (D) in Fig. 6.14). Third, a "doubling" effect that has been expanded upon in Sections 5.1.1, 6.3.1 and 6.4 was observed. Degradation of PA signal is

expected as any material more absorbing than water is added in the surrounding medium. The second effect can be explained by scattering, as molecules of fat redirect the trajectory of photons in the laser beam and the resulting PA signals are distorted.

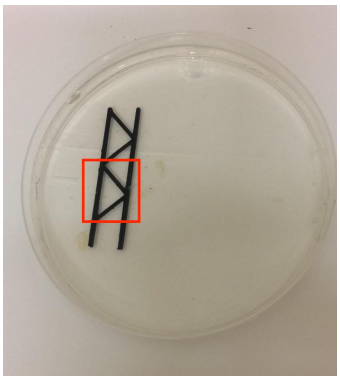

FIGURE 6.13: Geometrically-complex phantom embedded in gelatin (width of each line is $1mm$)

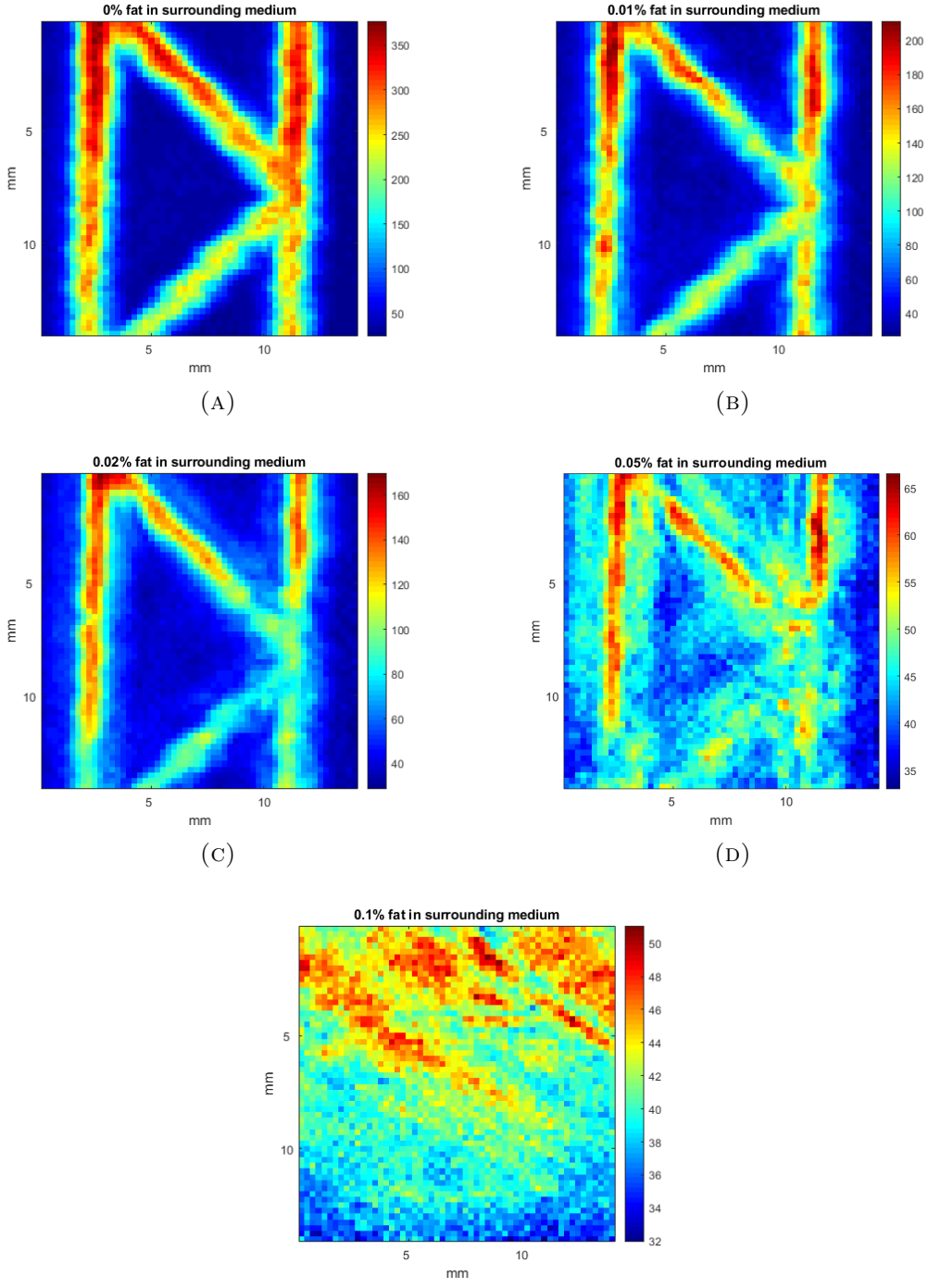

(A) (B) (C) (D) (E)

FIGURE 6.14: PA image of scaffold in (A) 0% fat, (B) 0.01% fat, (C) 0.02% fat, (D) 0.05% fat, (E) 0.1% fat. Time-gating was not performed while processing this data. All images acquired with in-house setup.

6.6 Lipid phantom imaging

In order to introduce more complexity in the PA absorber's surrounding medium, a black resin staircase phantom was 3D printed and immersed in water and lipid (see Fig. 6.15). This experiment was performed to assess the function of the PA probe in environments similar to soft tissue. The staircase phantom was first imaged under water, and the FWHM was assessed as the depth of the staircase underwater was increased from `1 mm` to `9 mm` (see Fig. 6.16 (C)). The staircase phantom was then immersed under lipid solution. The lipid phantom was made by adding `200 mL` of oil to `200 mL` gelatinous water (prepared using methods outlined in the first paragraph of Section 6.1). `9 g` of sodium dodecyl sulfate (SDS) was added to emulsify the solution. The staircases had varying depths of immersion in the lipid, with the closest stair being `1 mm` away from the transducer and immersed in `0 mm` lipid, and the farthest being `9 mm` away from the transducer and immersed in `8 mm` lipid. The latter staircase was not detected by the transducer.

The staircase phantom in water allowed us to determine how the resolution of the PA system changes as the probe-to-absorber distance is increased by assessing the FWHM. As the probe-to-absorber distance is increased, diameter of the laser beam from the fiber optic increases and intensity of the pressure wave detected decreases. This results in a spreading of the FWHM, which can be seen in (C) of Figure 6.16). Laser beam divergence increases non-linearly as light exits the fiber optic, and is dependent on the numerical aperture of the fiber optic. This non-linear increase in spread can be seen through the relatively large increase in FWHM from $6\,mm$ to $9\,mm$ probe-to-absorber distance in (C) of Figure 6.16). The

lipid surrounding medium marginally increases the FWHM of the PA signal, as seen in (D) of Figure 6.16). (D) also shows a decrease in signal between 2 mm and 6 mm probe-to-absorber distance. This can be attributed to the laser beam being increasingly guided into the core of the of fiber optic as the probe is moved by the translation stage. Combined, the physical instability of the collimator, fiber optic and translation stage contribute to the fiber optic moving with each step that the translation stage takes. As the fiber optic moves, the laser beam is guided into the core or cladding differently during acquisition over different regions of interests. When the light is guided more strongly into the core, there is low "doubling" effect resulting in a smaller FWHM, which explains the anomalous pattern in (D) of Figure 6.16).

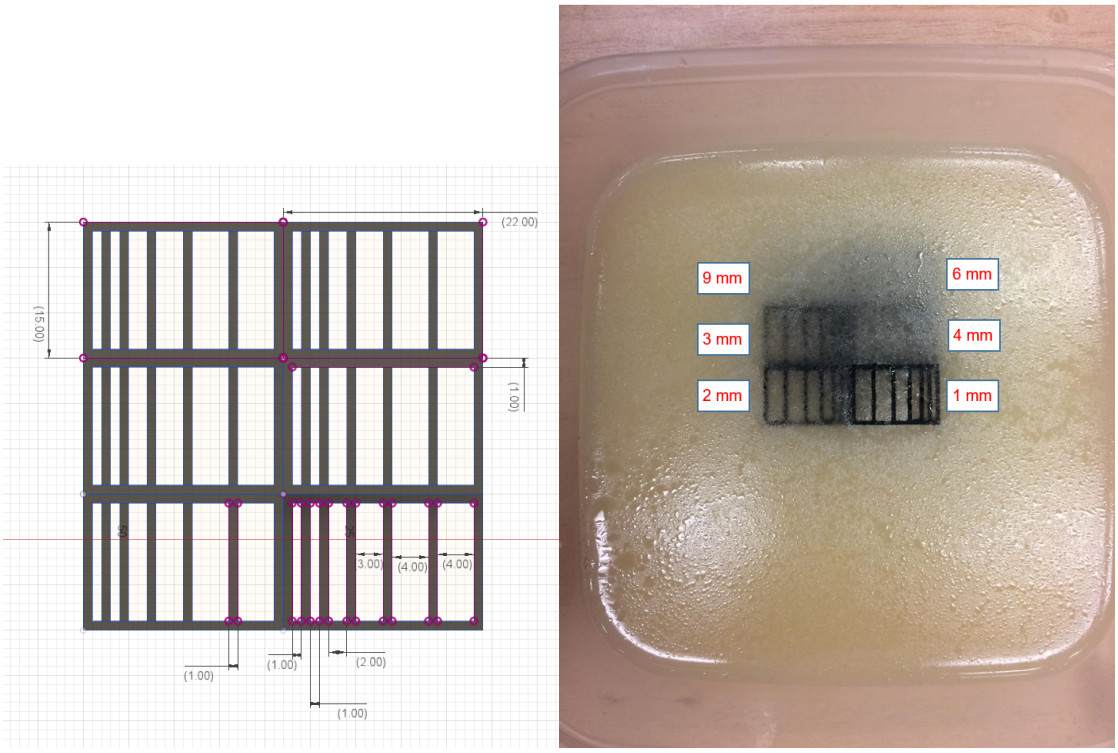

(A) (B)

Figure 6.15: Design of staircase phantom (all dimensions in mm) (A) and staircase phantom embedded in emulsified gelatin-oil at varying depths from the transducer (B)

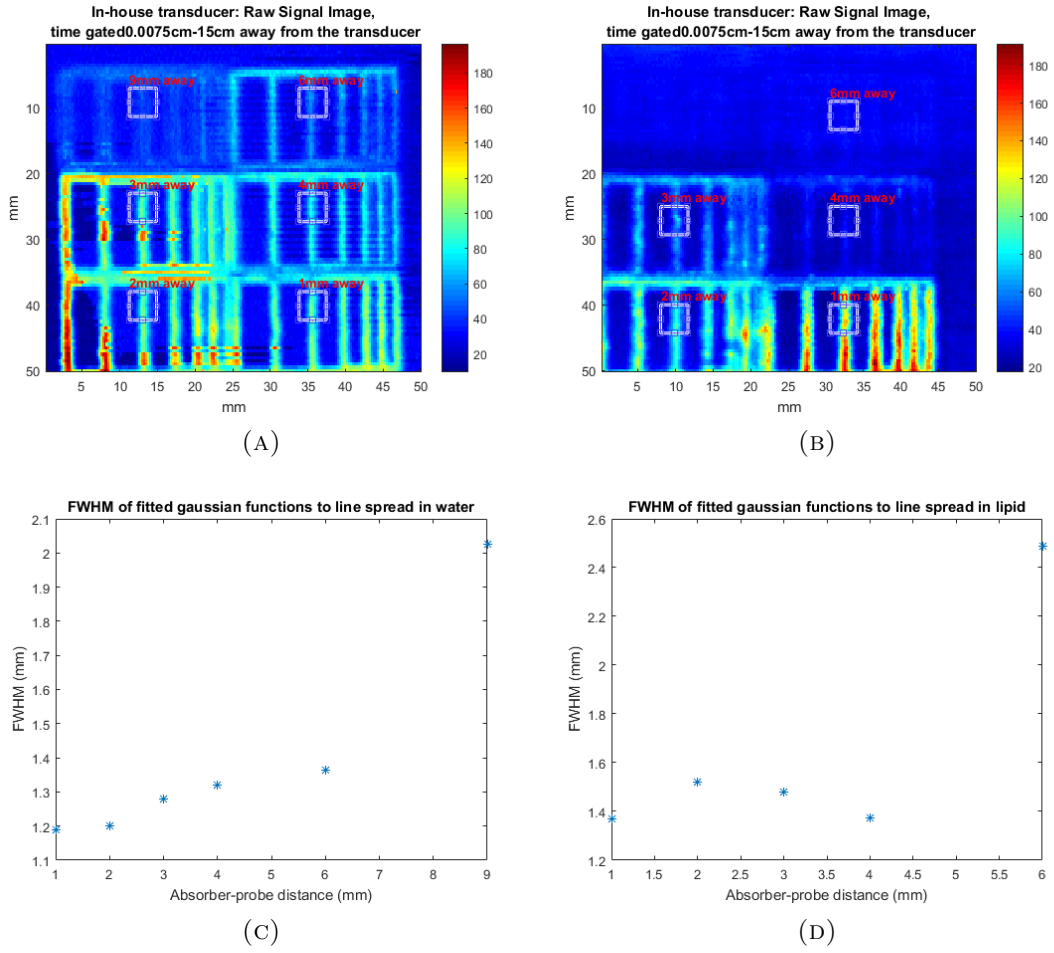

Figure 6.16: PA image of staircase immersed in water, with analysis regions shown (A), PA image of staircase immersed in lipid, with analysis regions shown (B), FWHM of absorbing lines in water as a function of probe-to-absorber distance (C) and FWHM of absorbing lines in lipid as a function of lipid depth and probe-to-absorber distance (D)

6.7 Effects of acoustic scattering on photoacoustic signal

In order to test acoustic scattering, a phantom was made with two layers (i) clear gelatinous layer (ii) gelatinous layers with 50% talcum powder (Johnson & Johnson). The talcum powder layer was made by adding `20 g` of talcum to `40 mL` gelatinous water (see Fig. 6.17). The transducer and light source were operated in transmission mode in two scenarios (1) light–clear-gelatin–absorber–talcum-gelatin–receiver (see Fig. 6.17 (A)), and (2) light–talc-gelatin–absorber–clear-gelatin–receiver (see Fig. 6.17 (B)). This allowed us to assess the effect of talcum on the light source in scenario (1), and the effect of talcum on sound waves produced after the PA effect in scenario (2).

Results from Scenario (1) show decreased PA signal intensity due to talcum interfering with light absorption for the PA absorber, meaning talcum acted as a light absorber, which can be clearly seen through the opaqueness of the gelatinous phantom in (D) of Fig. 6.17. Scenario (2) results show the high distortion experienced by the pressure waves generated, as the structure of the geometrically-complex PA absorber is not recovered in the formed image.

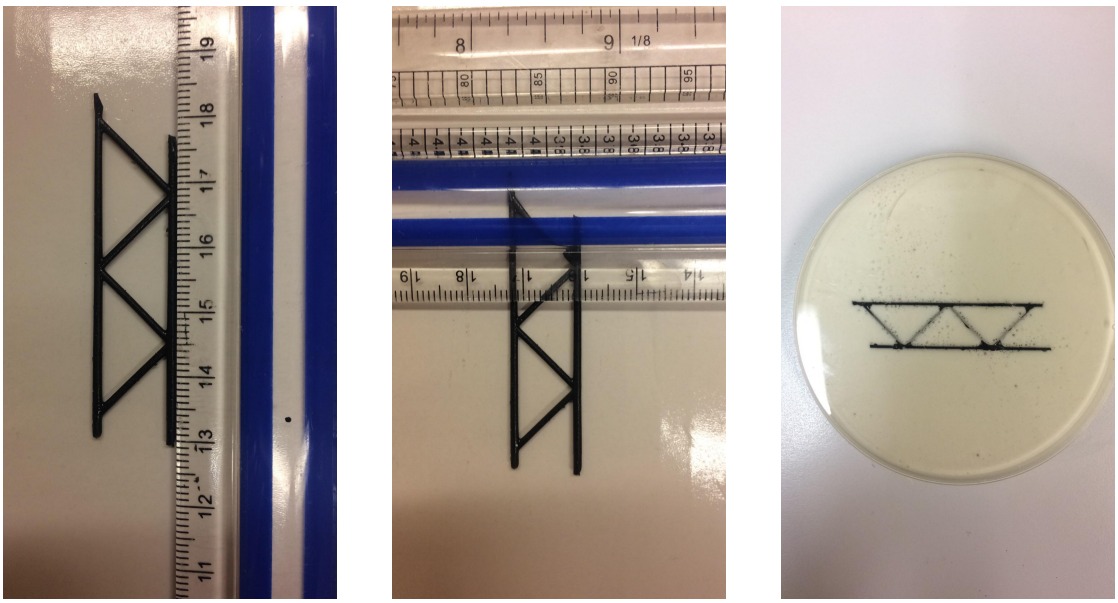

(A) (B) (C)

(D) (E)

Figure 6.17: Height (A) and Width (B) of absorber immersed between clear layers of gelatin (C) and a talcum-gelatin mix (D), each layer 4 mm deep (E)

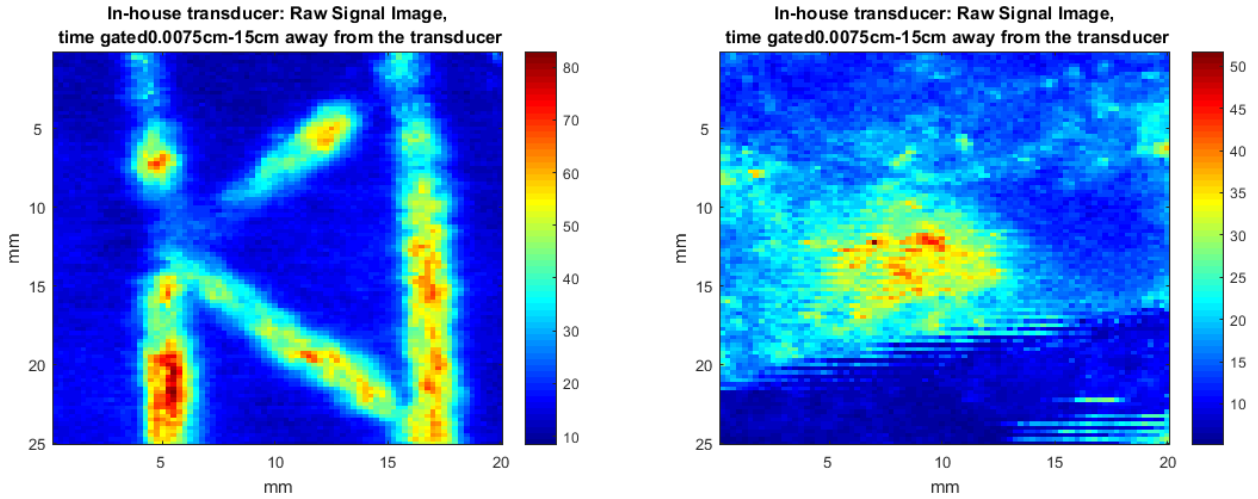

(A) (B)

FIGURE 6.18: PA Image produced as a result of light–clear-gelatin–absorber–talcum-gelatin–receiver (A) and light–talc-gelatin–absorber–clear-gelatin–receiver (B)

6.8 Penetration through bone

To test the practical application of detecting intracranial hemorrhages with the developed PA probe, a gelatinous phantom was made with a 2 mm thick bone plate covering an absorber (see Fig. 6.19). Penetration through bone was tested because bone was seen as the biggest barrier in penetration of light and recovery of PA signals. The transducer and light source were operated in transmission mode in two scenarios (1) light–gelatin–absorber–bone–receiver, and (2) light–bone–absorber–gelatin–receiver. This allowed us to analyze the penetration of ultrasound signal through bone in scenario (1), and penetration of light through bone in scenario (2). The light intensity was decreased with the use of filters in scenario (1) to assess the minimum light intensity necessary for a PA signal to be picked up (see Fig. 6.20 (A) through (C)). Penetration through bone with light was not achieved, and

high scattering was seen (see Fig. 6.20 (D)).

The results of scenario (1) showed that pressure waves generated with our PA system can be recovered with ease through bone with 1% of 125 mJ of light per 6 ns pulse. With a 532 nm light source, only 4% of light is expected to reach the absorber (see simulations in Section 4.1.2). Hence, perfect recovery of the PA absorber structure with the use of 532 nm light is not expected. Results of scenario (2) confirms this. Bone is highly scattering to 532 nm of light, and appropriate recovery of the absorber structure is not seen in (D) of 6.20. The "doubling" effect is also seen here, and distorts the recovered image further. The two horizontal lines seen at the top and bottom of the image correspond to the edges of the bone plate in the phantom.

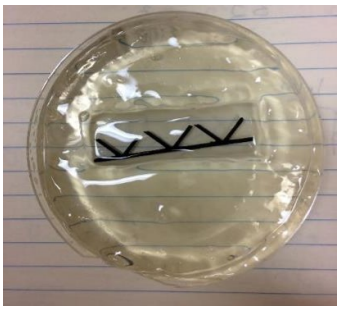

(A)

(B)

FIGURE 6.19: Excavated bone revealing absorber (A) and side view with absorber (left) and bone (right) (B)

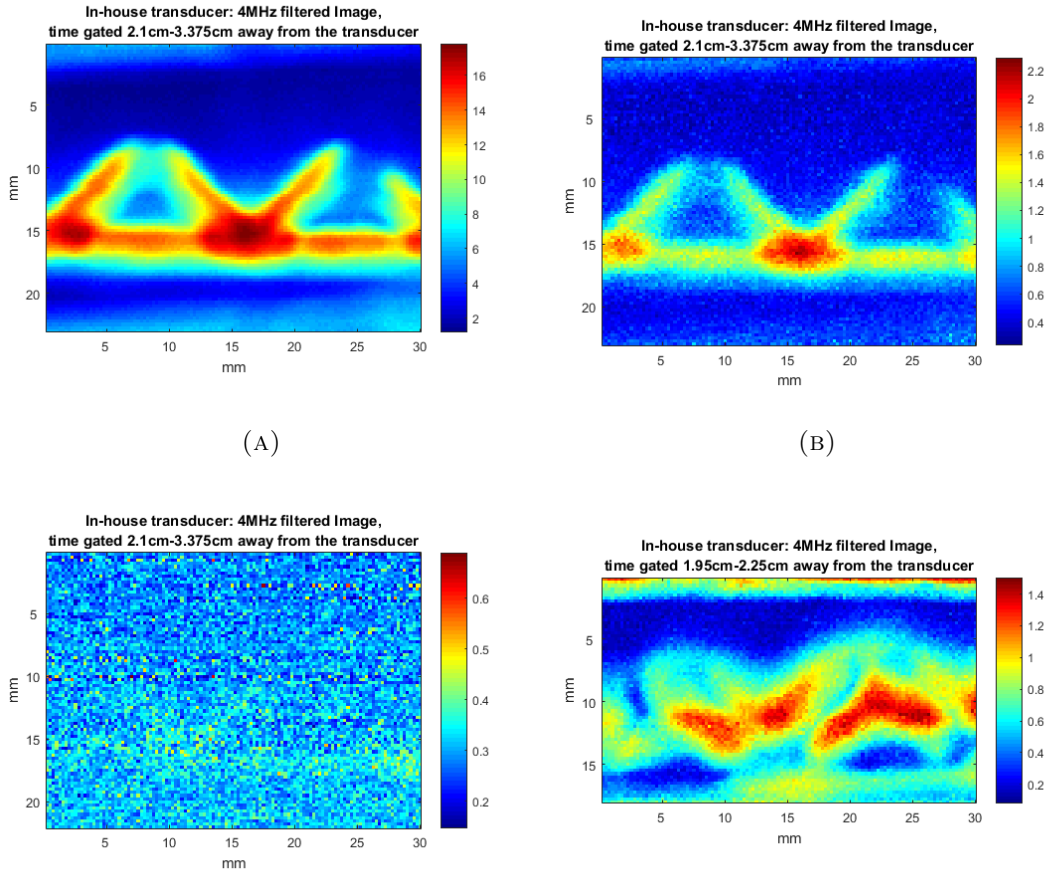

(A) (B)

(C) (D)

Figure 6.20: Ultrasound penetration through bone with 1 OD filter (A), 2 OD filter (B), 3 OD filter (C). Light penetration through bone (B)

Chapter 7

Discussion

This thesis discussed the development of a PA imaging system for with an application of detection of intracranial hemorrhages in mind. While we were able to successfully develop the PA system, there were many factors limiting the applications of this system and inducing errors in experimentation.

7.1 Factors influencing signal strength

The most frequent factor encountered that influenced signal strength of the PA signals was the variable alignment of the collimating lens with the laser beam. Guidance of the laser beam into the cladding of the fiber optic instead of the core cause a donut-shaped beam profile to exit out of the fiber optic. This resulted in a reduction of the resultant PA signal intensity and a wide FWHM, resulting in an inaccurate image of the PA absorber. Next, the linear translation stage was not securely affixed to the optical table, causing the stage along with the probe to be unstable while imaging. In some experiments, this has led to a "shifting" effect

of pixels from one row to another, resulting in a distorted image. Additionally, the orientation of the PA probe also impacts the PA signals acquired. If the ring-element in the PA probe is orthogonally facing the phantom, or PA absorber, the PA signal is noted to be higher in amplitude than when facing it at a different angle. These factors influenced the intensity of the received PA signals, which contributed to the degrading resolution capabilities of the PA system. All these factors can be mitigated by securely affixing all components to the optical table properly.

7.2 Noise inducing components

There were multiple sources of noise in the PA system. While experimenting with the PA probe, we found that it was necessary for the PA probe to share a ground with the linear translation stages to remove a component of the noise signals. As with any electrical system, appropriate grounding throughout the system is vital to eliminating noise signals from interfering the PA signals. Next, there was a RF noise signal constituting multiple frequencies around $1-2\,MHz$ in the signals that could not be eliminated (see (B) of Fig. 6.7). The source of these noise signals was assumed to be ambient RF signals from the surrounding imaging machines (MRI). A RF shielding aluminum housing around the experimental setup may reduce these noise signals. Averaging 10 signals at one location helped reduce the contribution of these noise signals to the image. Additionally, wires connecting the transducer element to the pre-amplifier were not shielded appropriately. The inside of a cable is made of three main components. They are the conductor, the dielectric, and

shield/braid. These components are then surrounded by an outer protective jacket. The conductor acts as the positive connection of the cable while the shield acts as the ground. The dielectric isolates the conductor from the shield. Most cables have one shielding/braided layer. The cables connecting the transducer element to the BNC cable were made up of a thin filament conductor only. Having a shielding/braided layer could have prevented noise interference. Furthermore, to better prevent electrical interference from the environment, all cables could have been double shielded cables which an additional shielding/braided layer in contact with the other.

7.3 Limitations of this thesis

There were some inefficiencies in how this work was performed. Phantoms were made with gelatin, which has a low shelf-life (maximum of 2-3 days). This is because gelatinous phantom stability is much lower compared to other alternatives. Gelatinous phantoms degrade easily overtime when submerged in a water bath. This limits the conclusions we can make about the resulting images accurately representing the phantoms, since the phantoms slightly degrade during imaging. Phantom stability can be improved by using alternative materials such as silicon or formaldehyde (Cook et al. 2011b). Next, some gelatinous phantoms had entrapped air bubbles, which caused unwanted large intensity signals to interfere with PA absorber signals. This can be ameliorated by placing phantoms in a vacuum chamber to release entrapped air. Additionally, the experiment to test acoustic backscatter could have been conducted with micrometer-sized silica

particles immersed in gelatin, instead of large crystals of talcum powder, as is traditionally used in PA research. This would have provided an accurate representation of the PA system's response to acoustic interference in surrounding media. Lastly, lack of an optical-parametric-oscillator (OPO) prevented us from showing the efficacy of our PA probe and apparatus at wavelengths relevant to the human body (near-infrared wavelengths), and relevant to our final clinical application of detection of intracranial hemorrhages. An OPO can convert our 532 nm laser wavelengths into relevant wavelengths in the near-infrared range. With an OPO, it can be shown that the PA probe's light source can penetrate dermal and bone layers to reach the hemorrhagic layer, and that the probe can capture the resulting acoustic waves to detect, localize and potentially image the boundaries of the hemorrhage accurately. Additionally, with an OPO, it may be possible to probe for differences in PA signals generated by different types of hemoglobin (oxygenated, de-oxygenated, methemoglobin, etc.) as these chromophores optimally absorb differing wavelengths of light. This may allow us to obtain information about the age of a hemorrhage (Bradley 1993).

7.4 Conclusion

In this thesis, we have designed and developed a cost-effective PA system aimed towards the detection of intracranial hemorrhages. Simulation exercises were used to determine whether an experimental system would be able to achieve the final clinical application of detection of intracranial hemorrhages. Based on the successful simulation results, we designed and built a prototype PA probe using a

Nd:YAG laser and ring-elements. We used commercial transducer elements to establish a baseline for expected PA signals. We experimented with different PA absorbers, using a combination of gelatinous India Ink, India Ink silicone, and India Ink diluter with water. We finally experimentally determined black resin material from our 3D printer to be the optimal PA absorber. The PA system was characterized using different geometries of this PA absorber embedded in gelatin and submerged in a water bath.

While we have designed and developed a PA system, the system can be greatly improved by using efficient experimental techniques and noise-reducing components. Furthermore, a OPO should be implemented to complete the last step of the designed experiments for these results to be clinically relevant for the application of detection of intracranial hemorrhages.

Bibliography

Aguirre, A., Ardeshirpour, Y., Sanders, M. M., Brewer, M., and Zhu, Q. (2011). Potential Role of Coregistered Photoacoustic and Ultrasound Imaging in Ovarian Cancer Detection and Characterization. *Translational Oncology*. ISSN: 19365233.

Allen, T. J. and Beard, P. C. (2016). High power visible light emitting diodes as pulsed excitation sources for biomedical photoacoustics. *Biomedical Optics Express* 7(4), 1260. ISSN: 2156-7085.

Best, G. and Sezerman, Ö. M. (1999). Shedding Light on Hybrid Optics: A Tutorial in Coupling. *Opt. Photon. News* 10(2), 30–34.

Biqin, D., Sun, C., and Zhang, H. F. (2017). *Optical Detection of Ultrasound in Photoacoustic Imaging*.

Bradley, W. G. J. (1993). MR appearance of hemorrhage in the brain. eng. *Radiology* 189(1), 15–26. ISSN: 0033-8419 (Print).

Brenner, D. J., Elliston, C. D., Hall, E. J., and Berdon, W. E. (2001). Estimated Risks of Radiation-Induced Fatal Cancer from Pediatric CT. *American Roentgen Ray Society* 176(February), 289–296. ISSN: 0361-803X, 1546-3141.

Brott, T., Broderick, J., Kothari, R., Barsan, W., Tomsick, T., Sauerbeck, L., Spilker, J., Duldner, J., and Khoury, J. (1997). Early Hemorrhage Growth in Patients With Intracerebral Hemorrhage. *Stroke* 28(1),

Caceres, J. A. and Goldstein, J. N. (2012). Intracranial Hemorrhage. *Emergency medicine clinics of North America* 30(3), 771–794. ISSN: 0733-8627.

Caceres, J. A. and Goldstein, J. N. (2013). Intracranial Hemorrhage. *Emergency medicine clinics of North America* 30(3), 771–794.

Cook, J. R., Bouchard, R. R., and Emelianov, S. Y. (2011a). Tissue-mimicking phantoms for photoacoustic and ultrasonic imaging. *Biomedical optics express* 2(11), 3193–3206. ISSN: 2156-7085.

Cook, J. R., Bouchard, R. R., and Emelianov, S. Y. (2011b). Tissue-mimicking phantoms for photoacoustic and ultrasonic imaging. 2(11), 2243–2254.

De Boer, H. H., Van der Merwe, A. E., and Soerdjbalie-Maikoe, V. (2016). Human cranial vault thickness in a contemporary sample of 1097 autopsy cases: relation to body weight, stature, age, sex and ancestry. ENG. *International Journal of Legal Medicine* 130(5), 1371–1377. ISSN: 14371596.

Di Leo, G., Trimboli, R. M., Sella, T., and Sardanelli, F. (2017). Optical imaging of the breast: Basic principles and clinical applications. *American Journal of Roentgenology* 209(1), 230–238. ISSN: 15463141.

Diebold, G. J., Sun, T., and Khan, M. I. (1991). Photoacoustic monopole radiation in one, two, and three dimensions. *Physical Review Letters*. ISSN: 00319007.

Dogra, V. S., Chinni, B. K., Valluru, K. S., Moalem, J., Giampoli, E. J., Evans, K., and Rao, N. A. (2014). Preliminary results of ex vivo multispectral photoacoustic imaging in the management of thyroid cancer. *American Journal of Roentgenology*. ISSN: 15463141.

Dogra, V., Evans, K., Ghazi, A., Joseph, J., Messing, E., Rao, N., Valluru, K., Yao, J., and Chinni, B. (2013). Multispectral Photoacoustic Imaging of Prostate

Cancer: Preliminary Ex-vivo Results. *Journal of Clinical Imaging Science*. ISSN: 2156-7514.

Favazza, C. P., Jassim, O., Cornelius, L. A., and Wang, L. V. (2011). In vivo photoacoustic microscopy of human cutaneous microvasculature and a nevus. *Journal of Biomedical Optics*. ISSN: 10833668.

Freeman, W. D. and Aguilar, M. I. (2012). Intracranial hemorrhage: Diagnosis and management. *Neurologic Clinics* 30(1), 212–240.

Fry, F. J. (1977). Transkull transmission of an intense focused ultrasonic beam. *Ultrasound in Medicine and Biology*. ISSN: 03015629.

Gabriel, C., Gabriel, S., and Corthout, E. (1996). *The dielectric properties of biological tissues: I. Literature survey*. Tech. rep., 2231–2249.

Gao, Y., Rong, J., and Jing, X. (2013). The effect of different center frequency of transducers on the photoacoustic tomography. In: *Proceedings of 2013 IEEE International Conference on Medical Imaging Physics and Engineering*, 315–318. ISBN: 9781467360128.

González, A. B. (2011). Estimates of the potential risk of radiation-related cancer from screening in the UK. *Journal of Medical Screening* 18(4), 163–164. ISSN: 1475-5793.

Griffey, R. T., Sodickson, A., Rt, G., and Sodickson, A. (2009). Cumulative Radiation Exposure and Cancer Risk Estimates in Emergency Department Patients Undergoing Repeat or Multiple CT. *American Journal of Roentgenology* 192(April), 887–892.

Heijblom, M., Piras, D., Engh, F. M. van den, Schaaf, M. van der, Klaase, J. M., Steenbergen, W., and Manohar, S. (2016). The state of the art in breast imaging

using the Twente Photoacoustic Mammoscope: results from 31 measurements on malignancies. *European Radiology*. ISSN: 14321084.

Hoshi, Y. and Yamada, Y. (2016). Overview of diffuse optical tomography and its clinical applications. *Journal of Biomedical Optics* 21(9), 091312. ISSN: 1083-3668.

Ihara, I. (2008). Ultrasonic sensing: Fundamentals and its applications to non-destructive evaluation. In: *Lecture Notes in Electrical Engineering*. Ed. by S. Mukhopadhyay and R. Huang. Berlin: Springer. Chap. 21. ISBN: 9783540690306.

Jacques, S. L. (2013). Optical properties of biological tissues: a review. *Physics in medicine and biology* 58(11), 37–61. ISSN: 1361-6560.

Jacques, S. L. (2014). Coupling 3D Monte Carlo light transport in optically heterogeneous tissues to photoacoustic signal generation. *Photoacoustics*. ISSN: 22135979.

Jacques, S., Li, T., and Prahl, S. (2013). *Monte Carlo simulations of light transport in 3D heterogenous tissues (mcxyz.c)*.

Kahraman, S., Kayali, H., Atabey, C., Acar, F., and Gocmen, S. (2006). The accuracy of near-infrared spectroscopy in detection of subdural and epidural hematomas. *The Journal of trauma* 61(6), 1480–1483.

Kazui, S., Naritomi, H., Yamamoto, H., Sawada, T., and Yamaguchi, T. (1996). Enlargement of Spontaneous Intracerebral Hemorrhage. *Stroke* 27(10),

Ke, H., Erpelding, T. N., Jankovic, L., Liu, C., and Wang, L. V. (2012). Performance characterization of an integrated ultrasound, photoacoustic, and thermoacoustic imaging system. *Journal of Biomedical Optics* 17(5), 1–6. ISSN: 1083-3668.

Kim, G. R., Kang, J., Kwak, J. Y., Chang, J. H., Kim, S. I., Youk, J. H., Moon, H. J., Kim, M. J., and Kim, E. K. (2014). Photoacoustic imaging of breast microcalcifications: A preliminary study with 8-gauge core-biopsied breast specimens. *PLoS ONE*. ISSN: 19326203.

Koechner, W. and Bass Springer, M. (2003). *Solid-State Lasers: A Graduate Text*. Ed. by H. Koelsch. Springer.

Kolkman, R. G., Leeuwen, T. G. v., and Steenbergen, W. (2009). Photoacoustic Imaging with a Double-Ring Sensor. In: *Photoacoustic Imaging and Spectroscopy*. Ed. by L. V. Wang. Boca Raton: CRC Press. Chap. 15, 197. ISBN: 9781420059915.

Kruger, R. A., Miller, K. D., Reynolds, H. E., Kiser, W. L., Reinecke, D. R., and Kruger, G. A. (2000). Breast Cancer in Vivo: Contrast Enhancement with Thermoacoustic CT at 434 MHz - Feasibility Study. *Radiology* 216(1), 279–284.

Ku, G., Fornage, B. D., Jin, X., Xu, M., Hunt, K. K., and Wang, L. V. (2005a). Thermoacoustic and photoacoustic tomography of thick biological tissues toward breast imaging. *Technology in Cancer Research and Treatment* 4(5), 559–565. ISSN: 15330346.

Ku, G., Wang, X., Xie, X., Stoica, G., and Wang, L. V. (2005b). Imaging of tumor angiogenesis in rat brains in vivo by photoacoustic tomography. ENG. *Applied optics* 44(5), 770–775. ISSN: 0003-6935 (Print).

Laser Institute of America (2007). *American National Standard for Safe Use of Lasers: ANSI Z136.1*. Tech. rep.

Lazebnik, M., Popovic, D., McCartney, L., Watkins, C. B., Lindstrom, M. J., Harter, J., Sewall, S., Ogilvie, T., Magliocco, A., Breslin, T. M., Temple, W.,

Mew, D., Booske, J. H., Okoniewski, M., and Hagness, S. C. (2007). A large-scale study of the ultrawideband microwave dielectric properties of normal, benign and malignant breast tissues obtained from cancer surgeries. *Physics in Medicine and Biology*. ISSN: 00319155.

Lee, J., El-Abaddi, N., Duke, A., Cerussi, A. E., Brenner, M., and Tromberg, B. J. (2006). Noninvasive in vivo monitoring of methemoglobin formation and reduction with broadband diffuse optical spectroscopy. *Journal of applied physiology* 100(2), 615–622.

Leon-Carrion, J., Dominguez-Roldan, J. M., Leon-Dominguez, U., and Murillo-Cabezas, F. (2010). The Infrascanner, a handheld device for screening in situ for the presence of brain haematomas. *Brain Injury*.

Li, C., Pramanik, M., Ku, G., and Wang, L. V. (2008). Image distortion in thermoacoustic tomography caused by microwave diffraction. *Physical Review E - Statistical, Nonlinear, and Soft Matter Physics* 77(3), 1–7. ISSN: 15393755.

Li, C. and Wang, L. V. (2009). Photoacoustic tomography and sensing in biomedicine. *Physics in medicine and biology* 54(19), 59–97.

Marinovich, M. L., Sardanelli, F., Ciatto, S., Mamounas, E., Brennan, M., Macaskill, P., Irwig, L., Minckwitz, G. von, and Houssami, N. (2012). Early prediction of pathologic response to neoadjuvant therapy in breast cancer: Systematic review of the accuracy of MRI. *Breast* 21(5), 669–677.

Marshall, L. F. (2009). Traumatic Injuries of the Central Nervous System. In: *Clinical Adult Neurology*. Ed. by J. Corey-Bloom and R. B. David. 3rd ed. New York: Demos Medical Publishing. Chap. 16, 276.

Martí-Bonmatí, L., Sopena, R., Bartumeus, P., and Sopena, P. (2010). Multimodality imaging techniques. *Contrast Media and Molecular Imaging* 5(4), 180–189.

Mehmet, S. E., Johnston, C., Tempany-Afdhal, C., and Abbeele, A. D. d. (2009). Imaging Tools in Human Research. In: *Clinical and Translational Science: Principles of Human Research*. Ed. by D. Robertson and G. H. Williams. Chap. 6, 87–104.

Mitcham, T., Dextraze, K., Taghavi, H., Melancon, M., and Bouchard, R. (2015). Photoacoustic imaging driven by an interstitial irradiation source. *Photoacoustics*. ISSN: 22135979.

NDT Resource Center (2014). *Ultrasound*.

Nelson, J. (1999). Continuous-time random-walk model of electron transport in nanocrystalline TiO2 electrodes. *Physical Review B - Condensed Matter and Materials Physics* 59(23), 15374–15380. ISSN: 1550235X.

Nie, L., Cai, X., Maslov, K., Garcia-Uribe, A., Anastasio, M. a., and Wang, L. V. (2012). Photoacoustic tomography through a whole adult human skull with a photon recycler. *Journal of biomedical optics* 17(11), 110506. ISSN: 1560-2281.

Nie, L., Guo, Z., and Wang, L. V. (2011). Photoacoustic tomography of monkey brain using virtual point ultrasonic transducers. *Journal of biomedical optics* 16(7), 1–5.

Nie, L., Xing, D., Zhou, Q., Yang, D., and Guo, H. (2008). Microwave-induced thermoacoustic scanning CT for high-contrast and noninvasive breast cancer imaging. *Medical Physics*. ISSN: 00942405.

Ntziachristos, V. (2010). Going deeper than microscopy: the optical imaging frontier in biology. *Nature methods* 7(8), 603–614.

Olympus Corporation (2017). *Introduction to Ultrasonic Phased Array*.

Peng, K., He, L., Wang, B., and Xiao, J. (2015). Detection of cervical cancer based on photoacoustic imaging—the in-vitro results. *Biomedical Optics Express*. ISSN: 2156-7085.

Petrov, I. Y., Petrov, Y., Prough, D. S., Richardson, C. J., Fonseca, R. A., Robertson, C. S., Asokan, C. V., Agbor, A., and Esenaliev, R. O. (2016). Transmission (forward) mode, transcranial, noninvasive optoacoustic measurements for brain monitoring, imaging, and sensing. In: *Proceedings of SPIE*. Vol. 9708, 1–8.

Piras, D., Xia, W., Steenbergen, W., Van Leeuwen, T. G., and Manohar, S. (2010). Photoacoustic imaging of the breast using the twente photoacoustic mammoscope: Present status and future perspectives. *IEEE Journal on Selected Topics in Quantum Electronics*. ISSN: 1077260X.

Salihovi, D., Smajlovic, D., and Ibrahimagic, O. C. (2013). Does the Volume and Localization of Intracerebral Hematoma Affect Short-Term Prognosis of Patients with Intracerebral Hemorrhage ? 2013(March 2008), 10–13.

Sistrom, C. L. and McKay, N. L. (2005). Costs, charges, and revenues for hospital diagnostic imaging procedures: Differences by modality and hospital characteristics. *Journal of the American College of Radiology* 2(6), 511–519.

Stiell, I. G., Clement, C. M., Rowe, B. H., Schull, M. J., Brison, R., Cass, D., Eisenhauer, M. A., Mcknight, R. D., Bandiera, G., Holroyd, B., Lee, J. S., Dreyer, J., Worthington, J. R., Reardon, M., Macphail, I., Wells, G. A., and Page, P. (2005). Comparison of the Canadian CT Head Rule and the New Orleans Criteria in Patients With Minor Head Injury. *JAMA* 294(12), 1511–1518.

Sun, C.-W. and Chuang, C.-C. (2012). Hemodynamics Study Based on Near-Infrared Optical Assessment. In: *Hemodynamics - New Diagnostic and Therapeutic Approaches*. Ed. by A. S. Artis. InTech. Chap. 3, 47–68. ISBN: 978-953-51-0559-6.

Tang, A. M., Kacher, D. F., Lam, E. Y., Wong, K. K., Jolesz, F. A., and Yang, E. S. (2008). Simultaneous ultrasound and MRI system for breast biopsy: Compatibility assessment and demonstration in a dual modality phantom. *IEEE Transactions on Medical Imaging* 27(2), 247–254.

Tang, M. X., Elson, D. S., Li, R., Dunsby, C., and Eckersley, R. J. (2010). Photoacoustics, thermoacoustics, and acousto-optics for biomedical imaging. *Proceedings of the Institution of Mechanical Engineers, Part H: Journal of Engineering in Medicine*. ISSN: 09544119.

Thorlabs Inc. (2018). *MM Fiber Tutorial*.

Treeby, B. E. and Cox, B. T. (2010). k-Wave: MATLAB toolbox for the simulation and reconstruction of photoacoustic wave fields. *Journal of Biomedical Optics*.

Tsivgoulis, G. and Alexandrov, A. V. (2016). Ultrasound in Neurology. *CONTINUUM Lifelong Learning in Neurology* 22(5), 1655–1677. ISSN: 15386899.

Tuchin, V. (2016). Tissue Optics and Photonics: Light-Tissue Interaction II. *Journal of Biomedical Photonics & Engineering*. ISSN: 24112844.

Tuchin, V. V. (2015). Tissue Optics and Photonics : Light-Tissue Interaction. 4(June), 9–38.

Ugryumova, N., Matcher, S. J., and Attenburrow, D. P. (2004). Measurement of bone mineral density via light scattering. *Physics in medicine and biology* 49(3), 469–483. ISSN: 0031-9155.

Valluru, K. S. and Willmann, J. K. (2016). Clinical photoacoustic imaging of cancer. *Ultrasonography* 35(4), 267–280. ISSN: 2288-5919.

Wang, L. V. (2008). *Prospects of photoacoustic tomography*.

Wang, L. V. (2009). *Photoacoustic Imaging and Spectroscopy*. CRC Press.

Wang, L. V. and Yao, J. (2016). A practical guide to photoacoustic tomography in the life sciences. 13(8).

Wang, X., Chamberland, D. L., and Xi, G. (2008). Noninvasive reflection mode photoacoustic imaging through infant skull toward imaging of neonatal brains. *Journal of Neuroscience Methods* 168(2), 412–421.

Wang, X., Pang, Y., Ku, G., Xie, X., Stoica, G., Wang, L. L. V., Gamelin, J., Maurudis, A., Aguirre, A., Huang, F., Guo, P., Wang, L. L. V., Zhu, Q., Xia, J., Huang, C., Maslov, K., Anastasio, M. a., and Wang, L. L. V. (2003). Noninvasive laser-induced photoacoustic tomography for structural and functional in vivo imaging of the brain. *Nature Biotechnology* 21, 803–806. ISSN: 1539-4794.

Wray, S., Cope, M., Delpy, D. T., Wyatt, J. S., Osmund, E., and Reynolds, R. (1988). *Characterization of the near infrared absorption spectra of cytochrome aa 3 and haemoglobin for the non-invasive monitoring of cerebral oxygenation*. Tech. rep., 184–192.

Xiang, L., Tang, S., Ahmad, M., and Xing, L. (2016). High Resolution X-ray-Induced Acoustic Tomography. *Scientific Reports* 6, 1–6. ISSN: 20452322.

Xu, M. and Wang, L. V. (2006a). Photoacoustic imaging in biomedicine. *Review of Scientific Instruments* 77(4), 1–22.

Xu, Y. and Wang, L. V. (2005). Medical Imaging with Microwave: Thermoacoustic Tomography. In: *Encyclopedia of RF and Microwave Engineering*. Ed. by Kai Chang. New Jersey: John Wiley & Sons Inc., 2530–2540. ISBN: 0471654507.

Xu, Y. and Wang, L. V. (2006b). Rhesus monkey brain imaging through intact skull with thermoacoustic tomography. *IEEE Transactions on Ultrasonics, Ferroelectrics, and Frequency Control*.

Yang, X. and Wang, L. V. (2008). Monkey brain cortex imaging by photoacoustic tomography. *Journal of Biomedical Optics*. ISSN: 10833668.

Yao, J. and Wang, L. V. (2014). Photoacoustic brain imaging: from microscopic to macroscopic scales. *Neurophotonics* 1(1), 011003. ISSN: 2329-423X.

Yao, D.-K., Zhang, C., Maslov, K., and Wang, L. V. (2014). Photoacoustic measurement of the Grüneisen parameter of tissue.

Zhou, Y., Yao, J., and Wang, L. V. (2016). Tutorial on photoacoustic tomography. *Journal of Biomedical Optics* 21(6), 061007. ISSN: 1083-3668.